Development of a Fiberoptic Microneedle Device for Simultaneous Co-Delivery of Fluid Agents and Laser Light with Specific Applications in the Treatment of Brain and Bladder Cancers

Robert Lyle Hood

Dissertation submitted to the faculty of Virginia Polytechnic Institute and State University in partial
fulfillment of the requirements for the degree of

Doctor of Philosophy
In
Biomedical Engineering

Christopher G. Rylander, Chair
Rafael V. Davalos
Paulo A. Garcia
John L. Robertson
John H. Rossmeisl, Jr.

August 29th, 2013

Blacksburg, VA

Keywords: Microneedle, Transitional Cell Carcinoma, Malignant Glioma, Convection-Enhanced Delivery, Biotransport, Single-Walled Carbon Nanohorns

Development of a Fiberoptic Microneedle Device for Simultaneous Co-Delivery of Fluid Agents and Laser Light with Specific Applications in the Treatment of Brain and Bladder Cancers

Robert Lyle Hood

ABSTRACT

This dissertation describes the development of the fiberoptic microneedle device (FMD), a microneedle technology platform for fluid and light delivery, from general engineering characterization to specific applications in treating bladder and brain cancers. The central concept of the FMD is physical modification of silica fiberoptics and capillary tubes into sharp microneedles capable of penetrating a tissue's surface, enabling light and fluid delivery into the interstitial spaces. Initial studies sought to characterize the mechanical penetration and optical delivery of multimode fiberoptics and capillary tubes modified through a custom, CO_2 laser melt-drawing technique. Additional work with multimode fibers investigated using an elastomeric lateral support medium to ensure robust penetration of small diameter fibers. These early experiments laid an engineering foundation for understanding the FMD technology.

Subsequent studies focused on developing the FMD to treat specific diseases. The first such investigation sought to leverage the high aspect ratio nature of FMDs made from long capillary tubes as a therapy delivery device deployable through the instrument channel of a urological cystoscope. The therapeutic strategy was to infuse single-walled carbon nanohorns (SWNHs), a carbon-based nanoparticle allowing surface modification and drug encapsulation, into the infiltrating front of later stage bladder tumors. The SWNHs primarily serve as exogenous

chromophores, enabling a fluid-based control of photothermal heat generation created when the SWNHs interacted with laser energy from an interstitial FMD or a light-emitting fiber in the bladder's interior. The study described here primarily sought to characterize the dispersal of the infused SWNHs and the photothermal response of the particles when heated with a 1064 nm laser.

The FMD was also developed as a platform capable of conducting convection-enhanced delivery (CED), a therapeutic approach to treat invasive tumors of the central nervous system such as malignant glioma (MG). Intracranial CED involves the placement of small catheters local to the tumor site and slow infusion of a chemotherapeutic over long timeframes (12-72 hours). A primary challenge of this treatment approach is infused chemotherapeutics not dispersing sufficiently to reach the infiltrating cells in the tumor's margins. The hypothetical improvement provided by the FMD technology is using sub-lethal photothermal heating to sufficiently increase the diffusive and convective transport of an infusate to reach infiltrative cells in the tumor's periphery. Initial experiments sought to demonstrate and characterize a heat-mediated increase of volumetric dispersal in Agarose tissue phantoms and *ex vivo* tissue. Subsequent studies with *in vivo* rodent models determined the best laser parameters to achieve the desired levels of diffuse, sub-lethal heat generation and then demonstrated the hypothesis of increasing the rate of volumetric dispersal though concurrent local hyperthermia. This research was the first demonstration of photothermal augmentation of an interstitially infused fluid's dispersal rate, which may have uses outside of the CED approach to brain cancer exhibited here. Taken in sum, this manuscript describes the potency and versatility of the FMD technology platform through its development in various biomedical applications.

Acknowledgments

I would like to acknowledge my advisors, colleagues, and friends that helped guide me through developing this project from concept to prototype to testing. I would like to specifically thank Drs. Chris Rylander, John Robertson, and John Rossmeisl for their mentorship, advice, and encouragement throughout my time at Virginia Tech. In addition, I would like to recognize that the faithfulness and support of my God, family and friends made my success possible, with the most notable contributions from the last group by my beloved wife Gold, my partners on the FMD project: Rudy Andriani, Tobias Ecker, and Dr. Alpaslan Kosoglu, and lastly the advice, camaraderie, and general ego-checking providing by Drs. William Vogt and Katelyn Colacino.

TABLE OF CONTENTS

Contents

LIST OF FIGURES

LIST OF TABLES

Chapter I: Introduction and Literature Review
1.0 Introduction to the Fiberoptic Microneedle Device

1.1 Introduction to Microneedles

In recent years, developments in microscale fabrication have enabled the creation of needles on the scale of micrometers. These "microneedles" can be created out of a variety of materials such as polymers, metals, or glass, and are utilized to facilitate highly accurate small volume fluid delivery with minimal tissue disruption. Studies have shown that needle diameter and insertion force are primary determinants of patient pain caused by transdermal injection [1-3]. The small diameter of these microneedles reduces the invasiveness and patient sensation associated with their clinical use. The potential presented by these microneedles for therapeutic and diagnostic applications has led to a significant investment of research attention.

One of the first therapeutic applications utilizing microneedles was focused on increasing the effectiveness of transdermal drug delivery patches by enhancing skin permeability with slight penetration (<1 mm) [4]. Other applications involved using microneedles as electrodes to measure electrical potentials or cause electroporation in tissue [5-7] Other groups have successfully utilized these needles for intrascleral delivery of therapeutic agents and to inoculate patients against disease [8, 9]. Solid, biodegradable polymer microneedles containing dissolved pharmaceuticals have been developed for time-delayed drug release [10-12]. Due to the lessened patient discomfort associated with their small penetration diameter, microneedles have been developed for use in patients with conditions that require frequent infusions, such as diabetics [13]. However, this design parameter provides some challenges, as small diameters can make delivery of large volumes at convenient flow rates difficult. To bypass this difficulty, parallel

arrays of microneedles can be utilized. Early developers of this design successfully delivered sufficient insulin to lower glucose levels in diabetic rats [13, 14]. In a more refined variant of the parallel array design, one group developed a microneedle-based transdermal patch device that allowed for the active dispensation of insulin [15]. Microneedles are continuing to receive a great amount of research attention, with new designs being applied to novel applications in many diverse fields.

1.2 Introduction to the Fiberoptic Microneedle Device

1.2.1 Interstitial Light Delivery

The fiberoptic microneedle device, or FMD, was initially conceptualized as a device permitting controllable light delivery interstitially, with specific applications in transdermal deployment. Very fine, silica, solid fibers delivering light or hollow fibers delivering fluid would be laterally supported with an elastomeric material, allowing robust handling and enabling penetration through the tough epidermal and dermal skin layers to targets in the underlying tissue. Initial experiments with step index, multimode fiberoptics altered through a multistage, custom melt-drawing procedure were described in Kosoglu, Hood *et al.* [16]. FMDs with a 3 mm unsupported length and an average diameter of 125 μm were demonstrated to repeatedly penetrate *ex vivo* porcine skin samples with less than 75 mN of driving force. The FMDs also underwent destructive testing to determine their critical buckling force (F_{CR}) for different geometries. F_{CR} for FMDs were shown to be accurately approximated through Euler's buckling formula for a cylindrical column, which is given in Eq. (1) [17];

$$F_{CR} = \frac{E\pi^3 d_{AVG}^{\ 4}}{64(KL)^2} \tag{1}$$

In Eq. (1), E is the elastic modulus of silica (73 GPa), K is the effective length factor (determined by boundary conditions), L is the unsupported length, and d_{AVG} is the average diameter. This formula indicates that F_{CR} is dependent to the fourth order of d_{AVG}, meaning that relatively small changes in diameter have a substantial effect on buckling. Examples of tapered FMDs manufactured and utilized in this study can be seen in Figure 1.

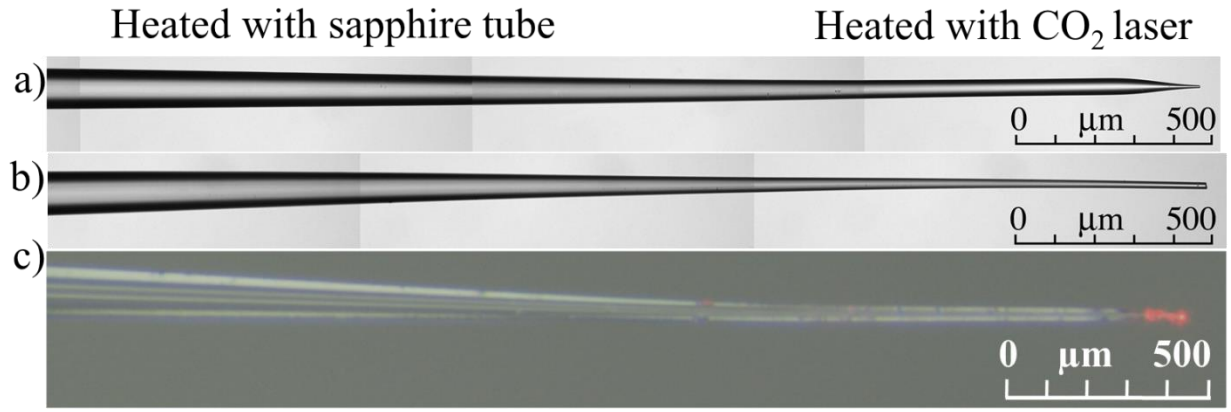

Figure 1: a) Brightfield image of a sharp (double-tapered) fiberoptic microneedle. b) Brightfield image of a flat (single-tapered) fiberoptic microneedle. c) Color microscope image of a sharp fiberoptic microneedle delivering red laser light near the tip (λ=633 nm, 0.1 mm leakage length in air).

A follow-up study by Kosoglu, Hood *et al.* sought to leverage a hydrofluoric-etching procedure to allow greater control of light leakage [18]. By exposing a greater length of a multimode fiber's core before the terminal tip, light leakage lengths of up to 2-3 mm were attained. This design made the terminal length of the FMDs act as optical diffusers, effectively lowering the local fluence of delivered light while allowing treatment of larger tissue volumes per exposure. Such a design would be advantageous in applications such as laser fat lipolysis, where relatively larger volumes of fat could be rapidly liquefied. Both the manufacturing procedure and fat

liquefaction in *ex vivo* porcine adipose tissue were demonstrated in the study, and an example of the latter is shown in Figure 2. Greater dispersed light leakage was observed in thinner FMDs created through longer immersion periods, but the increased fragility of thinner needles required the design to be carefully balanced between mechanical robustness and superior light distribution.

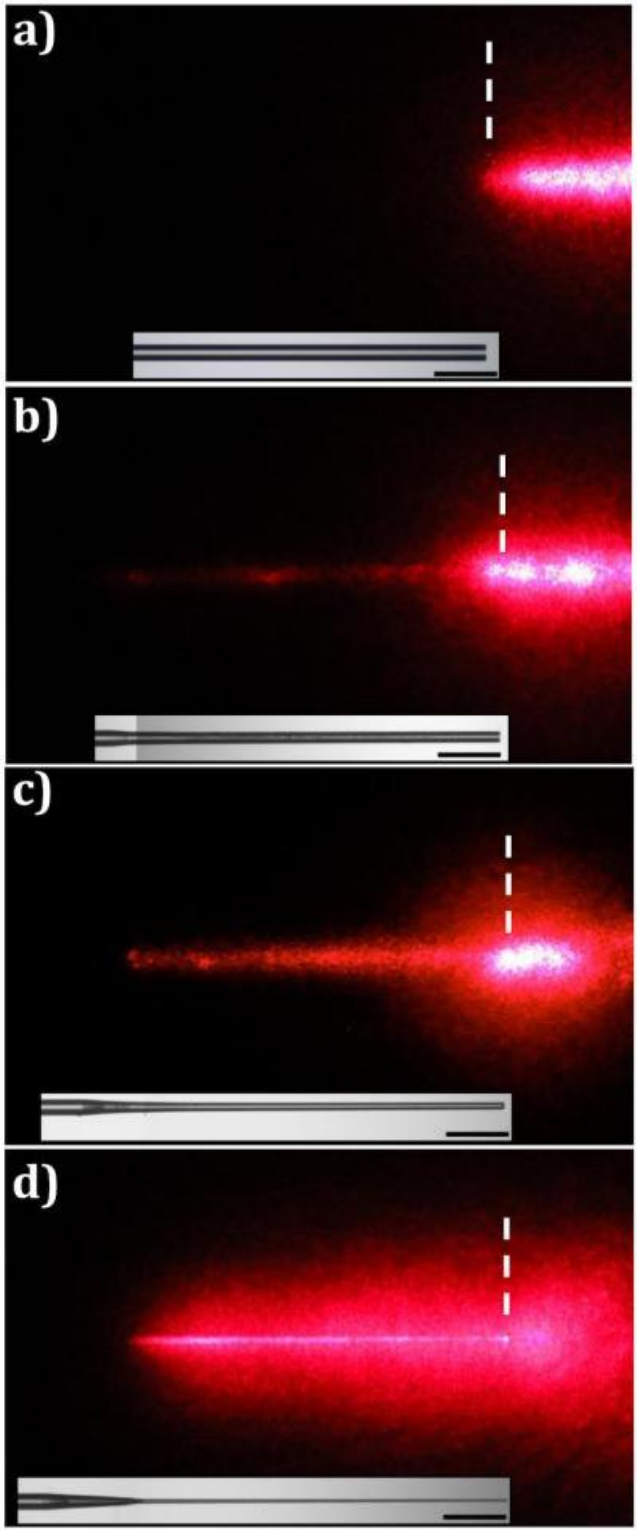

Figure 2: Images of the FMDs delivering red light: (a) flat-cleaved fiber, (b) 10 min acid immersion, (c) 30 min acid immersion (d) 50 min acid immersion

In a final study published by Kosoglu, Hood *et al.*, a novel method of laterally strengthening FMDs with an elastomeric support was investigated [19]. The critical buckling force (F_{CR}) of FMDs embedded in polydimethylsiloxane (PDMS) was compared to unsupported FMDs of the same diameter. The critical buckling force of 55, 70, and 110 µm diameter FMDs was measured to change by 610%, 290%, and 33%, respectively. Theoretical calculations by the Rayleigh-Ritz model consistently overestimated the experimentally determined strengthening, but correlated highly with the greater enhancement offered to thinner microneedles. Aided by the elastomeric reinforcement, microneedles 55 µm in diameter were able to repeatedly penetrate *ex vivo* porcine skin, a feat only demonstrated by needles at least 125 µm in diameter in a previous study by the group. A plot of the measured percentage improvements in F_{CR} are compared to the Rayleigh-Ritz model predictions (fixed-pinned assumption) is shown in Figure 3.

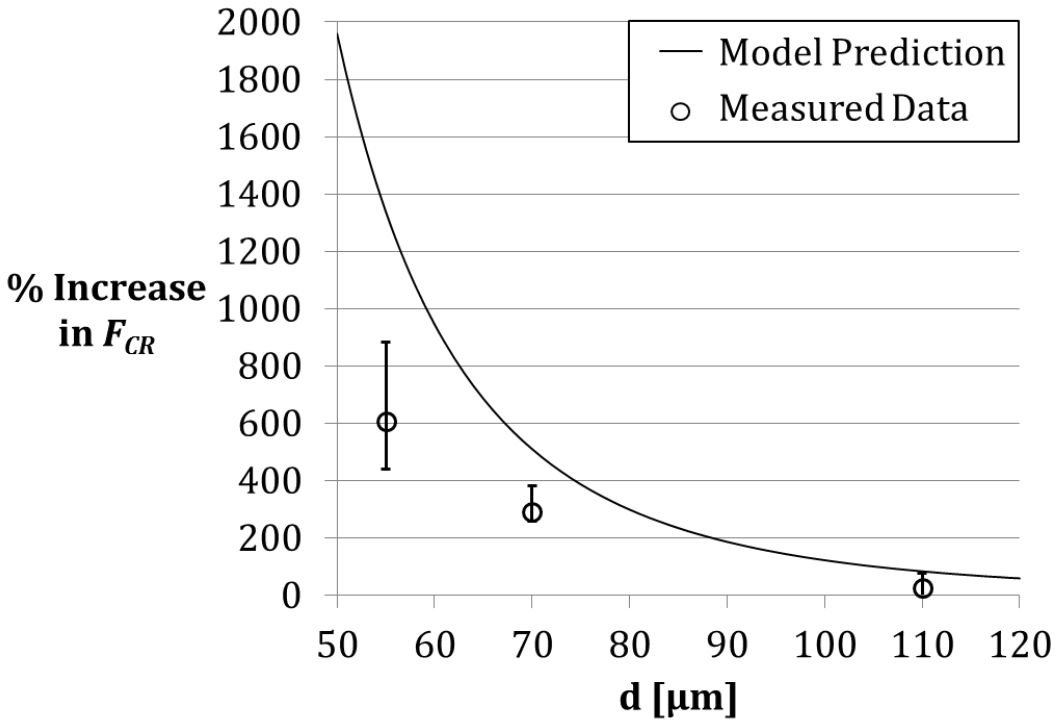

Figure 3: Rayleigh-Ritz prediction and measured percentage increase in F_{CR} provided by the PDMS support.

1.2.2 FMD Fluid Delivery and Light/Fluid Co-Delivery

Fluid-delivering FMDs were originally envisioned as melt-drawn, silica capillary tubes capable of penetrating skin tissue parallel to the light-delivering FMDs developed by Kosoglu, Hood *et al.* (cite). Early experiments (unpublished) demonstrated that silica capillary tubes (150 µm bore, 325 µm diameter) with sharp, melt-drawn tips were capable of penetrating *ex vivo* porcine skin with ease relative to their finer light-delivering counterparts. A photograph of a "hollow-core FMD" penetrating *ex vivo* porcine skin is shown in Figure 4.

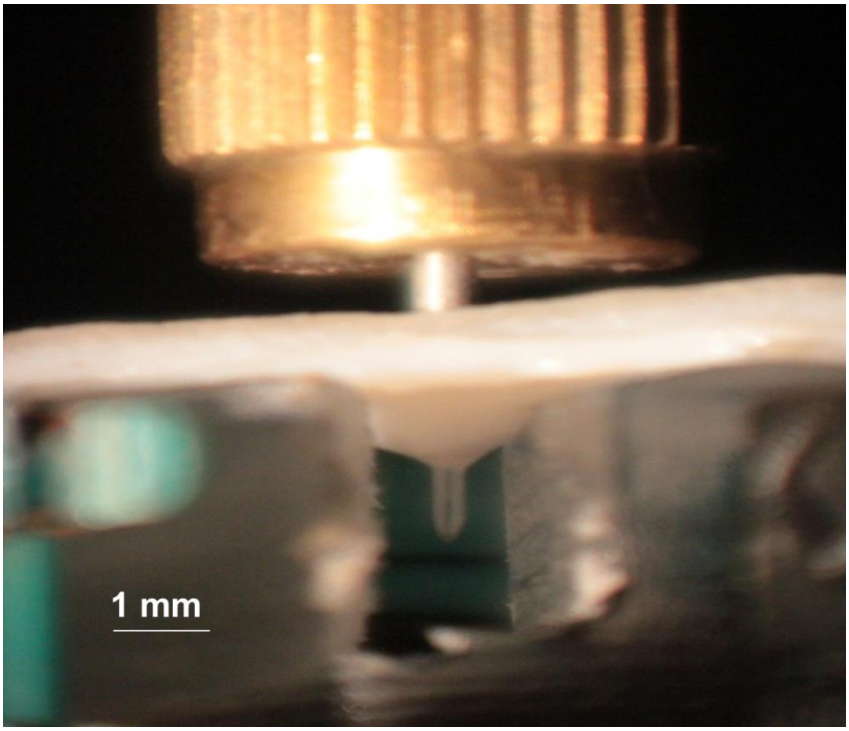

Figure 4: Hollow-core FMD penetrating *ex vivo* porcine skin.

Initial experiments (described in Chapter 2) were conducted to characterize the fluid flow properties of melt-drawn, hollow-core FMDs. Unfortunately, fluid flow behavior through converging ducts on that scale was shown to be highly irregular and unpredictable, causing a design development shift away from melt-drawn FMDs towards angle-polishing methods. Angle-polishing generates a sharp, beveled tip, highly similar to those on commercially available

hypodermic needles. Fluid flow through hollow-core FMDs with angle-polished tips was identical to that of flat-cleaved capillary tubing of the same inner diameter, simplifying flow behavior prediction (described by the Hagen-Poiseuille equation) and repeatability while easing manufacture.

Further design advancement was made through utilization of the light-guiding capillary tubing available from Polymicro Techologies. Through forming concentric core and cladding layers around a hollow bore, Polymicro developed a capillary tubing capable of total internal reflection. Initially envisioned by the company as a possible vehicle for new forms of chemical characterization, this group developed the light-guiding tubing for biomedical applications such as cancer treatment. To our knowledge, this is the first such device ever developed that enables one-tube fluid and light co-delivery to interstitial spaces at this size scale. The following sections in this chapter describe the current knowledge and treatment paradigms for transitional cell carcinoma of the bladder and malignant glioma. This manuscript describes the development of new treatments for these diseases based on the hollow-core FMD technology.

1.3 Introduction to FMD Treatment for Urinary Bladder Cancer

1.3.1 Current Treatment and Epidemiology for Urinary Bladder Cancer

Urinary bladder cancer is the fourth most common non-cutaneous malignancy of humans in the United States with approximately 71,000 new cases diagnosed and 15,000 deaths in 2010 [20]. Urothelial cell carcinoma (UCC, synonymous with transitional cell carcinoma) accounts for approximately 90% of all bladder cancers. Over 30% of UCCs are at an advanced clinical stage when diagnosed, with penetration of tumor cells into the muscularis propia (stages 3 and 4),

serosa (stage 4 only), and metastasis to surrounding organs [21-23]. Radical cystectomy of invasive UCC is the current standard treatment, but its use frequently results in significant post-operative complications and poor patient quality of life [24]. This treatment typically requires removal of the bladder, nearby lymph nodes, and part of the urethra in both sexes; the prostate, seminal vesicles, and vas deferens in men; and the ovaries, Fallopian tubes, and part of the vagina in women [24-26]. This treatment often results in sexual dysfunction, electrolyte imbalances, bone loss, and deterioration of the kidneys [27, 28]. Patients are faced with poor quality-of-life, bleak prognosis, and low survival rate (30-50% at 5 years post diagnosis) [21].

1.3.2 Alternative Photothermal Treatments for Urinary Bladder Cancer

Although patient outcomes for advanced stage, invasive bladder cancers are statistically poor, patient outcomes for early stage (stages 0-1) bladder cancers are relatively hopeful [29-31]. The primary treatment for such early lesions is transurethral resection of the bladder (TURB) followed by chemotherapy [31-36]. One of the original laser-based alternatives for treatment of superficial bladder tumors was Nd:YAG laser photoablation at a 1064 nm wavelength. Unfortunately, laser energy delivered at this wavelength is damaging to underlying tissues [29, 32, 37, 38]. Nd:YAG-based treatments were succeeded by the Ho:YAG laser (2.1 μm wavelength) for photothermal treatment of superficial bladder cancers, which has become widely utilized. Several studies have shown that treatment with the Ho:YAG laser is safe, effective, and associated with rapid patient recovery, indicating it is a viable alternative to standard TURB or electrocautery for treating early stage bladder cancer [30-32, 38].

While effective for superficial tumors, Ho:YAG laser treatment has proven ineffective for invasive, late stage bladder tumors due to insufficient light penetration into the tumor mass [30, 32, 38-40]. Light at a wavelength of 2.1 μm penetrates bladder tissue approximately 0.5 mm, which is insufficient to treat late-stage tumors that invade the muscular and serosal layers 2-4 mm into the bladder wall [32]. Inadequate delivery and heating of deep tumor volumes results in generation of poorly defined lesion boundaries and a high likelihood of tumor re-growth, recurrence, necrosis, and possible perforation of the bladder wall [28, 41].

1.4 Introduction to FMD Treatment for Malignant Glioma

1.4.1 Current Treatment and Epidemiology for Malignant Glioma

Malignant tumors of the central nervous system are the third leading cause of cancer-related deaths in adolescents and adults between the ages of 15 and 34; in children, brain tumors are the leading cause of cancer death. Among malignant glioma (MGs) variants, glioblastoma multiforme (GBM) is the most common form of malignant tumor in the central nervous system, and is associated with a mean survival time post-diagnosis of 15 months and a mortality rate exceeding 95% [42]. Common treatments for MG include surgical resection, radiatiotherapy, chemotherapy, or combinations of these three modalities [43, 44]. Prior to the development of adjunctive therapy protocols combining radiation therapy and the chemotherapeutic drug temozolomide, fewer than 5% of patients survived more than 2 years. However, neither single nor multimodality treatments are curative with the combination of adjunctive therapies improving mean survival by a few months to a rate of 26% [45]. One of the reasons for poor survival is that glioma cells typically infiltrate up to 2 cm beyond the volume of visible tumor,

making them difficult to detect and treat. Treatment of MGs is also limited by insufficient delivery of chemotherapy drugs due to the blood-brain-barrier. Thus, new methods increasing treatment specificity for MG treatment are urgently needed.

1.4.2 Introduction to Convection-Enhanced Delivery

Convection-enhanced delivery (CED) is a technique for delivering large macromolecules directly into the brain parenchyma, bypassing the blood-brain barrier [46, 47]. CED is accomplished via introduction of catheters through a burrhole in the skull to positions within and around a target tumor. This modality has been researched for treating neurodegenerative, epileptic, and neoplastic diseases [47-51]. In CED, chemotherapeutic infusate is actively pumped (flow rates range from 1-10 μL/min) into the brain parenchyma and pushed through the interstitial space [52]. Infusion is continued for up to several days before catheters are removed at the bedside [52]. In contrast to the millimeter distances obtained with simple diffusion, CED has been shown in laboratory experiments to deliver high-molecular-weight proteins 2 cm into the brain parenchyma after as little as 2 hours of continuous infusion [20]. This was accomplished without causing cerebral edema and was unaffected by capillary loss or metabolization of the macromolecule. Subsequent studies demonstrated that CED was a viable method for providing regional distribution of molecules as large as immunotoxins and radioisotope–conjugated antibodies, and even some conventional chemotherapeutic agents [23, 46, 49, 53, 54].

Although CED development seemed promising for treatment of MG, the method failed to meet required clinical endpoints in a recent Phase III FDA trial [23]. This was attributed to insufficient

distribution of chemotherapy throughout the target tumors and failure to broadly disseminate drug to the infiltrative tumor cells in the tumor periphery. The anatomical heterogeneity of the brain, only amplified in the tumor microenvironment, severely limited chemotherapy distribution [23]. While shortcomings in a clinical trial might be remedied through better implementation, the sizable biological challenges presented by intracranial neoplasms may better lend themselves to engineering solutions.

Fluid reflux, or non-ideal backflow along an inserted catheter, has primarily been addressed addressed through treatment design and engineering solutions for the catheter [55]. The first precaution against reflux taken is to maintain low volumetric flowrates for CED, usually between 1-5 μL/min. To infuse a volume that will cover several milliliters of brain volume, infusions frequently take place over timescales of 3-4 days [56]. Krauze *et al*. described a step design to avoid the backflow problem which allowed a six fold increase in flow rate compared to a standard needle/catheter design [57]. Ivanchenko and Ivanchenko presented novel catheter designs incorporating induced channels and suction ports along the needle shaft [55]. Experiments with flow rates of up to 10 μL/min were shown to have no backflow occurrence, significantly improving upon commonly used step down designs. Bobo *et al*. reported rising pressure in the injection line during the early stages of infusion due to tissue coring in the catheter blocking outflow, but observed a rapid pressure drop to a lower steady-state value once the blockage was dislodged [47]. This is similar to work conducted by Martanto *et al.,* who reported that 0.5-1.0 mm retraction of a centimeters-long microneedle inserted through *ex vivo* skin helped loosen or remove tissue coring prior to infusion [58].

1.4.3 Introduction to Thermochemotherapy

Clinical and laboratory evidence has shown that thermochemotherapy, or heating of delivered chemotherapeutic agents, is effective in increasing fluid penetration into peritoneal tumors [59]. This is an intuitive effect as both convective and diffusive fluid transport increase with increasing temperature. In addition, the cytotoxic effects of several chemotherapeutic drugs can be enhanced by adjunctive hyperthermia [60-62]. The augmented cytotoxicity has been attributed to several biological mechanisms, including plasma membrane permeabilization and amplified cell metabolism. Adjunctive hyperthermia could also increase volumetric dispersal and efficacy of chemotherapeutics delivered through CED.

1.4.4 Introduction to 0.6% by Weight Agarose Brain Tissue Phantoms

Nicholson wrote a comprehensive review on drug transport mechanics in brain tissue: from the data complied, it can be seen that brain tissue of different species can have very different fluid mechanical properties [63]. Brain phantoms mimicking the brain's mechanical and fluid conduction properties are commonly used for preliminary studies of catheter devices for brain tumor treatment, with 0.6% by weight Agarose phantoms being among the most common [64, 65]. Linninger *et al*. described the application of detailed FEM brain modeling to optimize catheter design and application parameters [64]. The group showed that utilizing diffusion tensor magnetic resonance imaging as an input for patient specific modeling allowed personalized treatment. Simple perfusion of Trypan blue dye into 0.6 % Agarose brain phantoms was used to evaluate the modeling approach. In Foley *et al.,* the application of an artificial brain phantom allows examination of a microfluidic device in a reproducible *in vitro* method [66]. Chen *et al*. reported the ratio of distribution volume to infusion volume of Agarose is 10 compared with 7.1 for brain [65]. The manuscript also described infusion pressure in agarose comparable in

distribution and magnitude to that of the brain and that the diffusion characteristics of common MRI agents were similar [65].

1.4.5 Introduction to Laser-Induced Thermal Therapy

Laser-based treatment modalities, such as laser-induced interstitial thermal therapy (LITT), have received much research attention for development into alternative treatments for brain tumors [67-71]. LITT is a procedure wherein tumor tissue is destroyed through photothermal heat generation, accomplished through percutaneous introduction of light-conducting fiberoptics local to a target tumor [68]. LITT's minimally invasive nature and fiberoptic presentation infer a high degree of compatibility with magnetic resonance imaging, benefitting especially from magnetic resonance thermometry (MRT) [69, 72]. MRT enables real-time identification of thermal gradients, allowing LITT to be adapted to tumor geometry and dynamic surgical conditions. However, LITT's efficacy is limited by the unpredictability of thermal gradients due to the heterogeneity of brain tissue, which is only increased by the presence of a solid tumor [70, 73]. Additionally, ablative therapies cause edema, which can be a dangerous side effect when trying to preserve critical cerebral structures [74, 75].

1.5 Project Overview

The focus of this project was to develop the FMD as a technology suitable for the treatment of invasive, solid tumors. The three major advantages offered by the FMD are: 1) microneedle penetration through the exterior of the tissue to deliver therapy interstitially throughout the thickness of a tumor; 2) the FMD can be used to present chemotherapy, image-enhancing molecules, photosensitizers, or any other clinical molecule that can be presented as a fluidic solution to an interstitial space; and 3) the FMD can deliver light interstitially for light-based therapies or collect light for imaging. As the microneedles are made from capillary tubes (both

light-guiding and not), the initial challenge to development was the characterization of fluid flow through the microneedle tip. Once the fluid delivery was understood, invasive bladder cancer was the first application the FMD was customized to treat. Development of the FMD for treating malignant glioma became the next research application, and is the primary focus of this manuscript. The research described below addresses the fluid delivery characterization, design modifications introduced to create a FMD applicable to bladder and brain cancer treatments, experimental testing of the resulting device, and modeling and quantification of correct treatment parameters for different target diseases.

Chapter II: Effects of Microneedle Design Parameters on Flow Rate and Hydraulic Resistance

2.0 Abstract

Microneedles have been an expanding medical technology in recent years due to their ability to penetrate tissue and deliver therapy with minimal invasiveness and patient discomfort. Variations in design have allowed for enhanced fluid delivery, biopsy collection, and the measurement of electric potentials. Our novel microneedle design attempts to combine many of these functions into a single length of silica tubing capable of both light and fluid delivery terminating in a sharp tip of less than 100 microns in diameter. This chapter focuses on the fluid flow aspects of the design, characterizing the contributions to hydraulic resistance from the geometric parameters of the microneedles. Experiments consisted of measuring the volumetric flow rate of de-ionized water at set pressures (ranging from 69-621 kPa) through a relevant range of tubing lengths, needle lengths, and needle tip diameters. Data analysis showed that the silica tubing (~150 micron bore diameter) adhered to within ±5% of the theoretical prediction by Poiseuille's Law describing laminar internal pipe flow at Reynolds numbers less than 700. High hydraulic resistance within the microneedles correlated with decreasing tip diameter. The hydraulic resistance offered by the silica tubing preceding the microneedle taper was approximately 1-2 orders of magnitude less per unit length, but remained the dominating resistance in most experiments as the tubing length was >30 mm. These findings will be incorporated into future design permutations to produce a microneedle capable of both efficient fluid transfer and light delivery.

2.1 Introduction

In recent years, developments in microscale fabrication have enabled the creation of needles on the scale of micrometers. These “microneedles” can be created out of a variety of materials such as polymers, metals, or glass, and are utilized to facilitate highly accurate small volume fluid delivery with minimal tissue disruption. Studies have shown that needle diameter and insertion force are primary determinants of patient pain caused by transdermal injection [1-3]. The small diameter of these microneedles reduces the invasiveness and patient sensation associated with their clinical use. The potential presented by these microneedles for therapeutic and diagnostic applications has led to a significant investment of research attention.

One of the first therapeutic applications utilizing microneedles was increasing the effectiveness of transdermal drug delivery patches by increasing skin permeability with slight penetration (< 1 mm) [4]. Other applications involved using microneedles as electrodes to measure electrical potentials or cause electroporation in tissue [5-7] Other groups have successfully utilized these needles for intrascleral delivery of therapeutic agents and to inoculate patients against disease [8, 9]. Solid, biodegradable polymer microneedles containing dissolved pharmaceuticals have been developed for time-delayed drug release [10-12]. Due to the lessened patient discomfort associated with microneedles, they have been developed for use in patients with conditions that require frequent infusions, such as diabetics [13]. However, the small diameters of microneedles make delivery of larger volumes difficult. To bypass this difficulty, parallel arrays of microneedles can be utilized. Early developers of this design successfully delivered sufficient insulin to lower glucose levels in diabetic rats [13, 14]. In a more refined variant of the parallel array design, one group developed a microneedle-based transdermal patch device that allowed

for the active dispensation of insulin [15]. Microneedles are continuing to receive a great amount of research attention, with new designs being applied to novel applications in many diverse fields.

The research described in this paper focuses on fluid flow characterization through a novel type of hollow-core silica microneedle that allows for several millimeters of tissue penetration and co-localized light and fluid delivery. These microneedles can be made from silica capillary tubing capable of guiding laser light. A device with this dual capability can be readily adapted to several applications, such as treatment of non-superficial, focal cancers by delivery of exogenous chromophores and laser irradiation from the same probe. Cosmetic laser-based applications such as body contouring may also benefit from this technology through simultaneous fat liquefaction and removal from sensitive areas such as the face.

Our fiberoptic microneedle design incorporates tubing of an inner bore diameter of 150±1 μm with a fabricated microneedle tip with diameter ranging between 20-100 μm. The sharpened tip is necessary to lower the force required for penetration and thereby safeguard the structural integrity of the needle, in addition to minimizing patient discomfort [3, 76]. Our design is biomimetic, as the mosquito's proboscis is of similar proportions and is able to painlessly penetrate millimeters into an animal's skin to extract blood [77]. These microneedles can be incorporated into many applications that require accurate localized delivery of small fluid volumes. The experiments performed in this study characterized the fluid flow properties of this transformative microneedle design so that it may be easily integrated into devices for a range of

applications. More specifically, the experiments sought to determine the most important factors contributing to the hydraulic resistance to fluid flow in this design.

2.2 Methods

2.2.1 Manufacturing Process for Hollow-Core Microneedles

Commercially available flexible fused silica capillary tubing was utilized in the characterization of the fluid properties for our design. The fused silica capillary tubing had an outer diameter of 363±4 μm, an inner diameter of 150±1 μm, and a coating thickness of 40 μm (Polymicro Technologies, Phoenix, AZ). The microneedle fabrication method outlined below is similar to that described in a previous publication by Kosoglu *et al.* for solid-core microneedles [76]. To begin the fabrication process, the protective polyimide jacket (40 μm coating) was removed from the silica tubing through soaking in a warmed sulfuric acid (~130^{o} C) bath for 15 minutes. The silica was drawn into a microneedle geometry by simultaneously heating the tubing with a CO_2 laser (wavelength, λ = 10.6 μm) to silica's melting temperature (~1650^{o}C) while stretching it with a linear stage providing uniaxial tension (~0.2 - 1 mm/s, manually translated). The drawing speed was intentionally varied to fabricate tip diameters ranging from 30-75 μm. Microscope images of several representative hollow-core microneedles are shown in Figure 5.

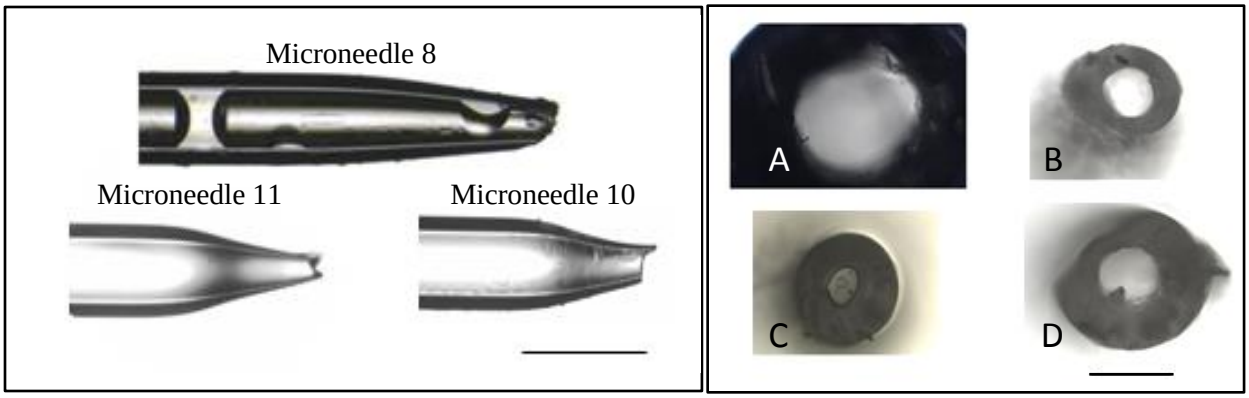

Figure 5: Left) Three sample hollow-core microneedles. The scale bar represents 500 µm. Water within the needle's bore can be seen in the image of microneedle 8. Right) *En face* images of the tips of A) flat-cleaved tubing B) needle 10 C) needle 11 D) needle 13. Scale bar represents 100 µm.

2.2.2 Hydraulic Circuit Analysis

In order to determine the most important factors contributing to hydraulic resistance, an experimental approach utilizing two successive stages was developed. Stage I consisted of characterizing the hydraulic resistance of the tubing that would precede the microneedle, while Stage II sought to characterize the resistance of the microneedle itself. This approach can be modeled via hydraulic circuit analysis as outlined by Kirby [78]. In Stage I, the hydraulic resistance of the flat cleaved tubing (150 µm inner diameter) was tested. The experiment consisted of using pressured CO_2 to drive deionized water through the tubing into atmospheric pressure. Laminar internal flow through a pipe is described by Poiseuille's Law as

$$R_{TUBE} = \frac{\Delta P}{Q} = \frac{128\,\mu L}{\pi D^4} \tag{2}$$

where R_{TUBE} is the hydraulic resistance (Pa·s/µL), ΔP is the pressure difference (Pa), Q is the volumetric flow rate (µL/s or mm^3/s), D is the pipe's diameter (mm), µ is the dynamic viscosity ($N{\cdot}s/m^2$), and L is the length of the pipe or tube (mm). The hydraulic circuit analytical model of a tube with a single (lumped) resistance is representated in Figure 6. To facilitate better physical

understanding and ease of calculation, the units for hydraulic resistance were input pressure divided by the measured volumetric flowrate (Pa·s/µL) and were reported as such in this chapter.

In Stage II, the hydraulic resistance of a length of tubing with an attached microneedle was tested via the same method as Stage I. As the resistance provided by the initial tubing (R_{TUBE}) would be understood after the completion of Stage I, the series resistance provided by the microneedle (R_{NEEDLE}) could be isolated and quantified (depicted in Figure 6). The total hydraulic resistance can then be described mathematically by

$$R_{TUBE} + R_{NEEDLE} = \frac{\Delta P}{Q} = R_{TOTAL} \quad (3)$$

where R_{TUBE} describes the resistance to flow due to the tubing length preceding the microneedle, R_{NEEDLE} is the resistance provided by the microneedle, and R_{TOTAL} is the total resistance. Assuming these resistances are linear and ideal (no capacitance or inductance), this equation should describe the ideal case of flow defined by viscous forces alone (limited inertial effects) through the microneedle design.

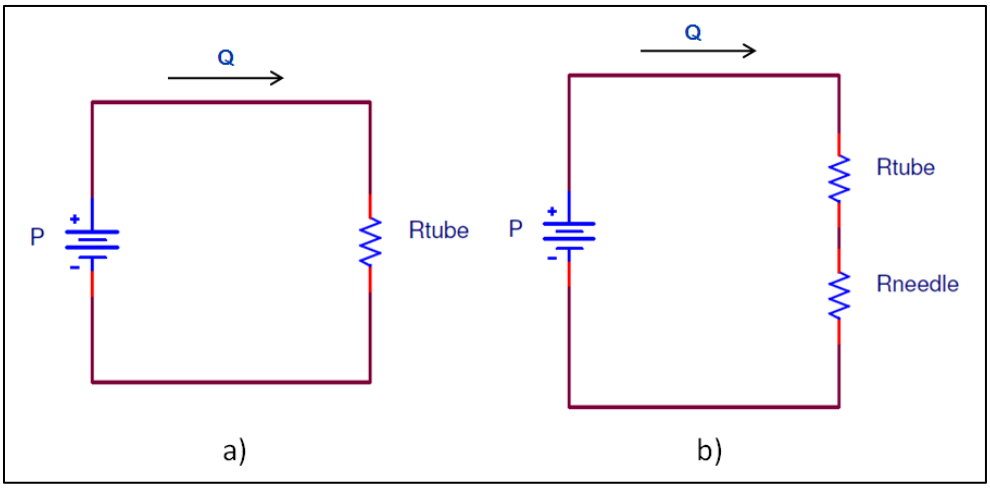

Figure 6: Hydraulic circuit analytical model representation of resistance in a) a capillary tube (Stage I) and b) tube with a microneedle tip (Stage II).

To correctly interpret results obtained via this experimental model, an understanding of the flow turbulence in the tubing and microneedles was important. The dimensionless Reynolds number describes this effect, and is calculated for internal pipe flow by:

$$\mathrm{Re} = \frac{\mathrm{QD}}{\upsilon \mathrm{A}} \tag{4}$$

where Re is the Reynolds number, ν is the kinematic viscosity (m^2/s), and A is the cross-sectional area of the pipe (m^2). For Stage II, the Reynolds number increased along the length of the needle towards the tip as the diameter decreased.

2.2.3 Hydraulic Resistance Experiments

A simple fluid deployment device (FDD) was fabricated as shown in Figure 7 to allow for variable input pressures and have negligible hydraulic resistance relative to the tubing or microneedles being tested. The individual components of the device consisted of brass and stainless steel piping, ball valves, inline filter (10 micron in-line filter, FloLok®, Twinsburg, OH), a Luer Lock adapter (1/4 NPT male to Luer Lock, Ellsworth Adhesives, Germantown, WI), and an 18G hypodermic needle (0.838 mm inner diameter). The filter minimized clogging of the needles, and the adapter enabled rapid removal and replacement of different tubing sections and microneedles. The volumetric flow rate of water through the FDD was measured by timed collection and weighing of DI water exiting the FDD. The resistance through the FDD alone (without tubing or microneedle attached) was calculated to be between 2 and 3 orders of magnitude less than the test resistances, which was further observed experimentally. This evidence indicated that the FDD presented an insignificant series resistance that would be constant across all experiments. The different lengths of flat cleaved tubing and microneedle-

tipped tubing were epoxy-bonded into 18 gauge hypodermic needles (1.067 mm inner diameter) for interface with the FDD. Excess tubing length extended through the Luer-Lok adapter into the setup, ensuring that the syringe needle did not contribute to the hydraulic resistance of the system. The bonding epoxy served to both fix the tubing in the hypodermic needle and prevent potential leaks. Any leakage from the device or hypodermic immediately invalidated the relevant experiment.

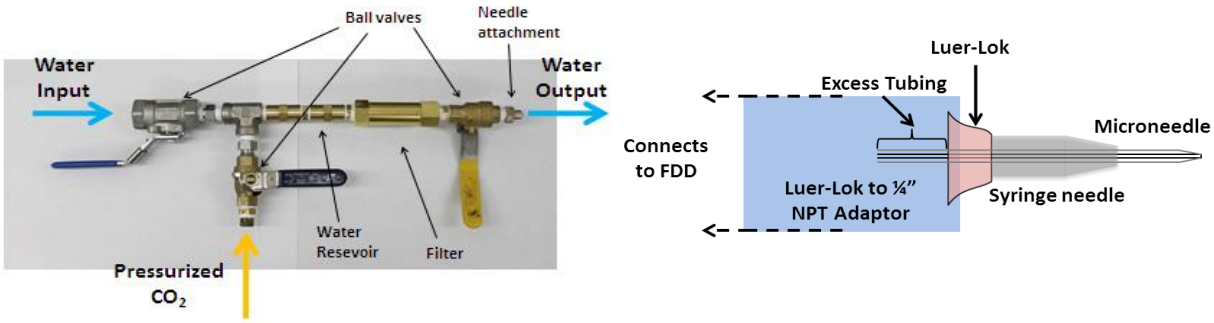

Figure 7: The left image shows the fluid deployment device (FDD) with specific components labeled. The right image shows a schematic of the microneedle coupling. The microneedle is epoxy-bonded into an 18G syringe needle, which couples to a Luer-Lok to ¼" NPT adaptor at the distal end of the FDD.

The experimental preparation was identical for Stages I-II. De-ionized water was added to the FDD (10-15 mL) and any air was bled from the system. Next, the FDD was pressurized to the desired experimental level by a CO_2 tank and regulator setup. For both stages, the weight of a small beaker (50 mL volume) was tared on an analytical balance with 0.1 mg (or 0.1 µL of water) accuracy. The beaker was used to capture flow through the test resistance. Once the

empty beaker was in position, the valve directly adjacent to the test resistance was opened, allowing fluid flow through the resistance and into the beaker.

Exiting water was captured for a set time (30 s) and then immediately taken to the balance for weighing to determine the fluid flow rate. While evaporation was insignificant (around 0.8 µL/min) relative to total captured volume (2-5 mL), rapidly weighing the beaker immediately after timed capture ensured that the effect of evaporative water loss was minimized. The experimental test pressures used for both stages ranged from 69 to 621 kPa (10-90 psi). For Stage I, 6 different tubing lengths were tested at each of the experimental pressures 3 or more times. For Stage 2, 15 different microneedles with different tubing length precursors were tested 5 or more times at each experimental pressure.

Both partial and complete clogging of the needles was observed infrequently during the Stage II experiments. Microneedles were observed under a microscope prior to experimentation to detect any flow obstruction. The experiments were conducted on each microneedle with incrementally increasing pressure, so any sudden drop in flow rate caused by flow obstruction was immediately evident. Any microneedle observed to have an obstruction was immediately removed from testing and cleared through deployment of a solvent (ethanol or acetone) through the needle. The previous data was discarded and the relevant experiments repeated for the cleared microneedle.

2.3 Results

2.3.1 Stage I Experimental Results

Flow rate was measured through different lengths of flat-cleaved tubing to measure the hydraulic resistance (R_{TUBE}). By conducting the experiments over a range of input pressures, graphs of flow rate versus pressure were generated and are presented in Figure 8.

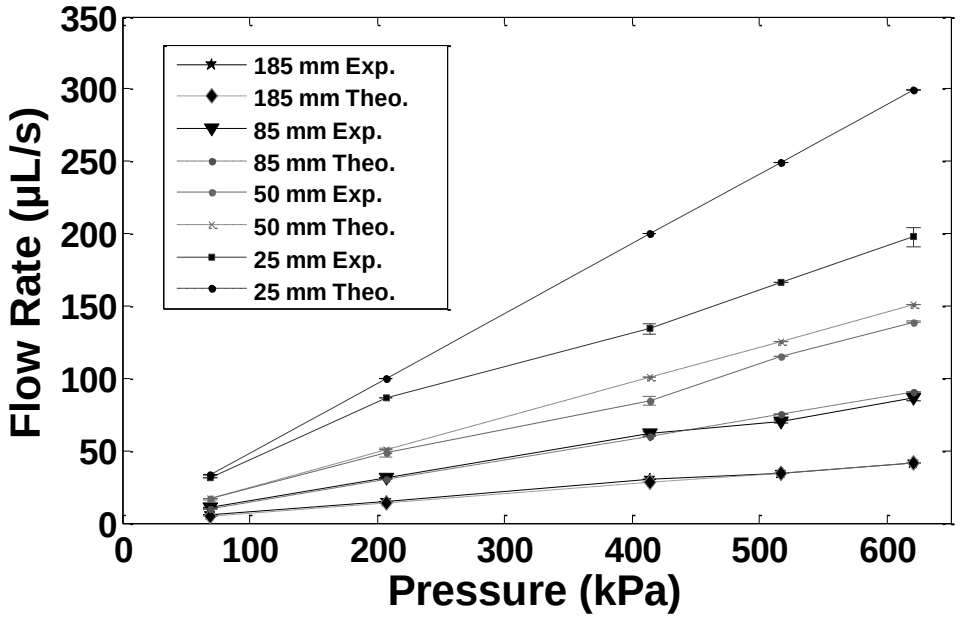

Figure 8: Graph of pressure versus volumetric flow rate for different lengths of straight tubing in Stage I. Both experimental data and theoretical values predicted by Poiseuille's Law are shown. Experiments were conducted at N=5 for each length of tubing.

Using the experimental data, resistance values were calculated for the different tubing lengths and compared to resistances predicted by Poiseuille's Law. Calculation of the tubing resistance from the pressure and flow rate data using Eqn. (1) yielded the results shown in Table 1.

Table 1: Resistance values calculated from Stage I experiments compared to the theoretically predicted values provided by Poiseuille's Law. Resistance units are in Pa·s/µL.

Tube Length	185 mm	125 mm	85 mm	70 mm	50 mm	25 mm
Experimental R_{TUBE}	15647	10764	7305	6010	4577	3439
Poiseuille R_{TUBE}	14926	10085	6858	5406	4115	2072
% Difference	4.83%	6.72%	6.51%	11.2%	11.2%	66.0%

2.3.2 Stage II Experimental Results

Graphs of pressure versus volumetric flow rate for tubing with attached microneedles are provided in Figure 9. The selected microneedles represent the range of volumetric flow rates measured. The total hydraulic resistance of tubing with microneedle tips was calculated from this experimental data.

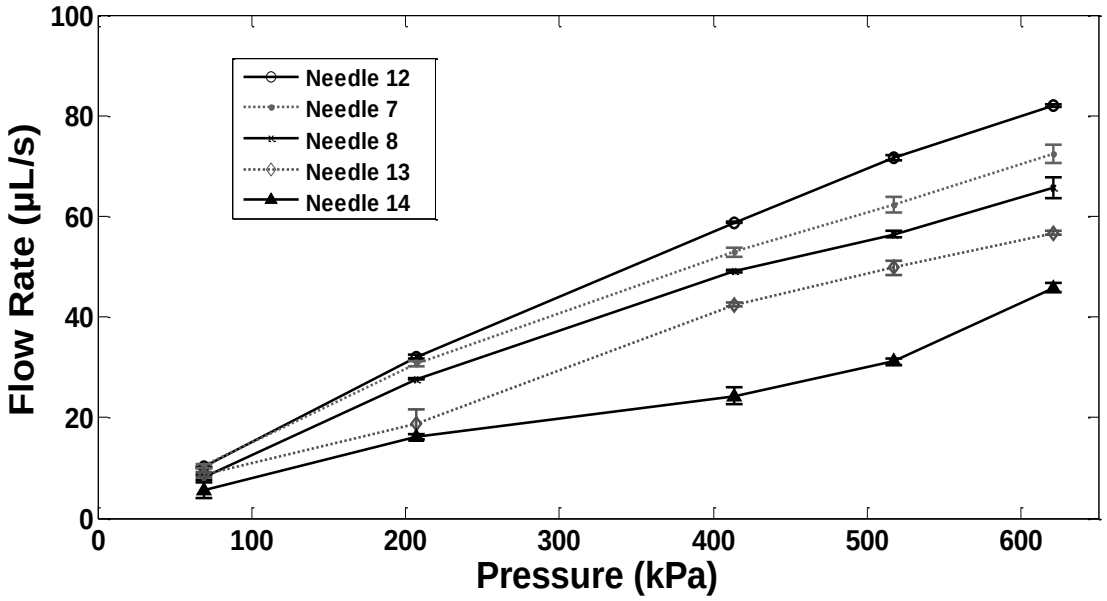

Figure 9: Measured flow rate versus pressure for tubes and microneedles. Error bars are included on all points, but do not extend outside the marker in some cases. Experiments were conducted with N=5 for each microneedle.

The hydraulic resistance associated specifically with the microneedle tip could be determined from Eqn. (1) ($R_{NEEDLE} = R_{TOTAL} - R_{TUBE}$), where R_{TUBE} is theoretically predicted using Poiseuille's Law. For Microneedles 1-15, the needle resistance ranged from 990 to 8230 Pa·s/µL at 207 kPa. High resistance correlated moderately with decreasing tip size.

Geometric parameters of fabricated microneedles (including length and taper angle) were described previously by this group [76]. The microneedles generally resembled straight-sided cones with linearly decreasing cross-sections. Needle measurements were taken from images recorded with a Leica DMIL LED light microscope (Leica Microsystems, Wetzlar, Germany) on the brightfield setting. Both sideview and *en face* images were measured and compared to ensure

accuracy as shown previously in Figure 5. The geometric parameters and experimentally measured resistances for the different microneedles are shown in Table 2.

Table 2: Geometric parameters and the experimentally measured resistances of the fourteen microneedles tested.

Needle #	Tube Length (mm)	Needle Length (μm)	Tip Diameter (μm)	Taper Angle (degrees)	R_{Needle} @ 207 kPa (Pa·s/μL)
1	70	410	75	5.2^{o}	990
2	30.5	496	59.7	5.2^{o}	1100
3	77.5	1015	68.3	2.3^{o}	1180
4	83	1116	40	2.8^{o}	1800
5	60.5	307	75.3	6.9^{o}	1860
6	69.5	683	61.5	3.7^{o}	1920
7	68	1152	66	2.1^{o}	2040
8	77	516	70	4.4^{o}	2110
9	69.5	997	71	2.3^{o}	2270
10	56.5	698	38.1	4.6^{o}	3280
11	60	701	38	5.5^{o}	4130
12	46.5	541	40	5.8^{o}	4880
13	38	634	50	4.5^{o}	5690
14	58	724	30	4.7^{o}	8230

2.4 Discussion

Based on the experiments determining the flow rate through the hollow tubes, we calculated the Reynolds numbers for each experiment to determine the validity of Poiseuille's Law as a model for our tubing. The range of Reynolds numbers for the Stage I experiments varied from 50 to 1675, indicating that flow through the shortest tubing lengths at the highest pressures exhibited both viscous and inertial traits. As our Poiseuille's Law model is based on ideal laminar pipe flow, its prediction of the hydraulic resistance should be less than that observed experimentally. As Table 1 indicates, Poiseuille's Law was not an accurate predictor (>5% deviation) for the flow resistance through tubing (without a microneedle tip) at Reynolds numbers greater than 700. In contrast, the high resistance provided by microneedles kept the flow in the tubing preceding the needle within a lower Reynolds number range ($100<Re<500$) in all of the Stage II experiments, allowing Poiseuille's Law to be an accurate model for the tubing.

For the Stage II experiments, the hydraulic resistance for the microneedles increased significantly with increased pressure, with an average increase of 33% from 69 to 620 kPa. This was likely due to increased turbulence in the fluid flow near the sharpest point of the needle, as the Reynolds numbers at the microneedle tips approached 3600 (well above the onset of transitional flow at Re = 2100) for the smallest tip diameter (30 μm) at the highest pressure (621 kPa) [79]. Hydraulic resistance at 207 kPa was chosen as the metric with which to compare different microneedles, as flow at 69 kPa was not continuous (dripping) for some of the higher resistance needles and pressures greater than 207 kPa exhibited increasingly transitional flow. In addition, Reynolds numbers calculated for the tubing sections at this pressure in Stage II fell within the range of 50-500 Pa·s/μL, indicating laminar flow and adherence to Poiseuille's Law.

Comparing the hydraulic resistances at 207 kPa allowed for better isolation of the direct effects of geometry on fluid flow.

Entrance length for each tubing and microneedle were calculated to determine its effects. An approximate value for entrance length of developing flow can be calculated with Eqn. 4

$$\left(\frac{Entrance\ Length}{Hydraulic\ Diameter}\right)_{Laminar\ Flow} = 0.05\ \mathrm{Re} \tag{5}$$

which relates the entrance length, hydraulic diameter, and Reynolds number for laminar internal pipe flow [80]. For the Stage I experiments, the longest entrance length (25 mm tube, 620 kPa) was found to be 12.7 mm. Using flow analysis outlined by Zahn et al., the pressure drop along this entrance length was found to be ~13 % of the total pressure drop, suggesting entrance effects significantly contributed to the discrepancies between Poiseuille's Law predictions and the experimental measurements in the Stage I experiments [81]. However, due to the higher overall resistance added by the microneedle tips in Stage II and the chosen comparison pressure of 207 kPa, the longest entrance length among the microneedles was found to be 3.7 mm. Since tubing with attached microneedles were $\geq$ 25 mm in length, these calculations suggest that the entrance effects for the Stage II experiments were negligible as the flow reaches a fully-developed state preceding the microneedles, thus supporting the use of Poiseuille's Law as a model for the straight tubing portion of the microneedle.

Data gathered in this study was consistent with the established literature on the flow behavior in conically-tapered microneedles in that small forces (such as capillarity) did not influence flow behavior significantly [82, 83]. As hydraulic resistance was most sensitive to tip diameter, future design iterations may include a conically beveled microneedle tip. Fortunately, the data gathered

in these experiments should also predict flow from a beveled tip, as the diameter of the closed tube before the spread of the bevel should behave similarly to the flat microneedle tips from this study.

Poiseuille's Law predicts a tubing hydraulic resistance of 80.7 Pa·s/µL per mm for the straight tubing used in these experiments. Thus, the total tubing resistance theoretically varies from 2100 Pa·s/µL to 15000 Pa·s/µL for lengths between 25 and 185 mm. The microneedle hydraulic resistance values measured in Stage II ranged from 990 to 8230 Pa·s/µL at 207 kPa. This finding indicates that fluid flow through the tubing should be kept at a minimum length as this design continues in development, an important concept as some tubing length may be necessary for successful coupling of both light and fluid into the same microneedle.

Hydraulic resistance tended to be highest for needles with small tip diameters. This is illustrated in Figure 10. The average resistance for needles with tip diameters between 30-55 µm was approximately 4270±2260 Pa·s/µL, while average resistance for needles between 55-90 µm was 1680±510 Pa·s/µL. As can be seen in Figure 5, the resistance for tip diameters less than 55 µm tends to be higher, but the data has significantly more spread. This data spread can be attributable to the greater influence of surface irregularities on the inner bore surface of the needle or the increased flow alteration due to minor clogging. The microneedles with <55 µm tip diameters were shown to be of significantly greater in hydraulic resistance than the microneedles with >55 µm by a Welch's t-test with 95% confidence**.**

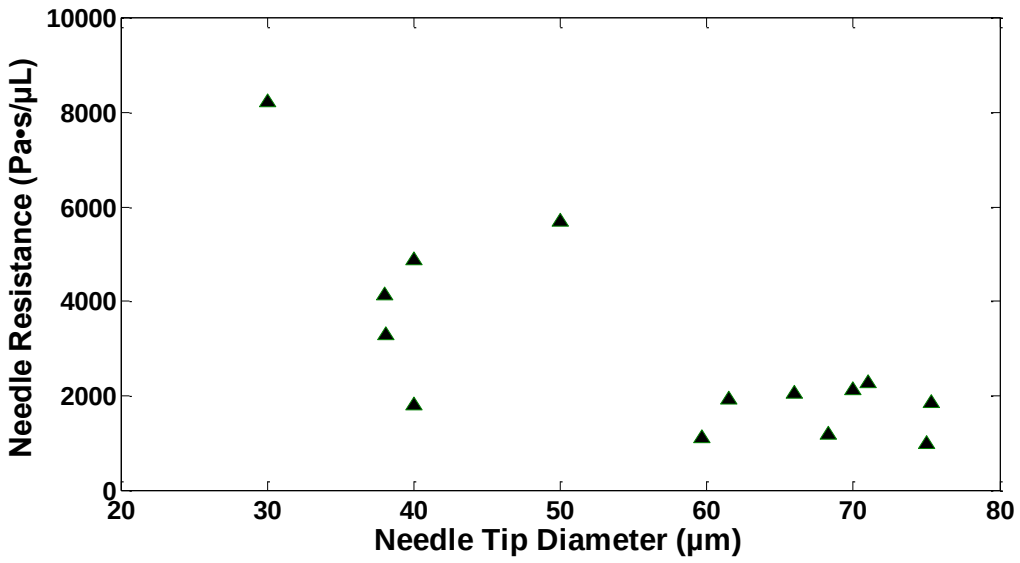

Figure 10: Hydraulic resistance of the fourteen microneedles plotted against their tip diameters.

This paper presents a transformative microneedle design capable of co-delivering fluid and light several millimeters beneath a tissue's surface. Parallel work to characterize the light delivery capacity of these microneedles is currently underway. This chapter focuses on experiments investigating the needles' hydraulic resistance to fluid flow. For straight tubing with an inner bore of 150 µm and a length greater than 50 mm long, Poiseuille's Law was shown to be accurate within 12% of experimental data for the pressure range of 69-517 kPa. The hydraulic resistance of microneedles manufactured through our method greatly increased the resistance per unit length of the silica capillary tubing. Comparison between different needle design geometries indicated that tip diameters <55 µm cause a significant increase in hydraulic resistance. Tubing length should be kept to a minimum and tip diameter should be increased to the largest possible size to reduce overall resistance. Future investigations should also consider the resistance to flow by the tissue at the microneedle tip, as this is important for future clinical translation. Similar experiments with these microneedles *in vivo* will accelerate translation of their use to clinical practice. To achieve reasonably low hydraulic resistances in clinical practice, parallel arrays of

these microneedles could deliver fluids simultaneously at lower pressures. This concept has been demonstrated by other groups, and could be readily incorporated into our design [13, 15].

Chapter III: Spatially Controlled Photothermal Heating of Bladder Tissue Through Single-Walled Carbon Nanohorns Delivered with a Fiberoptic Microneedle Device

3.0 Abstract

Laser-based photothermal therapies for urothelial cell carcinoma (UCC) are limited to thermal ablation of superficial tumors, as treatment of invasive lesions is hampered by shallow light penetration in bladder tissue at commonly used therapeutic wavelengths. This study evaluates the utilization of sharp, silica, fiberoptic microneedle devices (FMDs) to deliver single-walled carbon nanohorns (SWNHs) serving as exogenous chromophores in conjunction with a 1064 nm laser to amplify thermal treatment doses in a spatially controlled manner. Experiments were conducted to determine the lateral and depth dispersal of SWNHs in aqueous solution (0.05 mg/mL) infused through FMDs into the wall of healthy, inflated, *ex vivo* porcine bladders. SWNH perfused bladder regions were irradiated with a free-space, CW, 1064 nm laser in order to determine the SWNH efficacy as exogenous chromophores within the organ. SWNHs infused at a rate of 50 µL/min resulted in an average lateral expansion rate of 0.36 ± 0.08 cm^2/min. Infused SWNHs dispersal depth was limited to the urothelium and muscular propria for 50 µL/min infusions of 10 minutes or less, but dispersed through the entire thickness after a 15 minute infusion period. Irradiation of SWNH perfused bladder tissue with 1064 nm laser light at 0.95 W/cm^2 over 40 seconds exhibited a maximum increase of approximately 19 °C compared with an increase of approximately 3 °C in a non-perfused control. The results indicate that these silica FMDs can successfully penetrate into the bladder wall to rapidly distribute SWNHs with some degree of lateral and depth control and that SWNHs may be a viable exogenous chromophore for photothermal amplification of laser-based UCC treatments.

3.1 Background and Objectives

Urinary bladder cancer is the fourth most common non-cutaneous malignancy of humans in the United States with approximately 71,000 new cases diagnosed and 15,000 deaths in 2010 [31]. Urothelial cell carcinoma (UCC, synonymous with transitional cell carcinoma) accounts for approximately 90% of all bladder cancers. Over 30% of UCCs are at an advanced clinical stage when diagnosed, with penetration of tumor cells into the muscularis propria (stages 3 and 4), serosa (stage 4 only), and metastasis to surrounding organs [21, 22, 32]. Radical cystectomy of invasive UCC is the current standard treatment, but its use frequently results in significant post-operative complications and poor patient quality of life [24]. This treatment typically requires removal of the bladder, nearby lymph nodes, and part of the urethra in both sexes; the prostate, seminal vesicles, and vas deferens in men; and the ovaries, fallopian tubes, and part of the vagina in women [24-26]. This treatment often results in sexual dysfunction, electrolyte imbalances, bone loss, and deterioration of the kidneys [27, 28]. Patients are faced with poor quality of life, bleak prognoses, and low survival rates (30-50% at 5 years post diagnosis) [21].

Although patient outcomes for advanced stage, invasive bladder cancers are statistically poor, patient outcomes for early stage (stages 0-1) bladder cancers are relatively optimistic [29-31]. The primary treatment for such early lesions is transurethral resection of the bladder (TURB) followed by chemotherapy [31-36]. TURB describes the introduction of a cystoscope through the urethra to debulk a tumor via excision, radiofrequency ablation, electrocautery (ablation through resistive heating of a wire probe), or laser ablation. The major advantages provided by laser ablation include high precision and significantly reduced bleeding [32, 84]. One of the original laser-based alternatives for treatment of superficial bladder tumors was Nd:YAG laser tissue

coagulation at a 1064 nm wavelength. Unfortunately, laser energy delivered at this wavelength is highly penetrating through bladder tissue and can damage surrounding organs [29, 32, 37, 38]. Nd:YAG-based treatments were succeeded by the Ho:YAG laser (2.1 μm wavelength) for photothermal treatment of superficial bladder cancers, which has become widely utilized. Several studies have shown that treatment with the Ho:YAG laser is safe, effective, and associated with rapid patient recovery, indicating it is a viable alternative to surgical excision or electrocautery for treating early stage bladder cancer [30-32, 38].

While effective for superficial tumors, Ho:YAG laser treatment has proven ineffective for invasive, late stage bladder tumors due to insufficient light penetration into the tumor mass [30, 32, 38-40]. Light at a wavelength of 2.1 μm penetrates bladder tissue approximately 0.5 mm, which is insufficient to treat late stage tumors that invade the muscular and serosal layers 2-4 mm into the bladder wall [32]. Inadequate delivery and heating of deep tumor volumes results in generation of poorly defined lesion boundaries and a high likelihood of tumor recurrence, necrosis, and possible perforation of the bladder wall [28, 41]. As 2.1 μm light is too superficial for treating more invasive tumors and 1064 nm light is too penetrating, the use of exogenous chromophores in conjunction with 1064 nm light could enable spatial control of the photothermal effect at the depths necessary for treatment of late stage neoplasms.

Single-walled carbon nanohorns (SWNHs) have recently attracted attention as photoabsorbers and intracellular delivery vehicles for therapeutic drugs and imaging moieties [85, 86]. Carbonaceous nanoparticles absorb light in the near-infrared region, and can cause cell death through photothermal hyperthermia [85]. One of the most important advantages SWNHs have

over similar carbon nanoparticles is that they are produced without the use of metal catalysts, significantly lowering their cytotoxicity [87-89]. Other advantages include highly consistent particle size and a lower aspect ratio with respect to single- and multi-walled nanotubes. Additionally, SWNHs have been demonstrated to produce reactive oxygen species when heated, which implies their use may also leverage photochemical effects to destroy tumors [90, 91].

Recognizing the limitations of current laser-based treatments for bladder cancer and the therapeutic potential of some newly developed nanomaterials, this study evaluates the use of a silica fiberoptic microneedle device (FMD) for delivering SWNHs serving as exogenous chromophores in conjunction with a 1064 nm laser to selectively amplify thermal treatment doses in deeper tissue regions. The FMD technology is being developed to co-deliver laser energy and fluid agents through the hollow silica fibers, but this chapter will be describing experiments defining the fluid delivery aspect. A literature value of 2 cm^2 for a relevant tumor area laterally across the bladder wall's surface was identified as an experimental goal for SWNH dispersal [38]. For this study, the objectives was to use the FMDs to penetrate the serosa of an *ex vivo* bladder into the muscularis and infuse a sufficient volume of SWNHs through its 150 μm bore to permeate a clinically significant area (2 cm^2) in a reasonable timeframe (10 minutes), and subsequently irradiate the infused volume with an external beam of 1064 nm light causing a significant increase in photothermal heating relative to a non-perfused volume.

3.2 Methods

3.2.1 *Ex Vivo* Porcine Urinary Bladders

Ex vivo urinary bladders utilized in this paper (with the exception of the experiments outlined in Section 2.3) were excised from healthy, adult, mixed breed pigs of both sexes purpose-bred for research. The bladders were harvested from freshly sacrificed animals by a veterinarian in the Virginia-Maryland Regional College of Veterinary Medicine. Pigs ranged from approximately 5-10 months of age. The experiments utilized both inflated and non-inflated bladders for determination of SWNH dispersal. Bladder inflation was used to create a consistent curvature of the bladder wall, which was generated through introduction of an 18G syringe needle through the urethra into the bladder's interior and subsequent infusion of 500-750 mL of isotonic phosphate buffered saline solution (PBS). Additionally, the exterior of the bladder was moistened at 5 minute intervals with PBS to prevent drying of the serosa that could impact the fluid dispersal properties of the bladder.

3.2.2 Dispersal of SWNHs Laterally Across the Bladder's Serosa

SWNHs were synthesized by the Center for Nanophase Materials Sciences at Oak Ridge National Laboratories (Oak Ridge, Tennessee) by previously described methods [92]. The SWNHs were prepared and suspended in a 1 mg/mL Pluronic F-127 (Biotium, Inc.), as previously described, at a concentration of 0.05 mg/mL [88, 93, 94]. Other groups have demonstrated that the addition of the Pluronic does not affect the cytotoxicity or heat generation of the solution [90, 95-97]. Previous studies have demonstrated that the attenuation coefficient of 0.05 mg/mL in deionized water at 1064 nm to be approximately 2.6 cm^{-1} [88].

Silica FMDs were fabricated from TSP150375 fused flexible silica capillary tubing (Polymicro Technologies, Phoenix, AZ) with an outer diameter of 363±4 μm, an inner diameter of 150±1 μm, and a polyimide outer coating thickness of 40 μm. This capillary tubing was given a sharp, beveled, microneedle tip (see Figure 11) by manual angle-polishing with a series of aluminum oxide lapping films ranging from 5-0.5 μm grit sizes (ThorLabs, Sterling, VA).

For these experiments, an FMD was affixed within the bore of a 22G stainless steel needle and attached to a syringe containing the SWNH solution by plastic tubing. The FMD was manually inserted with gentle pressure into the serosal layer of an inflated bladder at an angle of approximately 10° from the wall's surface. The FMD was inserted a length of 1-2 cm with a final depth at the microneedle's tip of 1-2 mm. The syringe was mounted in an NE-500 syringe pump (New Era Pump Systems, Inc., Farmingdale, NY), and the flow rate was set to 50 μL/min. Infusions were conducted for 15 minutes for a total infused volume of 750 μL. Images were captured with a Canon EOS Rebel T1i/EOS 500D camera (Canon USA, Lake Success, NY) every 30 seconds beginning simultaneously with the syringe pump activation. The SWNH dispersal was traced and measured using ImageJ (NIH, Bethesda, MD) by two independent observers and averaged. Any area measurements with deviation greater than 10% were re-measured by a third observer and averaged with the previous measurements. Experiments were conducted using two bladders with two infusions each (N=4).

Figure 11: Image of sharp, beveled tip of An FMD. Water is visible inside the hollow bore.

3.2.3 Dispersal of Infused SWNHs throughout the Bladder's Layers

Experiments to determine the dispersal of SWNH solution through the thickness of the bladder wall were performed by infusing SWNHs into both inflated and uninflated healthy, *ex vivo* bladders. The *ex vivo* bladders used in these experiments were harvested from healthy, adult, mixed breed pigs of both sexes approximately 7 months in age from a regional abattoir (Smithfield Foods, Inc., Smithfield, VA).

Uninflated bladders were bisected and pinned open to expose the urothelium. A set of infusions was made within a bisected bladder at the thin-walled tissue near the bladder neck, where an FMD was introduced through the urothelium at an angle of approximately 10° to a superficial depth (< 1 mm). These infusions were conducted at a flow rate of 50 µL/min for 5, 10, and 15 minutes and repeated in a second bladder (N = 2). A second set of infusions was administered within a bisected and pinned bladder at the thicker-walled section near the apex. An FMD was introduced at an identical angle, but to a deeper penetration depth (2-4 mm) near the interface of the mucosa and muscularis propria. Sets of infusions were conducted at 50 and 100 µL/min. The higher flow rate experimental set was conducted to determine if there would be any increase in fluid reflux out of the tissue. Three infusions at each flow rate were administered within two bladders for 5, 10, and 15 minutes (N = 2).

Following the completion of both sets of infusions, the bladder tissue was attached to a styrofoam sheet and immediately submerged in 10% neutral buffered formalin solution for fixation. Following a minimum of 24 hours of fixation, tissues were removed and trimmed for further processing. Tissues were dehydrated in a graded series of aqueous ethanols of increasing ethanol concentration, transitioned to ethanol/xylene, xylene/paraffin, and finally paraffin polymer. These dehydration and embedding procedures were done by a Tissue Tek® VIP® 6 automated tissue processing system (Sakura Finetek USA, Inc., Torrance, CA). Once infiltrated with paraffin polymer, three micron sections were cut, rehydrated, and then stained with hematoxylin-eosin stain, using an automated tissue stainer (Leica Microsystems, Wetzlar, Germany).

Another set of experiments was conducted to determine the SWNH dispersal depth in inflated bladders. An FMD was introduced through the serosa proximal to the bladder apex at an angle of approximately 10° to a depth of 2-4 mm. Infusions were conducted at a flow rate of 50 µL/min for 5, 10, and 15 minutes and repeated in a second bladder (N = 2). Immediately after the set of infusions was completed, the bladder was drained, the infused region excised, and the removed tissue attached to a styrofoam sheet for submersion in 10% neutral buffered formalin solution. Following a minimum of 24 hours of fixation, tissues were removed and cut into thin, cross-sectional strips before being photographed with a Canon EOS Rebel T1i/EOS 500D camera (Canon USA, Lake Success, NY).

3.2.4 Laser Irradiation of Infused SWNHs

Experiments were conducted to test laser heating of infused SWNHs in the bladder wall using a 1064 nm CW diode-pumped fiber laser (IPG Photonics, Oxford, MA). The first experimental set was designed to determine the heating differences produced by laser irradiation of a SWNH perfused area of the bladder wall versus a non-infused control. A collimated laser beam with a 5 mm width was used to irradiate the surface of the inflated bladder's serosal layer. Laser energy was delivered at an irradiance of 0.95 W/cm^2 for 40 seconds. Irradiation of the SWNH perfused tissue was conducted at the center of the visually detectable perfused area. Irradiation of the non-infused tissue was conducted at a similar anatomical location on the bladder wall approximately 1 cm away from the edge of the distinguishable nanoparticle perfused region. During irradiation, temperature distribution across the bladder's surface was recorded by an infrared thermal camera at 60 Hz (Thermovision A40, FLIR Systems, Wilsonville, OR). This experiment was conducted in three bladders (N=3).

To determine whether the SWNHs efficacy as exogenous chromophores was independent of the Gaussian distribution of the laser beam, experiments were performed with a 1.5 cm beam width offset from the SWNH perfused bladder tissue in two bladders (N = 2). The *ex vivo* bladder was inflated and infused with SWNHs as described previously. The 5 mm collimated laser beam was expanded to a 1.5 cm beam width using an achromatic doublet lens (ThorLabs, Sterling, VA). The laser beam spot was offset from the discernibly perfused tissue such that only a portion of the beam's periphery was irradiating that tissue. The laser irradiance was 1.1 W/cm^2, and thermographs were taken over 40 seconds of laser heating.

3.3 Results

3.3.1 Dispersal of SWNHs Across the Serosa

The silica FMDs were sufficiently robust to be inserted into the inflated, *ex vivo* bladder wall's serosa and muscularis numerous times without fracturing the FMD or breaching the bladder wall by over-penetration into the lumen. A representative series of time lapse images are shown in Figure 12 A-D.

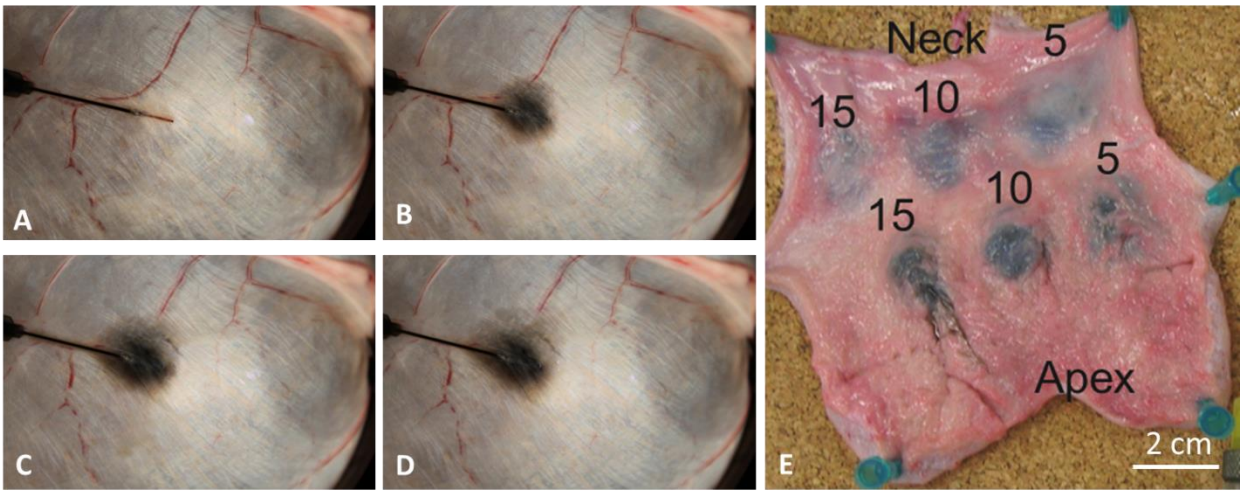

Figure 12: SWNH infusion through FMD into an ex vivo porcine bladder wall. A) t = 0 min, area = 0 B) t = 4 min, area = 1.5 cm2 C) t = 8 min, area = 2.6 cm2 D) t = 12 min, 3.2 cm2 E) Two sets of infusions, located proximal to the neck and apex of the bladder are labeled with their infusion times in minutes. The infusion rate was 50 µL/min for the neck infusions and 100 µL/min for the apical infusions.

SWNH area expansion across the serosa was shown to increase at a relatively linear average rate of 0.36 ± 0.08 cm^2/min when infused at 50 µL/min. A graph of the average values across the 15 min experiments is shown in Figure 13.

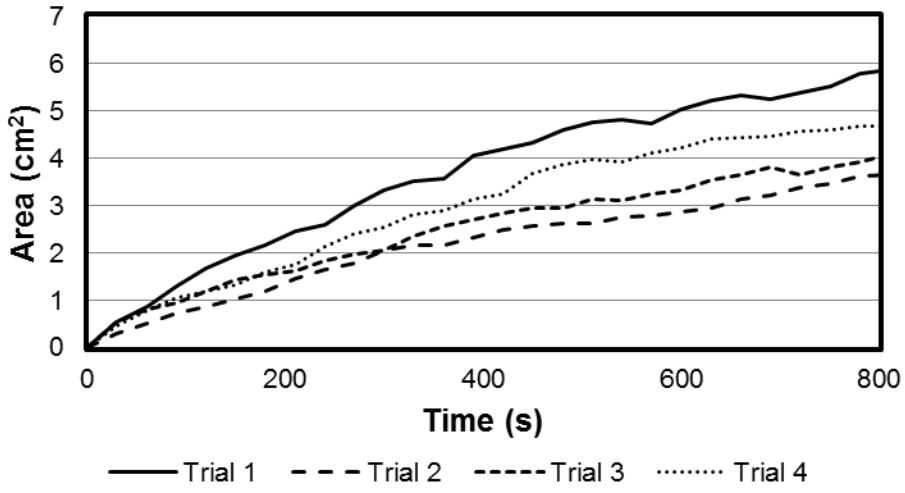

Figure 13: Area of SWNH dispersal versus time plot of data from image analysis of photographs of the serosa taken every 30 s during SWNH infusion at 50 µL/min into the wall of an inflated bladder. Four trials conducted with identical infusion parameters.

3.3.2 Dispersal Depth of Infused SWNHs

FMDs were placed into the urothelium of the bisected bladder repeatedly without sustaining damage. Reflux of fluid escaping the interstitial space by traveling along the FMD's outer surface was dependent on flow rate. Infusions at 50 µL/min produced limited reflux, while infusions at 100 µL/min caused obvious bolus formation and some reflux, which was consistent between infusions. Infusions at 100 µL/min did not demonstrate increased dispersal depth when qualitatively inspected by a trained veterinary pathologist.

A photograph of one set of infusions is shown in Figure 12 E, which demonstrates the pinned bladder and infusion points. Histological sections of infusion regions at the thin-walled neck of

the bladder exhibited SWNH dispersal through the urothelium and muscular propria for the 5 and 10 min infusions, and complete penetration throughout the bladder thickness for the 15 min infusion. Sections in thicker tissue near the bladder's apex showed SWNH dispersal through 4-5 mm of the wall's thickness for all infusion timescales, with more uniform and laterally widespread dispersals for longer infusions. Results were consistent between experiments. The SWNHs were washed from the sectioned tissue during the staining process; however, SWNH dispersal in the stained sections was evident by the expansion of the mucosal layer, which correlated highly with the localization of nanoparticles evident in the gross section from the thicker tissue shown in Figure 14 A-C.

Fixed cross-sections from the infusion sites into inflated bladders unanimously exhibited SWNH penetration throughout the thickness of the wall, independent of infusion timescale. This is possibly attributable to the thinner tissue of the inflated bladders. A representative photograph is shown in Figure 14 D.

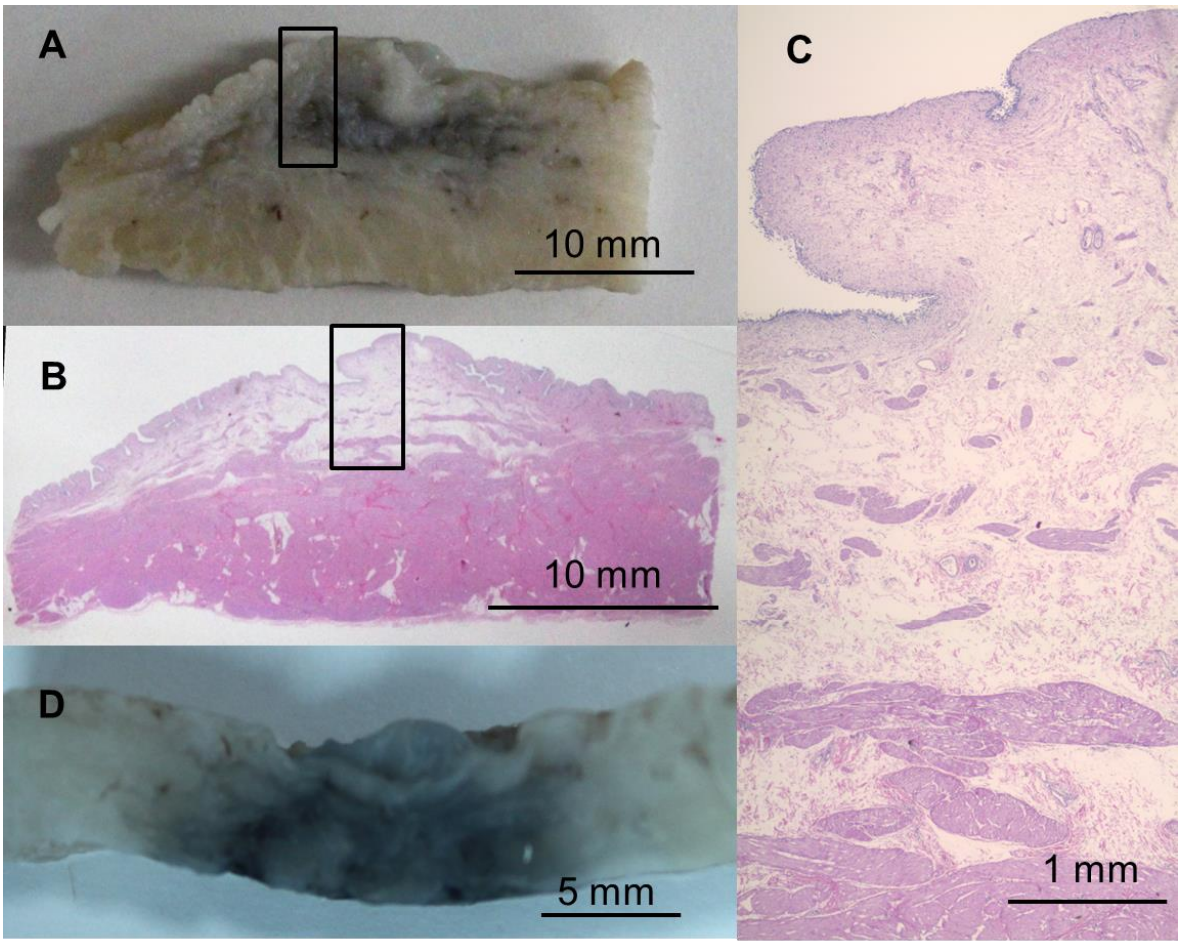

Figure 14: (A) Gross section of formalin-fixed bladder wall following 5 minute infusion into thicker/apical region of uninflated bladder. (B) Histological section cut directly from the gross section (A). (C) Close view of the stained section (location denoted by black boxes in (A) and (B)) showing expansion of the loose connective tissue in the mucosal layer from fluid expansion caused by SWNH infusion. (D) Gross section of fixed bladder wall following 10 minute infusion into inflated bladder showing SWNHs dispersal throughout the wall's thickness. All tissue is oriented with the urothelial layer upwards.

3.3.3 Laser Irradiation of Infused SWNHs

The temperature increase of an inflated, *ex vivo* bladder wall irradiated with 1064 nm laser energy (0.95 W/cm^2 for a 40 s duration) was measured at a region infused with SWNHs after a 15 minute infusion (> 3 cm^2 area) and a region without infusion. Calculation of maximum change in temperature was done by averaging the temperature pixel values over a 1 mm diameter circle centered around the pixel of highest temperature. Laser heating of a non-infused area yielded a maximum temperature increase of 3.2 ± 0.6 °C, while the heating of a SWNH infused area yielded a maximum temperature increase of 19 ± 1.5°C (N = 3). Representative thermographs of these results are shown in Figure 15 A-B.

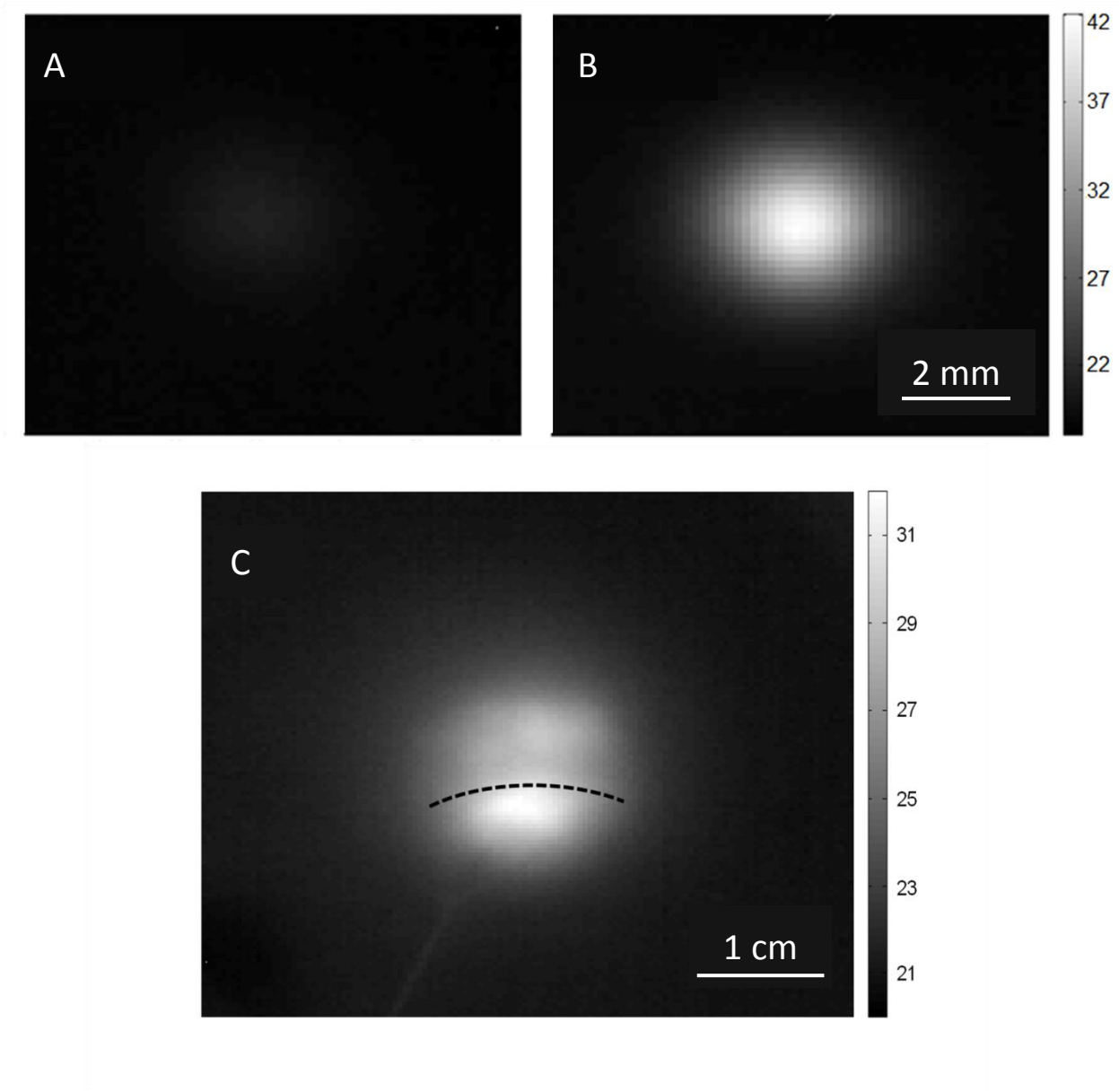

Figure 15: Thermographs of laser heating bladder tissue in regions: A) without SWNHs, B) with SWNHs (A,B have 5 mm beam width) C) Offset from SWNH dispersal (1.5 cm beam width). The highest temperature correlates with the laser/SWNH overlap. The dotted line in C) marks the top edge of the SWNH spread. Intensity scale is in Celsius.

Experiments utilizing an offset laser spot to heat the edge of the SWNH perfused tissue demonstrated that the significant difference in heating caused by the exogenous chromophores

was independent of the Gaussian profile of the laser beam. A representative thermograph of the offset laser spot heating at an irradiance of 1.1 W/cm^2 for 40 seconds is shown in Figure 15 C. A detectable temperature gradient was observed across the laser spot on the tissue correlating with the position of the nanoparticle spot.

3.4 Discussion

The experiments performed in this study demonstrated the ability of small, silica FMDs to quickly deliver a useful volume of SWNHs, which can be subsequently heated with 1064 nm laser energy to hyperthermic temperatures in healthy, *ex vivo* bladders. Experimental results indicated that the SWNHs can be readily delivered into the interstitial space through the FMDs, with significant dispersal across the bladder wall and time-dependent dispersal throughout the wall's thickness. Laser irradiation of the infused SWNHs exhibited significantly increased heating in comparison to non-infused tissue.

A large invasive UCC can be estimated as being 1-2 cm in diameter (assuming a roughly spherical geometry) [38]. This suggests that the largest tumors likely to be treated with this device could be assumed to have an observable surface manifestation on the bladder wall between 1-2 cm^2. If the rate of SWNH area expansion measured in this study would be conserved in the *in vivo* case, FMD infusion of SWNHs should penetrate this large tumor within approximately 5 minutes at a volumetric flow rate of 50 µL/min.

The detectable footprint of infused SWNHs was roughly circular for all the experiments (as shown in Figure 12. The center of this circle was at the mid-length of the FMD's protrusion from

the 22 gauge syringe needle, as opposed to the beveled microneedle tip. Reflux along the shaft of an infusion needle is typically observed in applications such as convection-enhanced delivery (CED) [98]. Krauze *et al*. proposed an improvement in CED infusion cannula designs through inclusion of a step change increase in needle diameter some distance from the cannula's tip, which was shown to halt the progression of reflux [57]. That concept is mimicked in the FMD design for bladder tissue, and a similar effect of the reflux stopping at the 22 gauge needle was observed. Once the fluid pocket of reflux around the FMD portion of the design stabilized, the fluid perfused into the surrounding bladder tissue, resulting in the roughly circular footprint with its centroid at approximately the mid-length of the silica shaft protruding from the stainless steel needle.

Laser irradiation of SWNH perfused tissue with a free space laser exhibited the efficacy of the nanoparticles as exogenous chromophores within the bladder wall. The maximum heating difference (averaged over 1 mm) between irradiating perfused and non-perfused tissue was approximately 590%. For many hyperthermic therapies, the heating threshold for quickly causing protein denaturation and tissue coagulation has been shown to be 60°C [32, 99]. The maximum tissue temperature increase in the SWNH-perfused tissue was approximately 19 °C, a increase in temperature that would fall short of 60°C if conserved in an *in vivo* treatment. However, heating levels can be modulated by varying either the laser irradiance or the concentration of the SWNHs [88, 93]. These findings indicate that SWNHs can aid laser heating of tissue in reaching temperatures inducing rapid hyperthermic tissue damage.

The offset laser spot experiment verified that the increase in heating due to SWNH absorption correlated with the infused region of SWNHs more than the center of the Gaussian beam distribution. This implies that by utilizing the FMD's ability to penetrate the bladder wall, SWNHs can be delivered throughout a target volume to shape the zone of photothermal heating from within deeper bladder layers containing neoplastic tissue. This experiment provides evidence that if the SWNH distribution can be contained within a target volume, laser irradiation should cause selective tissue destruction while preserving healthy tissue. Additionally, the centroid of the heated spot was less than the maximum temperature (both averaged over 1 mm^2) by ~3°C for N = 3 trials, indicating that laser heating of the SWNH permeated tissue needs to be with the center of the beam waist to best leverage the SWNHs.

The authors recognize the potential for FMDs delivering both the SWNHs and laser energy. Delivering SWNHs and laser irradiation through the same delivery channel would allow greater accuracy and control of the photothermal dose; however, the light delivery capabilities of the FMD were being further developed and are therefore not described in this chapter. For treatment of invasive UCCs, one or more FMDs may be guided into the bladder via the working channel of a cystoscope and placed against a tumor located in the bladder urothelium. Mechanical actuation will cause the FMDs to slide through the channel and penetrate the bladder to a final placement at desirable target positions within an invasive UCC. Delivery of exogenous chromophores to specific tissue regions will allow for a localized, targeted treatment and preservation of surrounding healthy tissues. Laser energy emitted from the FMD tip would induce photothermal damage confined by the spread of the SWNHs. This treatment protocol should enable

significantly reduced unwanted collateral healthy tissue damage while maximizing energy delivery to tumor tissue.

The authors acknowledge several limitations in the current study which constrain the context of our conclusions. First, all experiments were performed on *ex vivo* tissue, which is not perfused by blood. Blood perfusion may have a significant effect on the dispersion properties of the nanoparticles during infusion. Additionally, blood perfusion will likely affect the thermal convection and thermal localization properties during laser irradiation *in vivo*. A second limitation is the use of healthy bladder tissue for experimentation. The mechanics of injection, dispersion, absorption, and thermal response within invasive carcinomas may be very different from normal bladder tissue. These differences will be examined in future studies.

The FMD can potentially deliver a variety of fluid agents or pharmaceuticals in addition to the specific parameters used in this study. Other wavelengths within the near-infrared region associated with high tissue penetration could be used in conjunction with the SWNHs, such as 800 μm. The fluid delivery method outlined could be used to deliver other nanoparticles in solution or alternatively be used to deliver adjunctive, local treatments such as chemotherapy or photodynamic therapy. This versatile, enabling technology could be useful for a wide variety of treatment options in addition to the therapeutic concept outlined in the above experiments.

Chapter III Supplement 1: Fiberoptic Microneedle Device Design Concept

3S1.1 Initial Co-Delivery FMD Design

Previous publications have described the FMD's evolving state of development, which has progressed to a prototype incorporating a light-guiding capillary tube (HCF) capable of delivering both fluids and light [100-102]. A concept depiction of this design is shown in Figure 16. The HCF is commercially available light-guiding silica capillary tubing (365 µm outer diameter, 150 µm inner diameter, Polymicro Technologies, Phoenix, AZ) angle-polished at the tip to produce a sharp, beveled microneedle, shown in Figure 11. Light conduction is achieved by the principle of total internal reflection within the fused silica annular core (291 µm OD, n = 1.46) by having an exterior cladding layer of doped silica (15 µm OD, n= 1.44) and a fluid medium with a lower refractive index inside the inner bore [103].

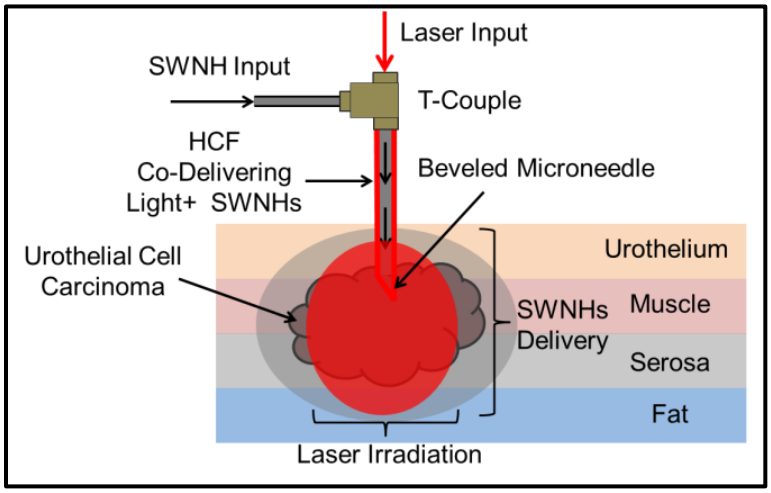

Figure 16: FMD design concept for bladder treatment. Light-guiding HCFs permit simultaneous co-delivery of laser light and fluid agents, enabling a combinatorial treatment.

To fabricate a prototype capable of co-delivery, the HCF was coupled with both a multimode fiberoptic (50/80 µm core/clad, Polymicro Technologies, Phoenix, AZ) and a 30 gauge syringe needle (Becton, Dickinson, Franklin Lakes, NJ) inside a 410 µm inner bore sheath made from a 22 gauge dispensing needle (McMaster-Carr, Atlanta, GA). A schematic of this co-delivery couple is shown in Figure 17. Light from a 1064 nm laser was coupled into the 80 µm fiber using a free space to fiberoptic coupler (Newport Corporation, Irvine, CA). The distal end of the fiber was placed inside a 22 gauge sheath (approximately 1 cm long) simultaneously with a 30 gauge syringe needle. Once the fiber and 30 gauge needle were positioned, epoxy (Master Bond Inc., Hackensack, NJ) was applied to the end of the sheath to hold them in place. The HCF was aligned relative to the 80 µm fiber with a 3D goniometer micropositioning stage (Opto Sigma, Santa Ana, CA). Coupling efficiency was determined by placing the distal end of the hollow-core fiber into an integrating sphere (Newport Corporation, Irvine, CA). Once a coupling efficiency of >30% was attained, the HCF was also epoxied into the sheath. Both ends of the sheath were epoxied a second time to ensure a robust fluid seal.

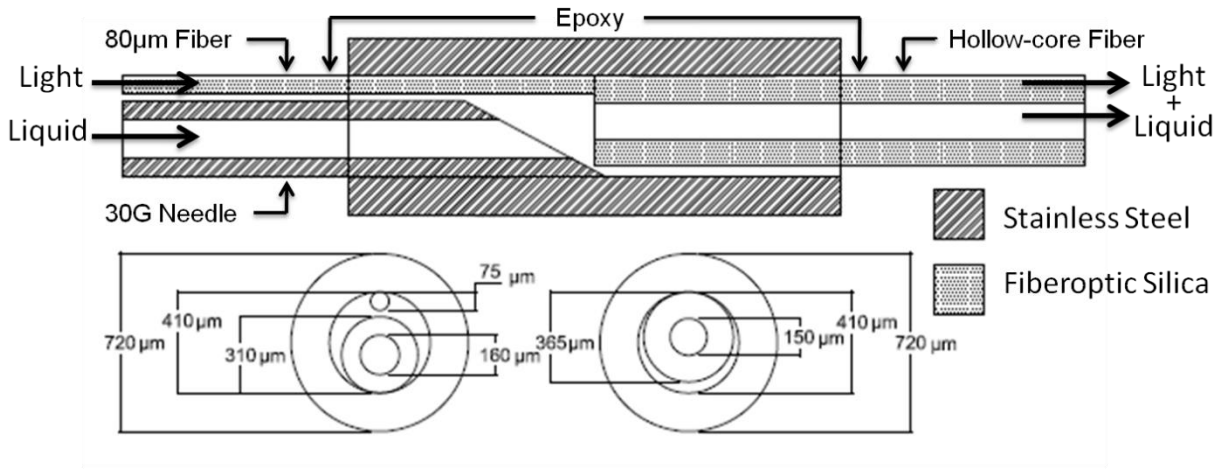

Figure 17: Schematic of first FMD co-delivery couple design.

3S1.2 Demonstration of Co-Delivery with a Fiberoptic Microneedle Device

Experiments demonstrating co-delivery through a single light-guiding capillary tube were performed through sequential delivery of SWNH solution and laser light into healthy, *ex vivo* bladders. Light from a 1064 nm laser was coupled into an 80 μm fiber using a free space to fiberoptic coupler. A 30 gauge needle fluid input was attached to a syringe filled with a 0.05 mg/mL SWNH solution. Pressurized flow was provided by an NE-500 syringe pump. The distal end of the co-delivery HCF was introduced into the wall of an inflated, *ex vivo* bladder (as described previously). HCFs were manually inserted at an angle of approximately 10° through the serosa of the inflated bladder. Insertion depths varied between 1-2 mm and the inserted length between 1-2 cm. Infusion was conducted at 20 μL/min for 25 min, and the expanding nanoparticle perfused area was captured every 1 min with an SLR camera. After infusion was complete, the sample was irradiated with 1064 nm laser light conducted through a HCF at 400 W/cm^2 for 40 seconds. A control experiment heating a non-infused bladder wall with the same power was also performed. Thermographs of the irradiated tissue were captured via IR thermography as described previously.

The co-delivery couple prototype had a light coupling efficiency of 35% between an 80 μm multimode fiber and the HCF. Experiments demonstrating the feasibility of co-delivery through a single HCF exhibited a maximum temperature increase of 33° C when irradiated at 400 W/cm^2 for 40 seconds. Temperature increase for non-perfused tissue at the same irradiance and time was 5° C. Representative images of the light delivery to both infused and non-infused regions of the bladder wall are shown in Figure 18.

Figure 18: Irradiation from light-guiding, hollow-core microneedle after delivering SWNHs into the inflated bladder wall. Left) photograph showing microneedle position (Note: the red guide laser is visible), Middle) thermograph of non-infused control, Right) thermograph of SWNH perfused tissue. Color scale is in Celsius, white lines denote fiber path.

3S1.3 Discussion

The experiments utilizing the HCF for both the fluid and light delivery demonstrated proof of concept for the FMD. Successful infusion of SWNH solution followed by 1064 nm laser light irradiation heated tissue to a maximum temperature shift of 33° C within 40 seconds of heating the tissue at 400 W/cm^2. Optimization of treatment parameters and approach were not an objective of this pilot study, as the *in vivo* case may differ significantly from the tissue utilized. Although the volume treatable by a single cycle of co-delivery may prove insufficient for photocoagulation of a target tumor's margins, multiple heating cycles, insertions, or fibers in parallel could be utilized to increase the treated volume and efficacy of treatment. These results substantiate the feasibility of photothermal treatment at invasive tumor depths with the FMD.

Chapter III Supplement 2: Initial Cystoscopic Deployment of the Fiberoptic Microneedle Device

3S2.1 Cystoscopic Deployment Method

Two FMDs were prepared through the methods described above. An epoxy collar was formed approximately 0.5 cm from the tip to reduce reflux. One FMD had a sharp, angle-polished tip (approximately 45º). The second was flat-polished. A clinical cystoscope with a 25^{o} Wolfe telescope, a 13 Fr sheath, and an angled instrument insertion port was introduced through the urethra and into the bladders of female, canine cadavers. The FMDs were inserted through the insertion port and instrument channel into the tissue's submucousa. Infusions of trypan blue were made into both the bladder and urethral walls. Infusions were made at 0.3 mL/min and continued for 2 min.

3S2.2 Results

Both FMDs were inserted smoothly through the angled instrument channel without damage. Transmucousal insertion with the angle-polished FMD required far less force and a lower insertion angle (defined above) while creating a smaller mucosal defect. Substantial reflux was observed if the epoxy collar was not pushed flush against the tissue wall. Dye spread throughout the muscular layer and may have permeated the submucousa. Infusion areas of approximately 1-2 cm^2, an area consistent with that presented by many veterinary canine patients, were estimated by an expert in veterinary urology. Photographs of infused bladders are shown in Figures 19 and 20.

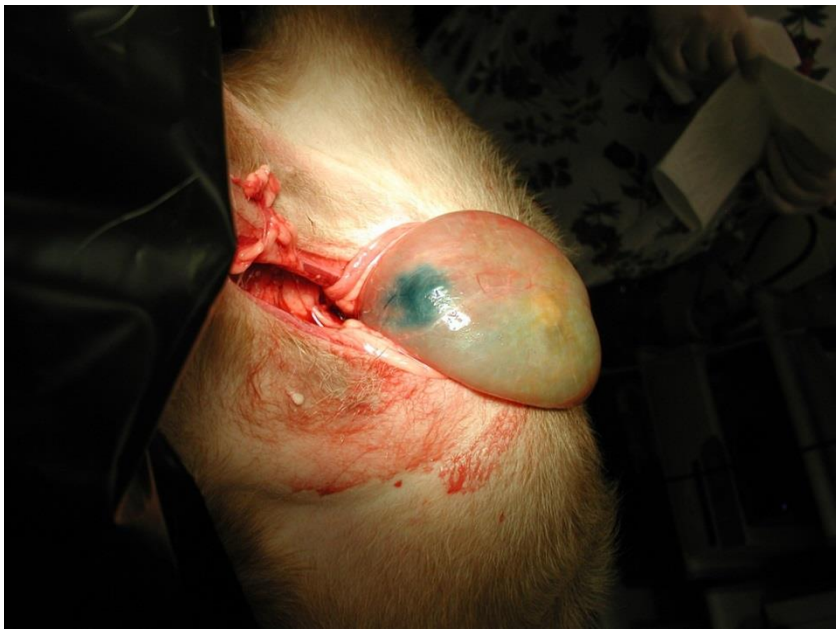

Figure 19: Infused and filled bladder protruding from cadaver's body. A single, large infusion site can be seen.

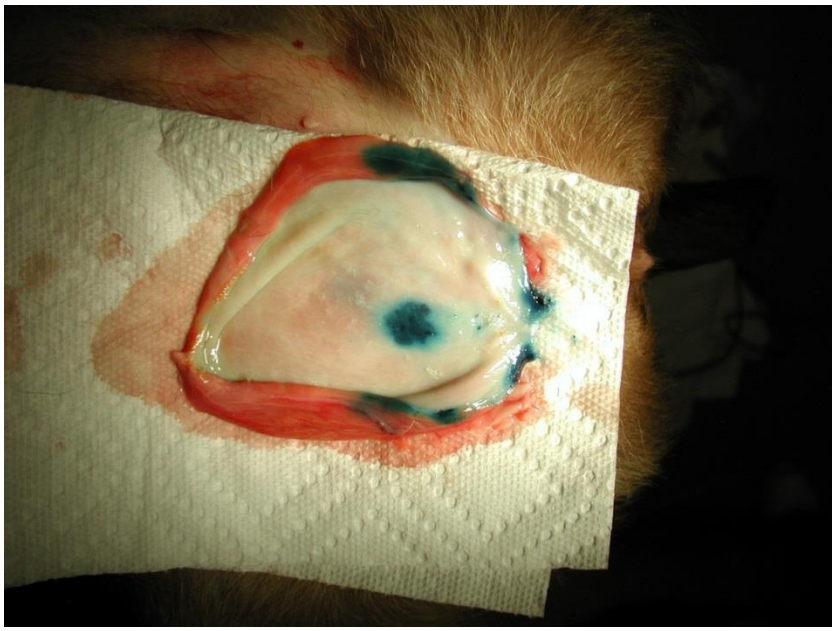

Figure 20: Photograph of the mucousal side of an excised and opened bladder. The bladder neck is to the right and the apex is to the left. Multiple infusion sites are visible.

3S2.3 Discussion

The FMD devices were successfully inserted through the instrument channel of a clinical cystoscope and used to repeatedly infuse clinically relevant areas of dye into target regions. Addition of an epoxy collar was observed to be an improvement over previous designs. Angle-polishing of the FMD tip lessened the difficulty of transmucousal insertion and was perceived to generate less of a tissue defect. This served as the first successful deployment of FMDs through a urethral cysctoscope.

Some interesting observations were made by the administering clinician. Dye was noticed to infiltrate and spread through blood vessels, as shown in Figure 21. If infusing SWNHs as specified above, the potential for systemic spread of the particles may present a regulatory challenge. Additionally, dye spread was not limited to the target detrusor muscle layer, but seemed to also infiltrate the submucousa. *In vivo* characterization of the pharmacokinetics demonstrated by SWNHs infused into the bladder will most likely be a necessity.

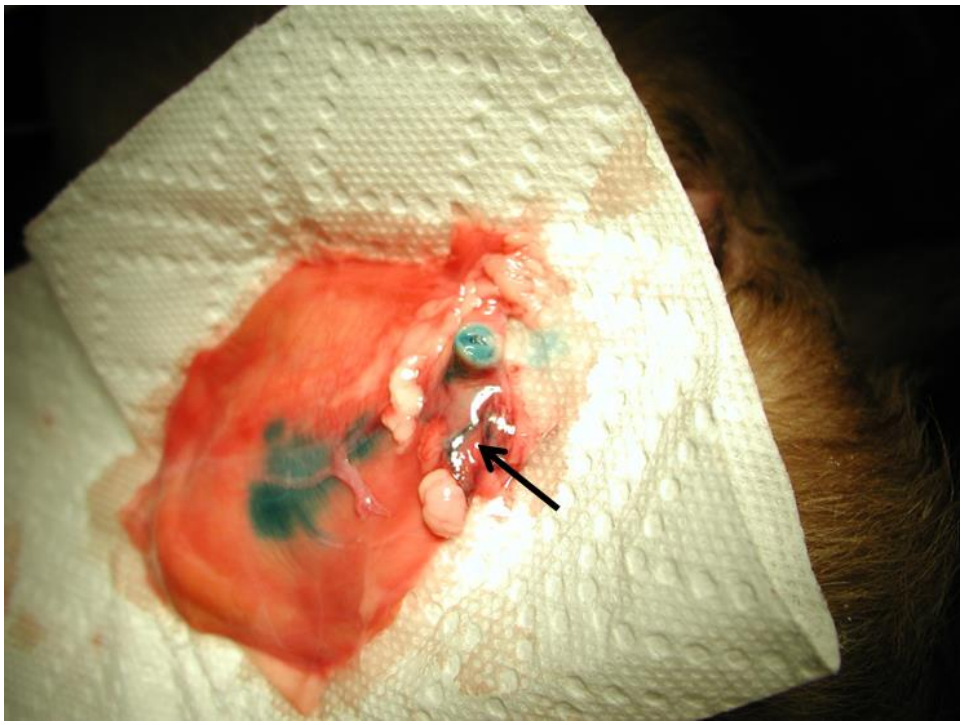

Figure 21: Arrow indicates where infused dye infiltrated a local blood vessel.

Chapter IV: Thermally Augmented Convection-Enhanced Drug Delivery Using the Fiberoptic Microneedle Device

4.0 Abstract

This chapter marks a transition in focus from the previous chapters, in that the remaining sections of this document detail work developing the FMD for conducting convection-enhanced delivery (CED). This section describes a new iteration of the FMD designed with the objective of photothermally augmenting the volumetric dispersal of infused therapeutics. We hypothesize that concurrent delivery of laser energy, causing mild localized photothermal heating (4-5 °C), will increase the spatial dispersal of infused chemotherapy over a long infusion period. Agarose brain phantoms, which mimic the brain's mechanical and fluid conduction properties, were constructed from 0.6 wt% Agarose in aqueous solution. FMDs were fabricated by adhering a multimode fiberoptic to a silica capillary tube, such that their flat-polished tips co-terminated. Continuous-wave 1064 nm light was delivered simultaneously with FD&C Blue #2 (5%) dye into phantoms. Preliminary experiments, where co-delivery was tested against fluid delivery alone (through symmetrical infusions into *in vivo* rodent models), were also conducted. In the Agarose phantoms, volumetric dispersal was demonstrated to increase by more than 3-fold over a four-hour infusion time frame for co-delivery relative to infusion-only controls. Both forward and backward (reflux) infusions were also observed to increase slightly. Increased volumetric dispersal was demonstrated with co-delivery in an *in vivo* rodent model. Photothermal augmentation of infusion was demonstrated to influence the directionality and increase the volume of dye dispersal in Agarose brain phantoms. With further development, FMDs may enable a greater distribution of chemotherapeutic agents during CED therapy of brain tumors.

4.1 Background and Objectives

Convection-enhanced delivery (CED) is a technique for delivering large molecules directly into the brain parenchyma, bypassing impediments imposed by the blood-brain barrier [46, 47]. CED is accomplished via placement of catheters, through a burrhole in the skull to positions within and around a target tumor. This technique has been investigated for treating neurodegenerative, epileptiform, and neoplastic diseases [47-51]. In CED, chemotherapeutic infusate is actively pumped (flow rates range from 1-10 μL/min) into the brain parenchyma and pushed through the interstitial space[104]. Infusion may be continued for several days. In contrast to millimeter distances obtained with simple diffusion, CED has been shown in laboratory experiments to deliver high-molecular-weight proteins up to 2 cm into the brain parenchyma, after as little as 2 hours of continuous infusion [104]. This was accomplished without causing cerebral edema and was unaffected by capillary loss or metabolic conversion of the macromolecule[20]. Subsequent studies demonstrated that CED was a viable method for providing regional distribution of molecules as large as immunotoxins and radioisotope–conjugated antibodies, and even some conventional chemotherapeutic agents [23, 67-71].

Although CED-based therapies seemed promising from laboratory studies, the method failed to meet required clinical endpoints in a recent Phase III FDA trial wherein CED was used to deliver an immunotoxin to treat malignant gliomas [23]. This was attributed to the CED method insufficiently distributing chemotherapy throughout the target tumors and failing to broadly disseminate drug to the infiltrative tumor cells in the tumor periphery [23]. While shortcomings in a clinical trial might be remedied through better implementation, the sizable biological

challenges presented by intracranial neoplasms may better lend themselves to engineering solutions.

Clinical and laboratory studies have shown that efficacy of thermochemotherapy, or heating of delivered chemotherapeutic agents, for increasing fluid penetration into peritoneal tumors[59]. This is intuitive, as both convective and diffusive fluid transport increase with increasing temperature. In addition, the cytotoxic effects of several chemotherapeutic drugs can be enhanced by adjunctive hyperthermia[60-62]. The augmented cytotoxicity has been attributed to several biological mechanisms, including plasma membrane permeabilization and amplified cell metabolism. Adjunctive hyperthermia could also increase volumetric dispersal and efficacy of chemotherapeutics delivered through CED.

Motivated by the limitations of current CED methods, we have invented a fiberoptic microneedle device (FMD) capable of co-delivering fluid agents and laser energy. This is achieved through simultaneous delivery of laser energy during an infusion, allowing for volumetric heating throughout the infusion zone. For this application, the FMD consists of a silica capillary tube (365 μm OD; 150 μm ID) and a solid-core (100/110 μm core/cladding) fiber in parallel. We have previously published microneedle fabrication techniques and results of mechanical penetration into tissue for similar designs[76, 105], and have demonstrated the properties of these microneedles as pertaining to both light and fluid delivery[106, 107].

The objective of this study was to determine if co-delivery of laser light during infusion would increase fluid dispersal in a well-studied prototypic tissue model. Our hypothesis was that by co-

delivering laser energy during fluid infusion sufficient to heat the Agarose 3-4 ºC, fluid dispersal volume and uniformity could be significantly increased over an infusion time frame of 4 hours.

4.2 Materials and Methods

4.2.1 Two Fiber Co-Delivery FMD Manufacture

Two fiber co-delivery FMDs were fabricated by bonding a fused silica capillary tube (365 µm outer diameter, 150 µm inner diameter, Polymicro Technologies, Phoenix, AZ) and a multimode fiberoptic (100/110/125 µm core/cladding/jacket, Polymicro Technologies, Phoenix, AZ) in parallel. The capillary tube was epoxied into a stainless steel 22G dispensing needle (McMaster-Carr Supply Company, Elmhurst, IL) such that the fiber extended ~25 cm from the dispensing needle tip. The extended length was threaded through an 18G stainless steel dispensing needle in parallel with a length of multimode fiber. The two fibers were epoxied in parallel such that their end-faces co-terminated. Both ends of the 18G dispensing needle were epoxied to provide lateral stability to the device. A schematic and photograph of the co-delivery FMD are shown in Figure 22.

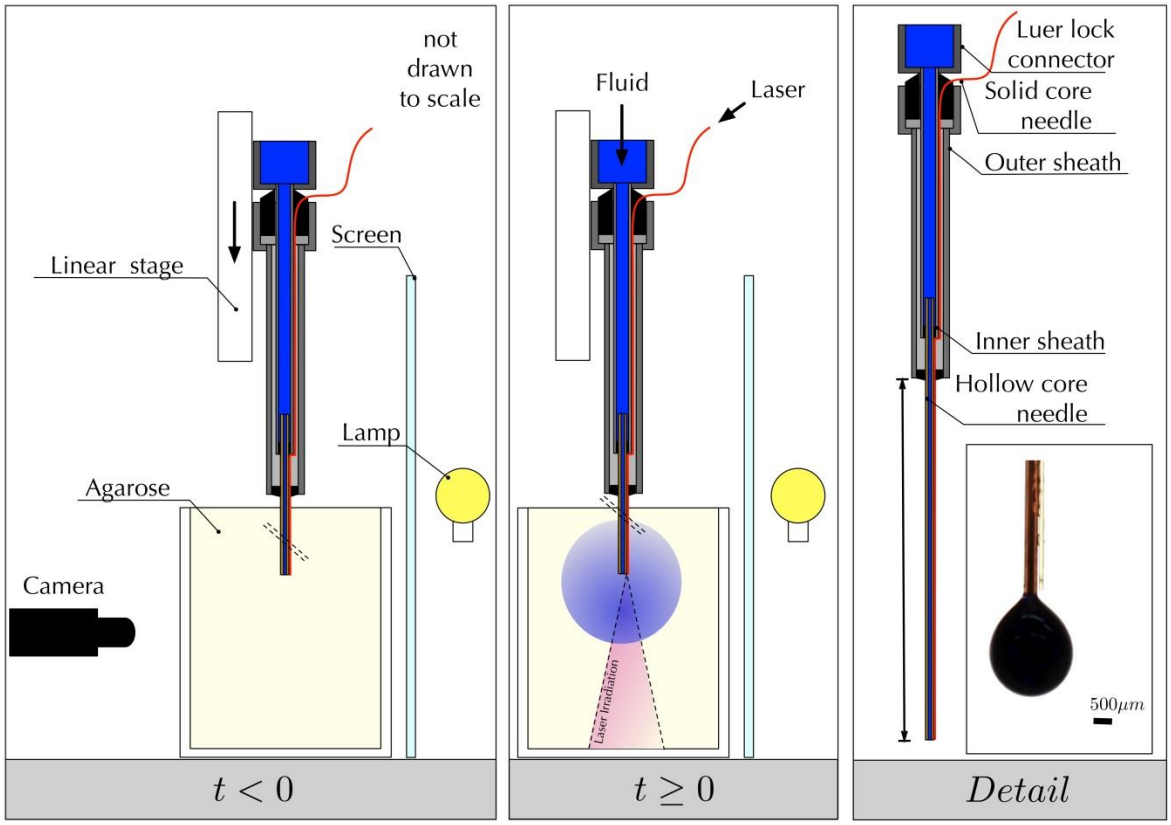

Figure 22: Depiction of experimental setup and procedure.

4.2.2 Agarose Brain Phantom Experiments

Certified molecular biology grade Agarose (#161-3101, Bio-Rad Laboratories, Hercules, CA) was mixed to create a 0.6% suspension (w/w) with de-ionized water. This mixture was then heated to boiling, allowed to cool for 15 minutes, and then decanted into rectangular, polystyrene molds (1.7x8.1x3.9 cm). The molds were tightly covered using Parafilm® M Barrier Film (American National Can Company, Norwalk, CT) and refrigerated at ~4 °C for at least 24 hours prior to use. Before experimentation, the phantoms (in molds) were removed from refrigeration for approximately 1 hour to allow a return to room temperature. This warming time was established as sufficient by measuring the temperature of representative Agarose volumes with a K-type thermocouple and a HH127 Data Logger (Omega, Stanford, CT).

A custom shadowography framework was fabricated from stiff aluminum profiles, a light diffusing acrylic sheet, and a goniometer micropositioning stage (Opto Sigma, Santa Ana, CA). The framework enabled backlit visualization of the infused volume and vertical, guided insertion of the FMD into the Agarose volumes.

Agarose infusions were conducted with fluid infusion at 1 µL/min and simultaneous irradiation with a 1064 nm CW diode-pumped fiber laser (IPG Photonics, Oxford, MA) at 0.5 W or at a 0 W (low power guide laser only) control. Laser light was coupled into the multimode fiberoptic light with a freespace to fiberoptic coupler (Newport Corporation, Irvine, CA). Prior to insertion and immediately following infusion, the FMD's transmission power was determined by placing the distal end into an integrating sphere (Newport Corporation, Irvine, CA). The capillary tube was primed with 5% FD&C Blue #2 dye. Pressurized flow through the FMD was provided by a 10 mL syringe (Becton, Dickinson, Franklin Lakes, NJ) connected to an NE-500 syringe pump (New Era Pump Systems, Inc., Farmingdale, NY).

The FMD was advanced into the Agarose block by manually loosening a set screw on the experimental framework and sliding the guided post vertically. Casanova *et al.* demonstrated that fluid reflux (backflow along the catheter body) in Agarose could be reduced through rapid catheter insertion[108]. Once manually inserted to a depth of 1-1.5 cm from the Agarose surface, the FMD was carefully translated to the depth of 1.5 cm with the goniometer. Once the target depth was reached, the FMD was raised 0.1 cm with the goniometer to reduce clogging at the microneedle tip, as described by Martanto *et al* [58]. If the manual insertion overshot the 1.5 cm target, the FMD was removed and reinserted elsewhere in the Agarose volume.

After successful insertion, the syringe pump and laser were begun simultaneously and continued for four hours. Laser irradiation was conducted at 0 (control) or 500 mW. Photographs were captured once every minute by a Canon EOS Rebel T1i/EOS 500D camera (Canon USA, Lake Success, NY). Line pressure at the 10 mL syringe was recorded using an OPP-M fiberoptic pressure sensor (OpSens Inc., Quebec, Quebec). If the pressure reached 40 mmHg, the system was considered "clogged" and the FMD was raised and lowered 1 mm with the goniometer. If the pressure reached 60 mmHg, the infusion ceased and the data was discarded. The experiment was also considered void if substantial reflux reached the surface of the Agarose. The laser power of 500 mW was determined to heat the Agarose volume to a steady state increase in temperature of 3-4 °C in a preliminary experiment.

4.2.3 Data Processing

The recorded images were processed using MatLab to estimate infusion volume with the assumption of rotational symmetry. The outer diameter (1.5mm) of the metal syringe needle was used to determine pixel size for each data set to ensure consistency. The location of this needle was also used to obtain the central axis for rotational integration as well as to correct for injection angles. The first image of each series was subtracted from subsequent images. The images were transformed into a set of binary data points through thresholds. The image was then bisected at the centerline and averaged into a single shape. This step accounted for non-symmetric fluid distributions. The averaged data sets were then rotationally integrated to obtain a volumetric dispersal value.

In order to determine estimator uncertainties, a set of reference images mimicking the infusion experiment were created. These sets were used as a benchmark for the data processing. While image artifacts are compensated for by the base picture, fluctuations in environmental light intensity and needle angle misalignments were carefully avoided. Figure 23 shows a representative set of simulated data; it is here assumed that the fluid is distributed in the porous media in a spherical fashion, which is an idealization of the ovoid profiles typical of the data. The volumes of the needles are accounted for by initial image subtraction. For the experiments described later, the volume coverage of the needle in the target volume was considered negligible and correction was not performed.

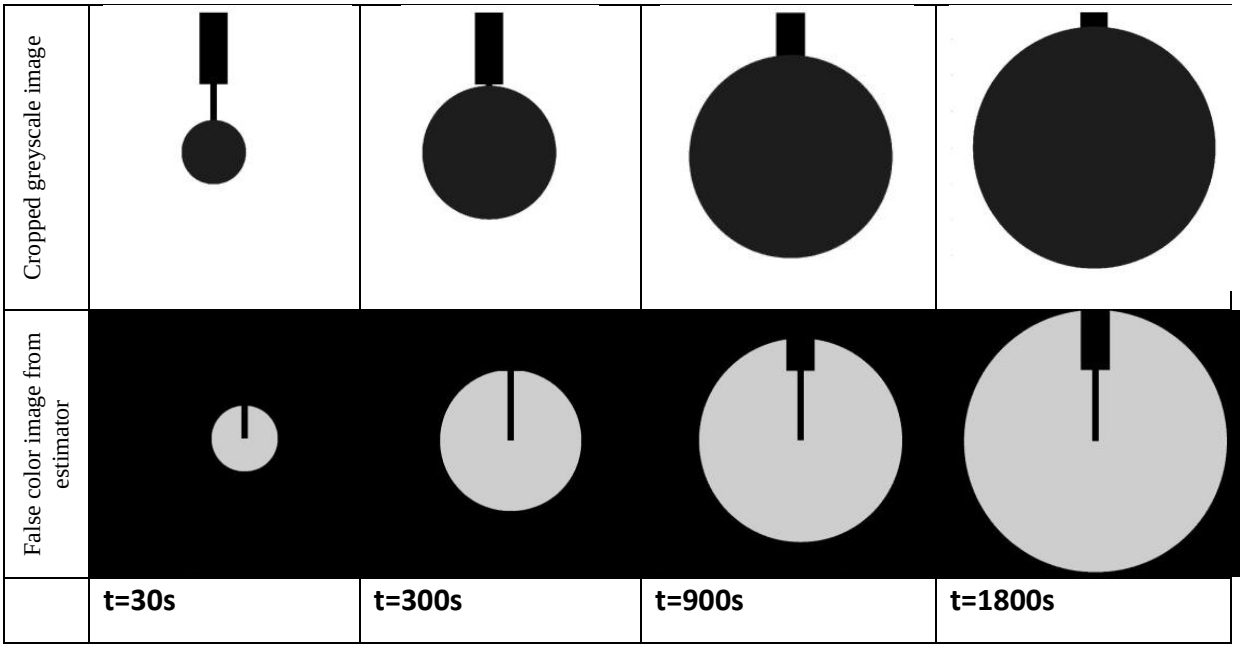

Figure 23: Simulated data to determine error at different timepoints generated from shadowography approach. These images are associated with an assumed DPI of 300.

For image sets with a data density of 150 DPI only, a 10 % uncertainty can be reached. However, data sets with 300 DPI and above, uncertainties as low as 1-2 % can be achieved. Experimental photography was conducted with a data density of at least 300 DPI to minimize error. Figure 24

demonstrates the dependency of the data reduction on the information density of the estimation process.

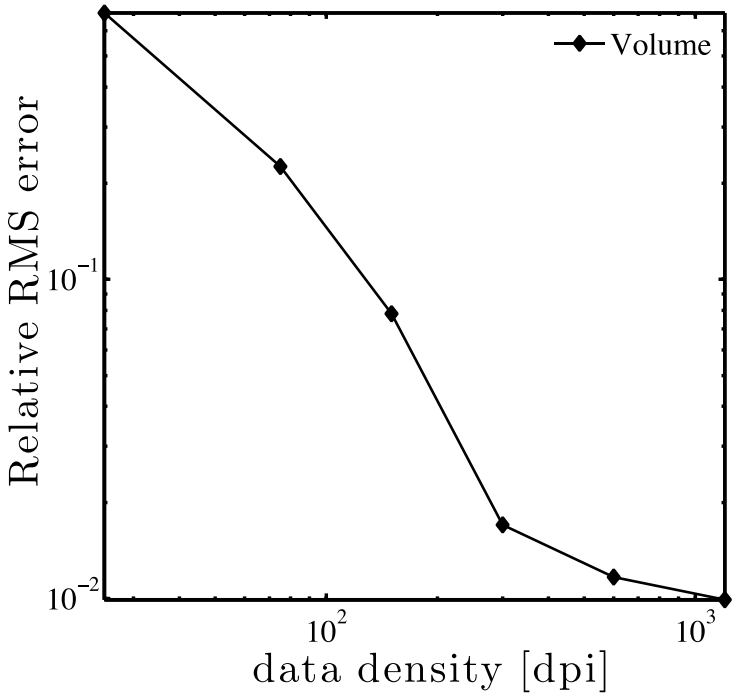

Figure 24: Volume distribution uncertainty dependent on spatial density of data set.

4.2.4 Preliminary Study with *in vivo* Rodent Brain

A similar pilot study was conducted using an *in vivo* rodent model to further test the technique of photothermal augmentation of intracranial infusions. Experimental protocols were approved by an Institutional Animal Care and Use Committee (CVM-12-057) and were performed in a GLP compliant facility. Two male Fischer 344 rats weighing 220–250 g were administered buprenorphine (0.02 mg/kg subcutaneously) prior to anesthesia with isofluorane delivered through an induction chamber. Anesthesia was continued using nosecone-delivered isofluorane. Confirmation of surgical plane of anesthesia was made by interrogation of the loss in tail or toe pinch reflex. The hair local to the surgical site was clipped and prepared aseptically, through

application of solutions containing povidone-iodine and alcohol. Once anesthetized, rats were secured with a stereotactic head frame designed for small mammals (Model 1350M, David Kopf Instruments, Tungisten, CA). The surgeon made a rostrotentorial surgical approach to the skull and created symmetrical circular parieto-occipital burr-hole craniectomy defects in both the left and right aspect of the skull using a highspeed electric drill.

Co-delivery infusion/irradiation was conducted with 1064 nm laser light at 100 mW and 2% Evans Blue (EB) solution infused into the parieto-occipital cerebral cortices. The laser power was determined to heat the brain tissue 3-4 °C in a set of experiments described in previous work by this group[105]. The set infusion flow rate was 0.1 µL/min and the experiments were conducted for 1 hour. For the N=2 rats utilized in these experiments, infusions were conducted symmetrically and simultaneously in either hemisphere of the brain. The FMD design employed was of a modified, single-fiber co-delivery design described in previous work[105]. Co-delivery through an FMD was conducted in the right hemisphere while fluid delivery alone through an identical FMD on the left. The FMDs were inserted using the stereotactic head frame to a distance of 0.75 mm within the cerebral tissue. Laser energy and fluid infusion were initiated simultaneously at t = 0.

When the infusion were completed, the FMDs were withdrawn and the rats euthanatized through injection of 1 mL of phenytoin-pentobarbital solution (Beuthanasia-D [390 mg phentobarbital sodium and 50 mg phenytoin per mL], Intervet Laboratories, Summit, NJ) prior to cervical dislocation. The brains were carefully removed *en bloc*, embedded in optimal temperature

cutting media, flash frozen in liquid nitrogen, and serially sectioned at 40 μm intervals in a cryotome to allow inspection of the infusate dispersal.

4.3 Results

4.3.1 MatLab Analysis of the Agarose Infusions

Using the MatLab thresholding software, volumetric dispersal of the infused fluid was calculated for the experimental and control groups at one minute timepoints. Each experiment was conducted at N=5. Plots of the volume measurements are shown in Figure 25 below.

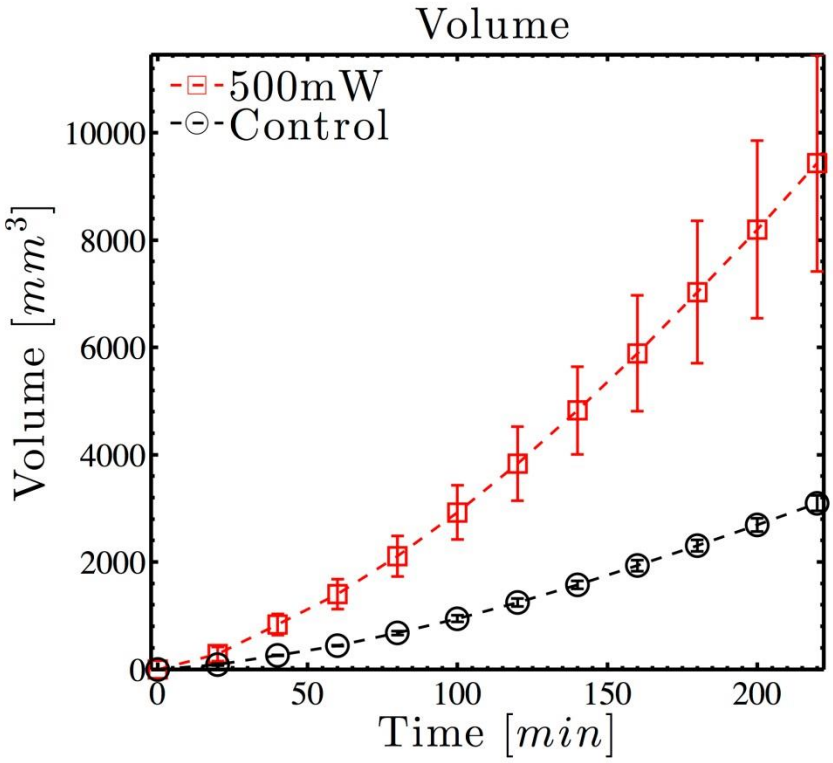

Figure 25: Volumetric dispersal for each infusion group over 4 hours.

In addition to volumetric dispersal, other metrics of comparison were calculated. Two such metrics were chosen to best show contrast between the different experimental and control groups

were center of gravity and forward dispersal of the fluid. For these plots, the origin is at the tip of the FMD and the positive axis is back along the length of the needle. The center of gravity is defined here as the centroid of the 2D shape delineated by the spreading dye. Figure 26 depicts plots of each group's measured center of gravity over the 4 hour infusion period. The forward dispersal is defined as the distance of the 2D centroid to the furthest threshold below the FMD tip. Figure 27 shows the calculated forward dispersals for each infusion group.

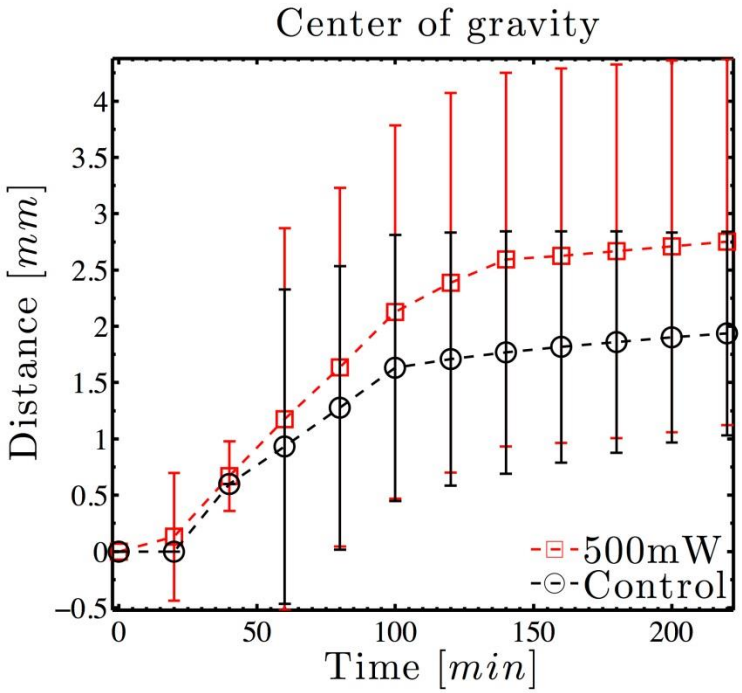

Figure 26: MatLab calculated values for the dispersing dye's center of gravity.

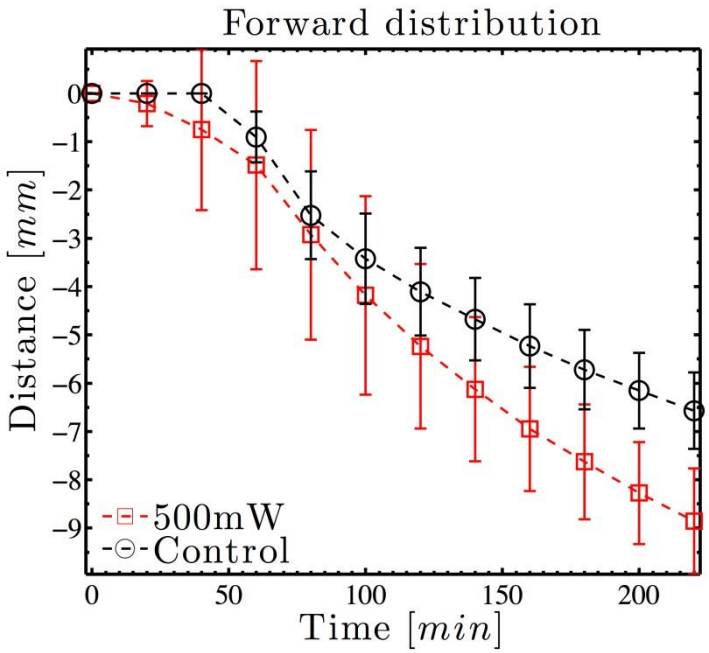

Figure 27: MatLab calculated values for the dispersing dye's distribution forward of the FMD tip.

4.3.2 Delivery into *in vivo* Rodent Brain

Inspection of brain cross sections from the *in vivo* rodent experiments showed a substantial increase in fluid dispersal for the co-delivery infusion compared to the fluid-only control. Damage observed in the brain tissue as a result of the infusion was limited to microhemorrhage along the FMD insertion tracks and a focal area of coagulative necrosis within the cerebral cortex at the FMD tips. For these pilot experiments, very little infusate reflux observed, although this was to be expected due to the low flow rate (0.1 µL/min). A representative section is shown below in Figure 28.

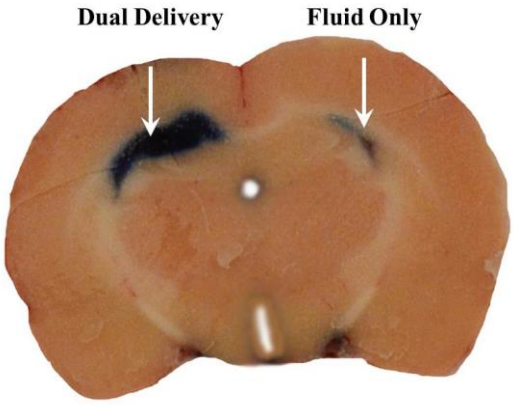

Figure 28: Gross section from in vivo rodent co-delivery experiments. Arrows denote estimated insertion vectors and approximate FMD tip position.

4.4 Discussion

Analysis of the forward distribution in the path of the laser energy offered proof for the hypothesized photothermally-mediated dispersal increase. The infusion volume demonstrated a geometric bias along the forward cone of the laser energy, but also increased orthogonally to the FMD's length. These observations correlate well with the expectation of enhancing the dispersal through photothermal means, as heat generation was greater in the path of the laser, but thermal conduction through the Agarose also increased dispersal rate outside of that path. Analysis also exhibited a positive correlation between reflux and laser energy delivered. This finding can be attributed to several mechanisms. Fluid viscosity shares an inverse relationship with temperature, and the reflux model described by Morrison *et al.* states that reflux distance increases with decreased viscosity[109]. Another reason could be that as reflux happens to some degree almost invariably, that heated fluid going up the FMD body is in turn heating the Agarose it contacts through thermal conduction, in addition to the heat generation from the laser in the Agarose volume. As the hypothesis of enhanced dispersal through slight photothermal heating is

supported by these findings, the described heating of backflow dye would enhance dispersal along the entire catheter body.

The pilot study in the *in vivo* rodent model provided data to support the hypothesis of photothermally-enhanced fluid dispersal. While the limited nature of the study would make quantitative analysis misleading, qualitative comparison showed significant increases in volumetric dispersal. An interesting observation was the limited reflux observed, but that may be attributable to the low flow rate. Another possible explanation for the substantial increase in dispersed volume would be tissue coring into the FMD bore for the control experiments, an alternative theory that cannot be dismissed due to the low N-number of the experiment. As tissue coring from brain tissue is semi-solid, one could speculate that heating from the laser light could lower the viscosity of the clog, making it easier to clear. These results, observations, and theories motivate a comprehensive *in vivo* study to be conducted in the near future.

The authors recognize the limitations of an Agarose model in comparison to the disease state *in vivo*. While the pilot study in the rodent model did support the conclusions from the more comprehensive Agarose study, further experimentation is necessitated to extinguish doubt as to the effect of co-delivering photothermal energy during fluid infusion. Nicholson *et al.* wrote a comprehensive review on the mechanics of drug transport in tissue, from which one can deduce that there are significant differences between different *in vivo* models, implying Agarose models are a further departure. Limitations of the artificial brain phantom model in comparison to *in vivo* brain tissue are shown in Table 3 below.

Table 3: Relative Comparison of used brain models

	Agarose Brain Phantom	***In vivo* Brain Tissue**
Composition	Homogeneous	Heterogeneous
Conductivity	Isotropic	Anisotropic
Visibility	Transparent	Opaque
Perfusion	None	Yes
Interstitial pressure	None	High
Physiological Response	None	Yes

4.5 Conclusion

This study was conducted to determine if co-delivery of laser energy would increase volumetric dispersal of infused dye in an Agarose tissue model. Using shadowography and image processing techniques, this chapter demonstrated that volumetric dispersal of an infusion into Agarose brain phantoms can be enhanced through concurrent photothermal heat generation. A subsequent preliminary study in an *in vivo* rodent model supported the conclusion. In addition, the infused volume exhibited a slight increase in forward penetration into the Agarose and fluid backflow along the device. These concepts can be applied to increase the dispersal of fluid infusates delivered through CED for the treatment of neoplasms or other neurological conditions. Future studies will focus on refinement of the FMD and rigorous testing of the hyperthermia-mediated dispersal enhancement hypothesis in *in vivo* conditions.

Chapter IV Supplement 1: Isothermal Agarose Experiments

4S1.1 Introduction

The results from the Agarose experiments and preliminary *ex vivo* porcine work described in Chapter 4 demonstrated that photothermal heating increases the volumetric dispersal rate of an infusate over long infusion timeframes. The data is further corroborated by the study detailed in Chapter 6, wherein a number of live rodents underwent simultaneous fluid infusion and photothermal heating with the FMD, further exhibiting the positive correlation between increased local temperature and volumetric dispersal rate. Although these experiments demonstrated a relationship, they did not serve to characterize the quantitative connectedness of heating and fluid dispersal. To quantify this relation, a second Agarose study was conducted wherein identical infusions into isothermal Agarose volumes at multiple different temperatures were performed within the shadowography setup described above.

4S1.2 Methods

4S1.2.1 Isothermal Agarose Infusions

A custom infusion setup was designed for conducting Agarose infusions in waterbaths providing isothermal and repeatable environments. T75 flasks were modified to by drilling four ports on the shorter side of the container (see Figure 29): three for FMD insertion and one for a micro-thermocouple. A simplified FMD design consisting of a silica capillary tube (365 µm outer diameter, 150 µm bore) glued into a 22G dispensing needle (McMaster-Carr) was employed for these experiments. Three FMDs were pressed firmly into the drilled side ports of each T75 flask and epoxied into place. Each FMD had a multimode fiberoptic (100/110/125 µm

core/cladding/jacket) inserted in its hollow bore to exclude liquid Agarose from rising into the tube due to capillarity. A layer of easily removable hot glue was used to temporarily seal the thermocouple port. Three-way T-couples were attached to the Luer connector of each 22G needle (the fiber passed through the T-couple and extended beyond the top). This assembly provided the inner housing around the Agarose that could be placed wholly inside an exterior waterbath.

Agarose was prepared at a 0.6% w/w mixture with de-ionized water as described above. After boiling, 275 mL of Agarose solution was poured into each prepped T75 flask. The flasks were sealed and water was injected through the T-couple into each infusion line, forcing out any air between the tip of the capillary tube to the top of the T-couple. The flasks were refrigerated at 4 ^{o}C for at least 24 hours to allow the Agarose to cure.

The shadowography setup used to capture the infusions progress was nearly identical to that described above. Additions included a large, transparent, plastic tub to contain the waterbath and a temperature control device. Infusions were conducted at four temperatures: 15, 20, 25, and 30 ^{o}C. For the 25 and 30 ^{o}C infusions, a hot plate provided heating for the waterbath. For the 15 and 20 ^{o}C infusions, a water chiller (make/model) maintained the waterbath at the desired temperature. The waterbath temperature was monitored continuously with a T-type thermocouple (Omega, Stanford, CT).

For each experiment, an Agarose flask was removed from refrigeration. The multimode fibers were carefully pulled out of the FMDs. Syringes (3 mL, BD) secured within a syringe pump

(Harvard Apparatus) were connected to each of the flask T-couples via micro-IV extension sets. Both the syringes and extension sets were filled with 5% FD&C Blue #2 dye prior to connection with the flask. The dye was allowed to freely diffuse throughout the small volume of water within the T-couple, which did not dilute the dye sufficiently to interfere with the shadowographic measurement. The hot glue over the thermocouple port was carefully removed and a T-type micro-thermocouple was inserted into the Agarose. A third T-type thermocouple was inserted into ice water to provide a cold junction for calibration. The flask was then placed within the waterbath and allowed to thermally equilibrate for at least one hour. A diagram of the experimental setup is shown below in Figure 29.

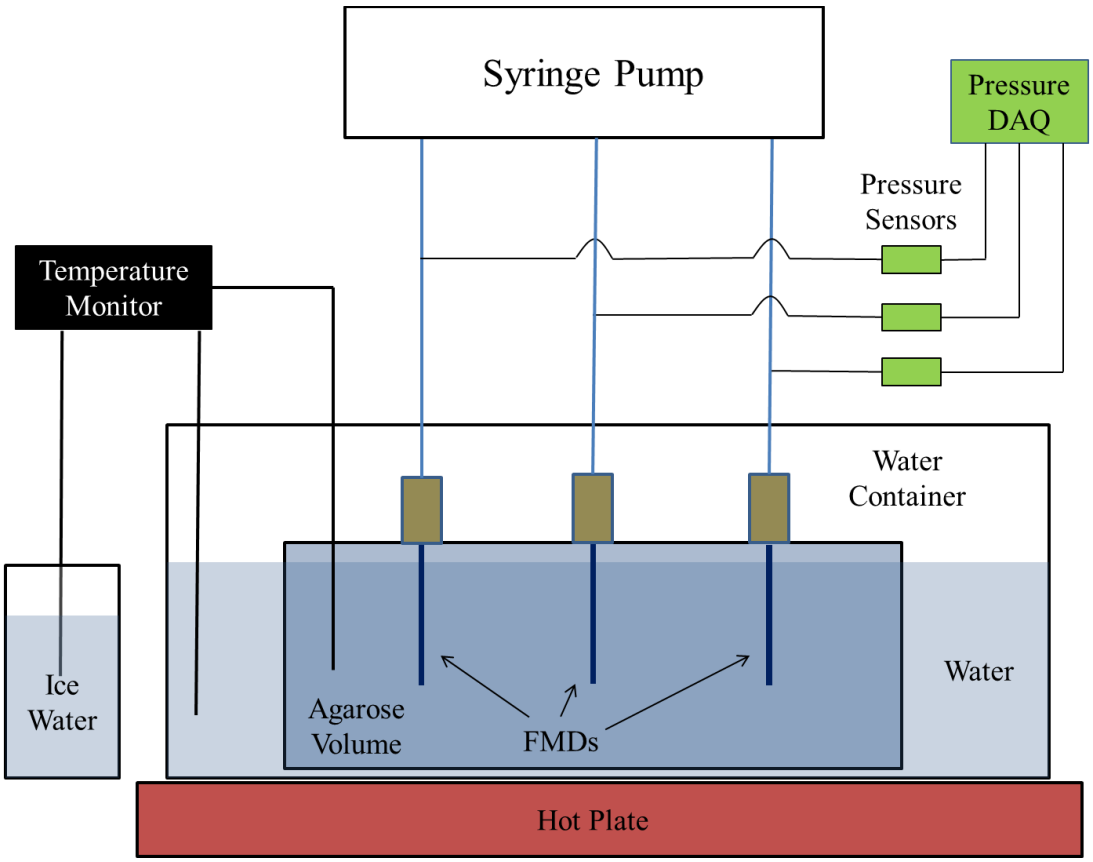

Figure 29: Diagram of Agarose infusion experimental setup.

Infusions were conducted at 1 µL/min for 100 minutes. Temperatures within the Agarose were maintained within ± 2 ^{o}C of their target or the infusion set was discarded. Line pressure for each infusion was monitored with wet/wet differential pressure sensors (Omega, Stamford, CT) connected in parallel of the micro-IV extension lines. The sensors were controlled by an 8-channel data acquisition unit connected to a laptop. Photographs were captured once per minute and processed as described above.

4S1.3 Agarose Experiment Results

At least N=4 experiments for each temperature were included in the volume distribution analysis. Exclusion criteria included dye front contact with the sides of the container, substantial reflux, temperature variation of >±2 ^{o}C of target, and line pressure exceeding 3 psi. Volumetric dispersal rate positively correlated with increasing temperature, and the 30 ^{o}C average V_d was over 7-fold greater than the 15 ^{o}C average at 100 minutes . A plot of the volume distribution as a function of time is shown in Figure 30.

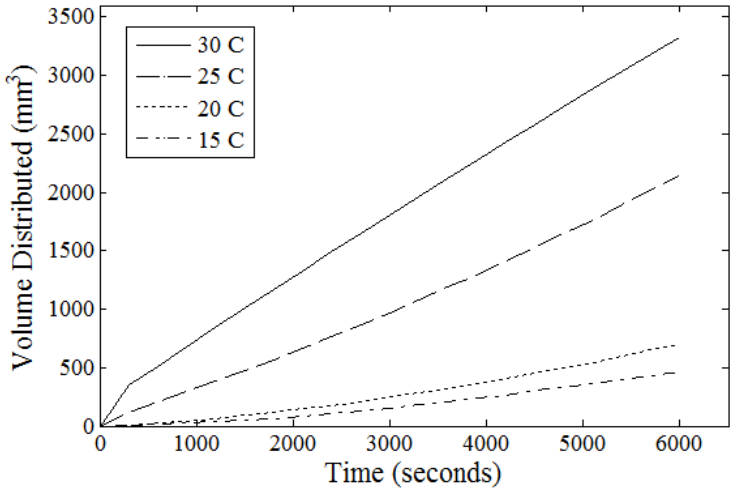

Figure 30: Volume distribution vs. time for each experimental temperature.

To determine statistical significance and provide a timepoint for the theoretical analysis described below, the volume at 100 minutes was chosen to compare between the different populations. A bar plot of the volume distributed for each temperature at 100 minutes is shown in Figure 31. A student t-test showed each of the populations to be statistically different at $p<0.05$.

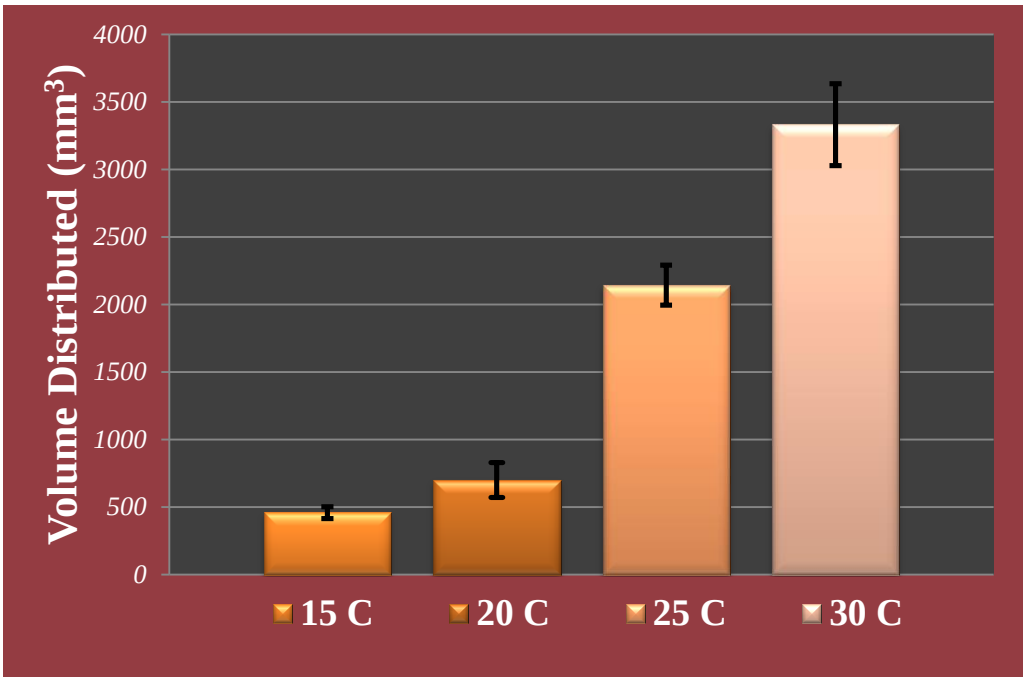

Figure 31: Bar plot showing volume distributed at 100 minutes for each temperature data set. Error bars depict the calculated standard error.

4S1.4 Poroelastic Model

A model developed by Chen *et al.* was modified and fit to our data in order to predict the temperature dependent effect on volumetric dispersal rate. Beginning with volume continuity and a modified Darcy's law equation describing the poroelastic case, Chen *et al.* developed a description of volume of distribution (*Vd*) as a function of pore fraction (φ) and dilatation (e), in addition to time (t). By modifying the equations describing convective transport through rigid porous media, the deformation behavior of the Agarose's porous "frame" was captured.

The dilatational diffusion constant is defined as $D_d \equiv k(\lambda + 2\mu)$, which includes contributions from the Darcy permeability of the Agarose (k) as well as the material rigidity (λ) and

compressibility (μ) moduli. For long time frames (where $t >> r^2/Dd$), the pore fraction can be written as a function of r:

$$\varphi(r,t) \approx \frac{A+\varphi_0 r}{A+r} \quad (6)$$

where A is defined as $A = q/(4\pi D_d)$, φ_0 is the initial pore fraction (t = 0), r is radius, and q is the volumetric flow rate. If $V_{inf} = qt$ (total infused fluid volume), the radius R of the resulting volume of distribution within the Agarose can be calculated by the equation

$$V_{inf} = \int_{r_0}^{R} dr\ 4\pi r^2 \varphi(r,t) \quad (7)$$

allowing the volume of distribution $V_d = 4\pi R^3/3$ to be determined.

Chen *et al.* estimated values for the different constants by employing a simultaneous least-squares procedure on a cost-function involving their measured and predicted pressure and distribution volume data. This group used the empirically-derived constants from Chen *et al.* and our experimentally measured V_d values to describe the dilatation diffusion constant D_d at each Agarose temperature. A plot of the calculated D_d value at each experimental temperature is shown in Figure 32. A quadratic regression was determined to provide the best fit through R^2 analysis between quadratic, exponential, and power law regressions in MatLab.

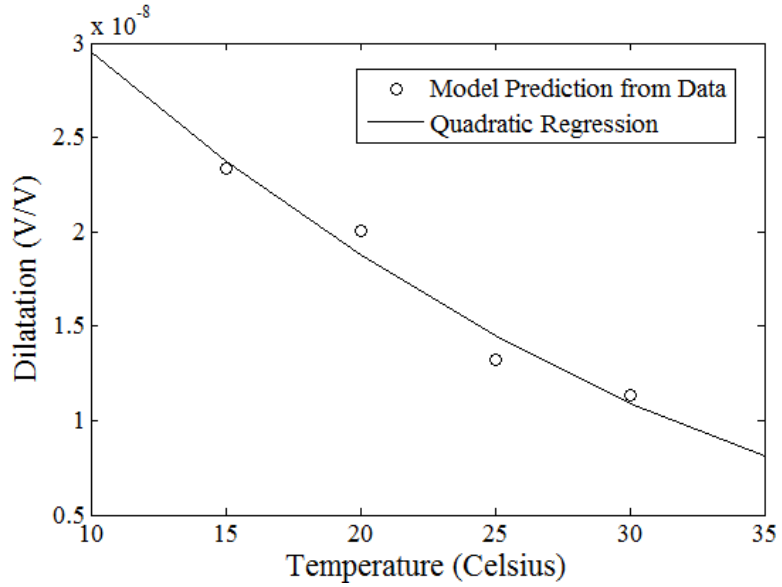

Figure 32: Dilatation coefficient calculated with the poroelastic model for each set of temperature data.

Using the quadratic fit equation for dilatational coefficient as an empirical model, a theoretical prediction for volume distribution as a function of temperature could be created. A plot of this prediction is shown in Figure 33.

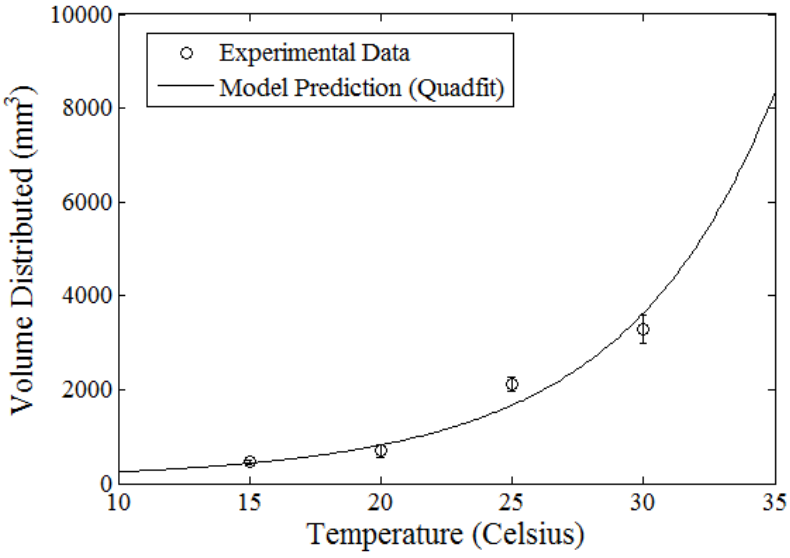

Figure 33: Volume distribution as a function of temperature plotted with the theoretical prediction from the calculated dilatational coefficients for each temperature.

4S1.5 Discussion and Conclusion

These additional Agarose experiments sought to quantify the relationship between the rate of volume increase and the Agarose's temperature. Experiments at 15, 20, 25, and 30 ^{o}C demonstrated a positive correlation between increased temperature and volumetric dispersal. Utilizing a model developed by Chen *et al.*, an empirical predictive model for the volumetric dispersal as a function of temperature after long infusion timeframes was developed.

Chapter V: Intracranial Hyperthermia through Local Photothermal Heating with the Fiberoptic Microneedle Device

5.0 Abstract

Background and Objectives: The fiberoptic microneedle device (FMD) seeks to leverage advantages of both laser-induced thermal therapy (LITT) and convection-enhanced delivery (CED) to increase volumetric dispersal of locally infused chemotherapeutics through sub-lethal photothermal heat generation. This study focused on determination of photothermal damage thresholds with 1064 nm light delivered through the FMD into *in vivo* rat models.

Materials and Methods: FMDs capable of co-delivering laser energy and fluid agents were fabricated through a novel technique of off-center fusion splicing of solid-core fiber to hollow-core capillary tubing. FMDs were positioned at a depth of 2.5 mm within the cerebrum of male rats with fluoroptic temperature probes placed within 1 mm of the FMD tip. Irradiation (without fluid infusion) was conducted at laser powers of 0 (sham), 100, 200, 500, or 750 mW. Evans blue-serum albumin conjugated complex solution (EBA) and laser energy co-delivery were performed in a second set of preliminary experiments.

Results: Maximum, steady-state temperatures of 38.7±1.6 and 42.0±0.9 ºC were measured for the 100 and 200 mW experimental groups, respectively. Histological investigation demonstrated needle insertion damage alone for sham and 100 mW irradiations. Photothermal damage was detected at 200 mW, although observable thermal damage was limited to a small penumbra of cerebral cortical microcavitation and necrosis that immediately surrounded the region of FMD

insertion. Co-delivery of EBA and laser energy presented increased volumetric dispersal relative to infusion-only controls.

Conclusion: Fluoroptic temperature sensing and histopathological assessments demonstrated that a laser power of 100 mW results in sub-lethal brain hyperthermia, and the optimum, sub-lethal target energy range is likely 100-200 mW. The preliminary FMD-CED experiments confirmed the feasibility of augmenting fluid dispersal using slight photothermal heat generation, demonstrating the FMD's potential as a way to increase the efficacy of CED in treating MG.

5.1 Background and Objectives

Malignant tumors of the central nervous system are the third leading cause of cancer-related deaths in adolescents and adults between the ages of 15 and 34; in children, brain tumors are the leading cause of death from solid tumors. Among malignant glioma (MGs) variants, glioblastoma multiforme (GBM) is the most common form of malignant tumor in the central nervous system, and is associated with a mean survival time post-diagnosis of 15 months and a mortality rate exceeding 95% [42]. Common treatments for MG include surgical resection, radiotherapy, chemotherapy, or combinations of these three modalities [43, 44]. Prior to the development of adjunctive therapy protocols combining radiation therapy and the chemotherapeutic drug temozolomide, fewer than 5% of patients survived more than 2 years. However, neither single nor multimodality treatments are curative with the combination of adjunctive therapies improving mean survival by a few months to a rate of 26% [42]. One of the reasons for poor survival is that glioma cells typically infiltrate up to 2 cm beyond the volume of visible tumor, making them difficult to detect and treat. Treatment of MGs is also limited by

insufficient delivery of chemotherapy drugs due to the blood-brain-barrier. Thus, new methods increasing treatment specificity for MG treatment are needed.

Convection-enhanced delivery (CED) has emerged as a promising method for delivering high concentrations of macromolecules to large regions of the central nervous system [46, 47]. CED involves the stereotactically-guided insertion of a small-caliber catheter into the brain parenchyma. Through this catheter, chemotherapeutic infusate is actively pumped into the brain parenchyma and disperses through the interstitial space [110]. Infusions can be continued for up to several days before catheters are removed [110]. In contrast to the millimeter distances obtained with simple diffusion, CED has been shown to deliver high molecular weight infusates 2 cm into the brain parenchyma after as little as 2 hours of continuous infusion [20]. This was accomplished without causing cerebral edema and was unaffected by capillary loss or metabolization of the macromolecule. With these initial experiments, CED was established as a viable method for providing regional distribution of molecules as large as immunotoxins and radioisotope–conjugated antibodies, as well as some conventional chemotherapeutic agents [18, 23-27].

Although CED achieved greater efficacy than traditional systemic chemotherapy, it failed to meet required clinical endpoints in a recent Phase III FDA trial [23]. This was attributed to the limited ability of CED to uniformly distribute drug throughout the targeted tumor and broadly disseminate drug to the infiltrative MG cells residing in the primary tumor periphery that are not detectable by MRI and ultimately correlate with tumor recurrence. The anatomical heterogeneity of the brain, which is amplified inside the GBM microenvironment, is a major limiting factor in

infusate distribution via CED. In particular, portions of the brain are inherently difficult to saturate with drugs due to variations in permeability of white and gray matter, tumor tissue, and cerebrospinal fluid tracts [23].

Laser-based treatment modalities, such as laser-induced interstitial thermal therapy (LITT), have received much research attention for development into alternative treatments for brain tumors [67-71]. LITT is a procedure wherein tumor tissue is destroyed through photothermal heat generation, accomplished through percutaneous introduction of light-conducting fiberoptics local to a target tumor [68]. LITT's minimally invasive nature and fiberoptic presentation infer a high degree of compatibility with magnetic resonance imaging, benefitting especially from magnetic resonance thermometry (MRT) [69, 72]. MRT enables real-time identification of thermal gradients, allowing LITT to be adapted to tumor geometry and dynamic surgical conditions. However, LITT's efficacy is limited by the unpredictability of thermal gradients due to the heterogeneity of brain tissue, which is only increased by the presence of a solid tumor [70, 73]. Additionally, thermal ablation can cause edema, which can be a dangerous side effect when trying to preserve critical cerebral structures [74, 75].

Clinical and laboratory evidence has shown that heating chemotherapeutic agents (termed thermochemotherapy) enhances fluid penetration into peritoneal tumors [59]. This is an intuitive effect as both convective and diffusive fluid transport increase with temperature. In addition, sub-lethal levels of hyperthermia have been demonstrated to increase the cytotoxic effects of several chemotherapeutic drugs [60-62]. Potential rationale for this observed enhancement owes to increased plasma membrane permeability and cell metabolic processes. Introducing a

hyperthermic element into CED could potentially increase volumetric distribution and chemotherapeutic efficacy.

Motivated by the limitations of LITT and CED and the benefits of thermochemotherapy, a fiberoptic microneedle device (FMD) has been developed to enable greater treatment versatility through permitting simultaneous co-delivery of laser energy and fluid agents. This technology is based on light-guiding capillary tubing that enables fluid conduction through a hollow bore as laser energy is conducted within the annular wall. Our group has published microneedle fabrication techniques and results of mechanical penetration into tissue [76], and have demonstrated the properties of these microneedles pertaining to both light and fluid delivery [106, 111]. The potential applications of this technology applied to LITT include concurrent delivery of a cooling medium, light absorbing chromophores, image contrast agents, or chemotherapuetics. The current envisionment of FMD technology is to combine elements of LITT with CED, using slight hyperthermia beneath the threshold for thermal damage to increase perfusive distribution of macromolecules for a broader and more uniform infusion volume.

The objective of this study was to determine photothermal damage thresholds for 1064 nm light delivery through the FMD into *in vivo* cerebral tissue. The 1064 nm wavelength was chosen for its deep penetration depth of 1-5 mm in cerebral tissue [112]. Preliminary experiments in *ex vivo* tissue identified an input power of 500 mW to not be associated with thermal damage over a short timeframe. The study hypothesis was that interstitial delivery of 500 mW into rat brain tissue would be sub-lethal to brain cells, indicating it is an acceptable laser power to be used in conjunction with FMD-CED co-delivery procedures.

5.2 Materials and Methods

5.2.1 Fiberoptic Microneedle Device Fabrication

Previous publications have described the FMD's evolving state of development, which has progressed to the current prototype incorporating a hollow fiberoptic (HF) capable of delivering both fluids and light simultaneously [76, 106, 111]. The HF is commercially available, light-guiding, fused silica capillary tubing (365 µm outer diameter, 150 µm inner diameter, Polymicro Technologies, Phoenix, AZ) angle-polished at the tip to produce a sharp, beveled microneedle, as shown in Figure 34C. Light conduction is achieved by the principle of total internal reflection within the annular, fused silica core (305 µm OD, n = 1.46) by having an exterior cladding layer of doped silica (15 µm OD, n= 1.44) and a fluid medium with a lower refractive index inside the inner bore [103]. The capillary was angle-polished at an approximately 45º angle, giving the light transmitting tip a core surface area of approximately 0.055 mm^2. Keller *et al.* demonstrated that total internal reflection is maintained when an index matching fluid is within the hollow bore, as light traverses the fluid and core to reflect from the cladding interface on the far side [113]. The HF is manufactured with a 40-60 µm polyimide jacket around the outer cladding layer to provide lateral support and protection.

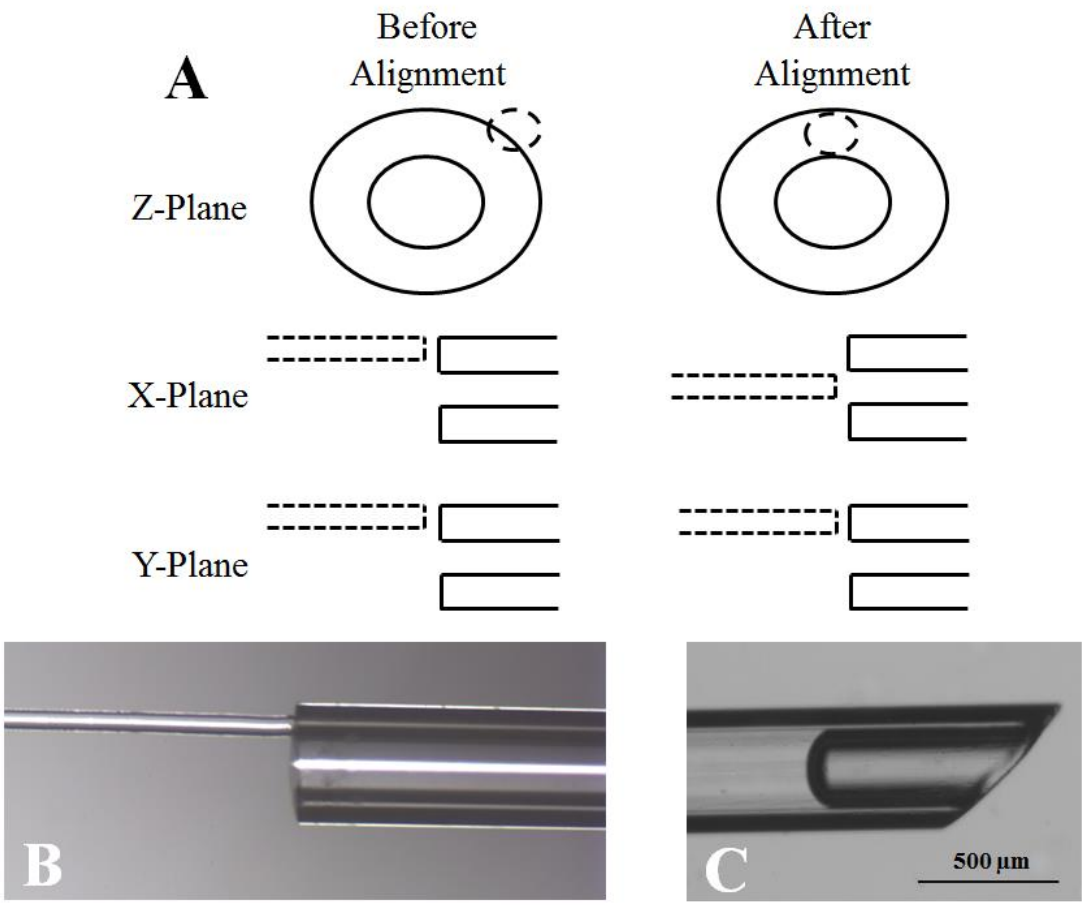

Figure 34: A- Schematic of fiber alignment, not to scale. B- Successful fusion splice. C- Polished microneedle tip. Scalebar is conserved between B and C.

To fabricate a prototype capable of co-delivery, the HF was coupled with both a solid, multi-mode fiberoptic (SF) (80 µm outer diameter, 50 µm core diameter, Polymicro Technologies, Phoenix, AZ) and a 30G syringe needle (Becton, Dickinson, Franklin Lakes, NJ) sheathed inside 450 µm inner diameter fused silica capillary tubing (TSP450670, Polymicro Technologies, Phoenix, AZ). To ensure high light coupling efficiency, the SF was fusion spliced to the annular core of the HF using a Sumitomo Type-36 Fusion Splicer (Sumitomo Electric Lightwave Corp., Research Triangle Park, NC). The Type-36 Fusion Splicer utilizes a high power electric arc

created between two electrodes to bond two fiberoptics through brief melting. The off-center nature of the splice necessitated a manual alignment of the fiberoptics.

Prior to splicing, the polyimide jacket was removed from a short length (approximately 3 mm) of the fibers at both ends of both the HF and SF through submersion in heated sulfuric acid (96.5% to approximately 200 ºC, ScienceLab.com Inc., Houston, TX). Both ends of the SF and one end of the HF were flat-polished with a graded series of lapping films from 60 to 0.5 µm on an Ultrapol 1200 End and Edge Polisher (UltraTec Manufacturing, Inc., Santa Ana, CA). The non-spliced end of the HF was polished at an approximately 45º angle to create a sharp, microneedle profile to ease insertion into tissue, as shown in Figure 34B. The splicing procedure began with a SF and a HF being placed in the fusion splicer's fiber holders and electrically spattered, accomplished through a low power arc passed over the fiber tips to remove any contaminants (dust, etc.) or remnants of the polyimide jacket. The Type-36 utilized two CCD cameras allowing orthogonal viewpoints of the fiberoptics and stepper motors allowing micron resolution movement control in three dimensions. Once spattered, the fibers were aligned top-to-top from both viewpoints. The HF was translated 115 µm in the positive y-direction and 15 µm in the positive x-direction, achieving an alignment with the annular core of the HF. This alignment process is shown in Figure 34A. Once the proper off-center alignment was attained, the splice was conducted with the following parameters: 2 s arc duration, 0.1 s pre-fusion duration, 10 µm arc gap, 5 µm overlap, and 17 step arc power ("step" is a proprietary Sumitomo unit). A successful splice is shown in Figure 34B.

Once spliced, the joined fibers were placed within a protective length of TSP450670 fused silica capillary tubing (inner diameter 450 µm, Polymicro Technologies, Phoenix, AZ). A 30G syringe needle was inserted parallel to the SF and placed in close proximity to the splice inside the sheath, enabling fluid coupling to the HF through the Luer-Lok connector as shown in Figure 35. Both ends of the sheath were sealed with an EP30 MED (Master Bond Inc., Hackensack, NJ), a biocompatible epoxy optically translucent at the 1064 nm wavelength utilized in this study. Splices had varying amounts of light conduction loss, so the silica sheath and epoxy allow light transmission to reduce absorptive heating local to the splice from leaked light. A schematic of this co-delivery couple is shown in Figure 36. The co-delivery couple was made more robust through encasing the silica sheath within a larger, polyether ether ketone sheath (PEEK, Chrom Tech, Inc., Apple Valley, MN), which shields the device from the Luer-Lok connection to the last 1-2 cm of the HF. The PEEK sheath provides greater reinforcement against breakage from lateral loading and torsion at the Luer connection when attaching a fluid line. Images of the co-delivery couples before and after the addition of the PEEK sheath are shown in Figures 35A and 35B.

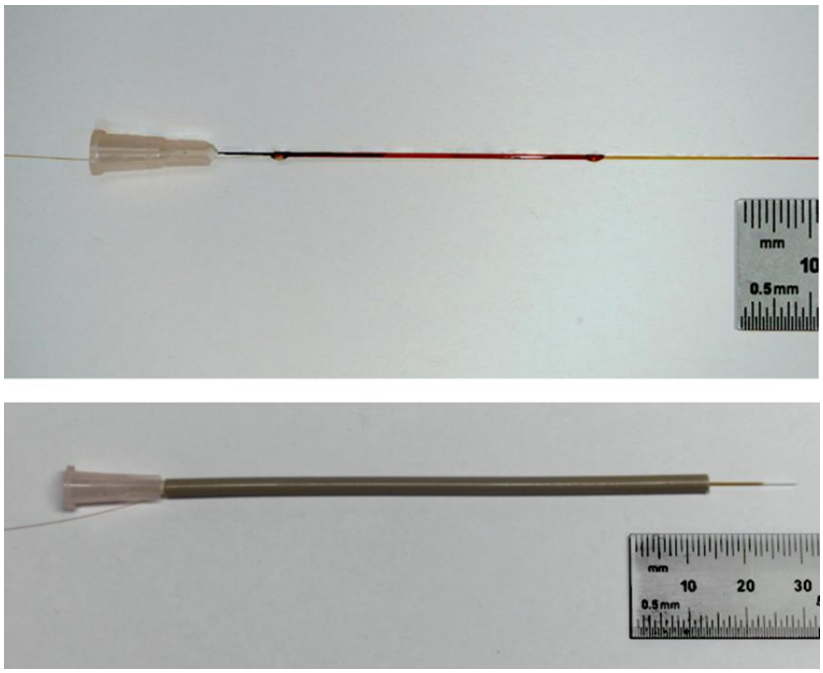

Figure 35: Top- Co-delivery couple with only capillary tube for support. Bottom- Co-delivery couple with robust PEEK tubing support.

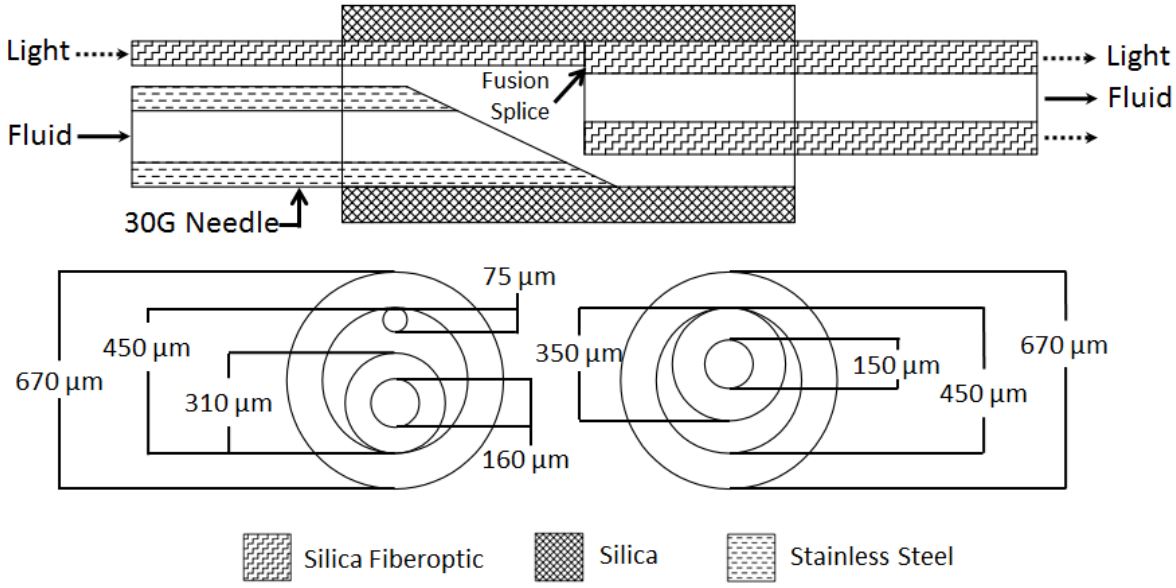

Figure 36: Schematic of FMD co-delivery couple design.

5.2.2 Animals and Craniectomy Procedure

All study procedures were conducted following Institutional Animal Care and Use Committee approval (CVM-12-057) and performed in a GLP compliant facility. Fifteen, male Fischer 344 rats weighing 220-250g were pre-medicated with buprenorphine (0.02 mg/kg subcutaneously), and anesthetized with isofluorane delivered via induction chamber. Anesthesia was maintained with isofluorane delivered via nosecone, and a surgical plane of anesthesia assessed by loss of the tail or toe pinch reflex. The hair of the skull was clipped and aseptically prepared using povidone-iodine and alcohol solutions. Anesthetized rats were placed in a small animal stereotactic head frame (Model 1350M, David Kopf Instruments, Tungisten, CA, USA). A routine rostrotentorial surgical approach to the skull was made and a 3 mm in diameter circular parieto-occipital burr-hole craniectomy defects were created in the right aspect of the skull of each rat using a high-speed electric drill at the following stereotactic locations relative to the bregma: 4 mm posterior and 3 mm lateral. In the instances a bilateral treatment was performed (Table 4), a mirror image craniectomy defect was created in the left aspect of the skull. FMDs were then advanced to a depth of 2.5 mm beneath the surface of the exposed dura through each craniectomy defect using the manipulator arm of the stereotactic frame.

5.2.3 FMD Photochemotherapeutic Treatment

Brains underwent FMD treatments according to the treatment matrix depicted in Table 4. The lowest power delivered of 100 mW corresponded to an irradiance transmitting from the beveled microneedle tip of 1.8 W/mm^2. In the rats in which CED infusion was performed, an Evans blue-serum albumin conjugated complex solution (EBA) was infused. EBA was prepared using a previously described protocol [114]. Briefly, EBA with a final concentration of 0.2 mg/ml, was

formulated by diluting a 2% solution of Evans blue (Sigma, St. Louis, MO, USA) 100 fold in a 4% bovine serum albumin solution. All EBA CED infusates were delivered at a rate of 0.1μL/min for 60 minutes using a two channel microinfusion pump (PhD Ultra, Harvard Apparatus, Harvard, MA, USA). The infusion rate of 0.1 μL/min was shown by Chen *et al.* to be associated with negligible reflux and reduced ventricular penetration in an *in vivo* rodent model [115].

Near-infrared laser light was coupled from the 1064 nm continuous wave laser (IPG Photonics, Oxford, MA) into the SF input of the FMD using a free space to fiberoptic coupler (Newport Corporation, Irvine, CA). The distal end of the FMD was placed into a calibrated integrating sphere (918D-SL-OD1, Newport Corporation, Irvine, CA) to ensure proper alignment of the SF in the coupler apparatus and ensure that the FMD was outputting the desired power. A single FMD with a light coupling efficiency of approximately 55% was used for all experiments. The FMD was also placed within a thermopile (LM-10HTD, Coherent Inc., Santa Clara, CA) to determine the differential reading between the thermopile and integrating sphere. This was necessary as the integrating sphere could not be used to measure the FMD's output power once the device was mounted on the stereotactic frame due to space constraints. Power values were checked before and after every experiment. The integrating sphere was the most accurate power measurement device available, so all reported power values originate from that device.

Once the desired laser output was attained from the FMD, the FMD was mounted on the stereotactic frame. For experiments involving a sham FMD or an infusion only FMD for the left hemisphere, a second FMD was mounted on the frame, such that their distal tips were co-

terminating and 6 mm apart. For the temperature determination experiments (non-infusion), a fluoroptic temperature probe (STB Probe, LumaSense Technologies, Santa Clara, CA) was placed along the experimental FMD with the tip 1 mm behind the FMD tip. Temperature measurements were recorded at 2 Hz for the duration of the experiment, initiating when the FMD was inserted into the brain tissue. Temperature measurements from the fluoroptic probes were influenced by interference from the 1064 nm laser to the extent of masking useful data. To obtain meaningful measurements, the laser was stopped once every 10 minutes for 15 seconds over the duration of the experiment.

Following completion of the infusions, the FMD were withdrawn from the brain, and the rats euthanatized by intraperitoneal injection of 1 ml of phenytoin-pentobarbital solution (Beuthanasia-D [390 mg phentobarbital sodium and 50 mg phenytoin per ml], Intervet Laboratories, Summit, NJ, USA) followed by cervical dislocation.

5.2.4 Brain Pathology

Immediately following sacrifice, the brains were harvested *in toto*, examined and photographed for evidence of gross damage. The brains were then immersion fixed in 10% neutral buffered formalin for 48 hours at room temperature. Formalin-fixed brains were serially sectioned in the coronal plane at 1 mm thick intervals using a young rat matrix slicer (Zivic Instruments, Pittsburg, PA, USA).

The 1 mm thick brain slices obtained from the matrix were further sectioned at 5 μm intervals, stained with hematoxylin and eosin (H&E), and examined with light miscroscopy for

morphologic evidence of thermal or mechanical damage to the brain resulting from the FMD-CED treatments. EBA infused brain specimens were counterstained with hematoxylin only.

5.3 Results

5.3.1 Brain Temperature

Data collected through turning off the laser for 15 second intervals every 10 min produced repeatable data for the 100 and 200 mW experimental groups. The average steady-state temperature was 38.7±1.6 and 42.0±0.9 ºC for laser irradiation at 100 and 200 mW, respectively. Due to observed variation in the rodents' core temperature over the course of the procedures, values for the normalized change in temperature (ΔT) were computed from deducting the averaged steady-state core temperature before and after the laser irradiations from the measured peak values when the laser was deactivated. These normalized ΔT values were 2.98±1.07 and 5.24±0.82 °C for 100 and 200 mW, respectively. A representative graph showing the measurements at each laser deactivation for a 200 mW irradiation is shown in Figure 37.

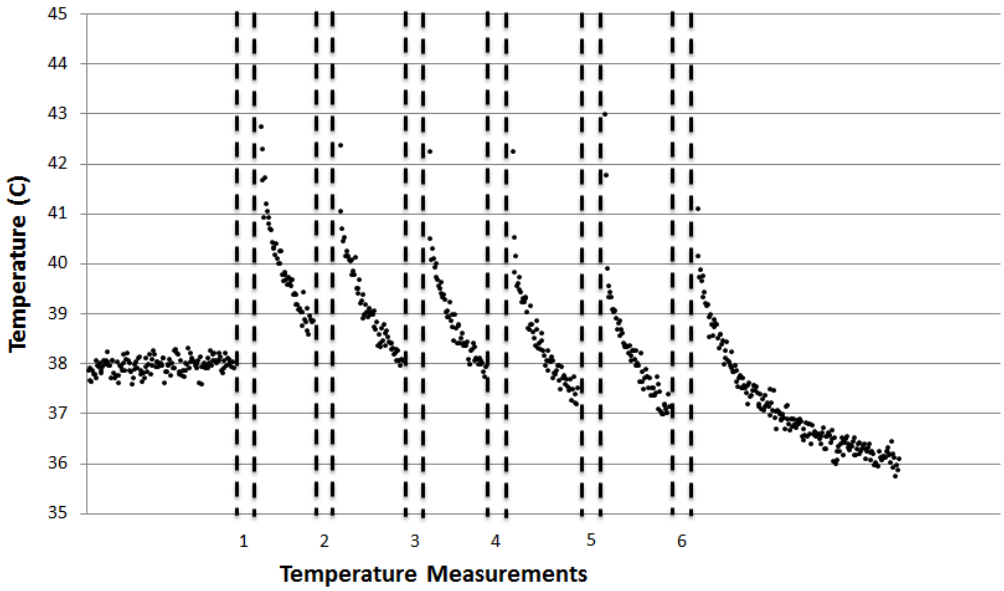

Figure 37: Six temperature measurements spaced at t = 10, 20, 30, 40 50, and 60 min. Each sampling is approximately 15 seconds in length, with the exception of the final measurement, where the temperature was allowed to return to steady-state (rat's core temperature). Variation in the steady-state temperatures before and after the laser irradiations were due to core temperature variation within the anesthetized rodent.

5.3.2 Brain Pathology

No abnormalities were observed in untreated cerebral cortices. In both sham FMD treated (Figures 38A, 38F) and FMD 100 mW treated (Figure 38B, 38G) rats, morphological damage was limited to physical displacement of the cerebrocortical tissue and associated microvascular hemorrhage in the trajectory of the FMD insertion. At laser energies above 100 mW, FMD treatment was associated with evidence of morphologic evidence of thermal brain injury. In rats treated with FMD 200 mW, thermal injury was limited to a small penumbra of cerebral cortical microcavitation and necrosis that immediately surrounded the region of the FMD insertion (Figure 38C and 38H). In rats treated at FMD 500 and FMD 750 mW, there were extensive regions of brain tissue pallor resulting from coagulative necrosis and intraprenchymal

hemorrhage that resulted in obliteration of the brain tissue architecture (Figure 38D, 38I, 38E, and 38J). At 500 mw and 750 mW, thermally injured injured regions extended radially to effect areas deep (Figure 38D and 38E), rostral (anterior; Figure 38D), and caudal (posterior; Figure 38E) to the level the FMD insertion including the lateral ventricle and subcortical structures. In 3/5 FMD 500 mW treated rats and 3/3 of FMD 750 mW rats, the region surrounding the FMD insertion was malacic and resulted in a full thickness, cavitary cerebrocortical defect (Figure 38D, arrows). There was a positive association between the severity and size of regions of thermally-induced brain damage and the laser power delivered (Figure 38C, 38D, and 38E).

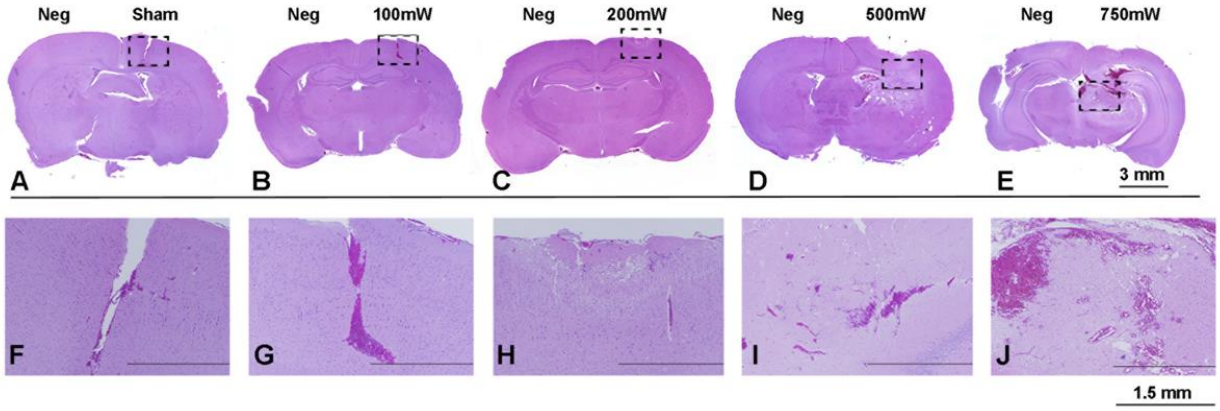

Figure 38: Photothermal effects of FMD delivered laser energy in rat brain. Brain tissue damage is mechanical and limited to the trajectory of the FMD needle insertion in both sham (A, F) and FMD 100 mW (B, G) treated cortices. Collateral photothermally-induced necrosis of cortical and subcortical structures becomes more severe with increasing laser power $\geq$ 200 mW (C,D,E, H, I, and J [insets]). All sections stained with hematoxylin and eosin.

5.3.3 Pilot FMD-CED Infusions

In rats undergoing FMD-CED procedures with EBA (Table 4), the region of infusate distribution was larger in cerebral cortices treated with co-delivery of laser energy (Figure 39A). In the FMD 100 mW treated rat, damage to the brain tissue as the result of the infusion was limited to microhemorrhage along the FMD insertion tracks and a focal area of coagulative necrosis within the cerebral cortex at the FMD needle tips (Figures 39A- arrows, 39B, and 39C). The observed changes in the brain were similar between the FMD control and FMD 100 mW irradiated cortices (Figure 39B and 39C). In the FMD 200 mW treated rat, reflux up the FMD insertion track, infusate leakage into the lateral ventricles, and extension of coagulative necrosis of the cerebral cortical tissue adjacent to the FMD 200 mW insertion region, similar to that illustrated in Figures 39C and 39H, were observed (data not shown).

Table 4: Treatment variables for each hemisphere. Sham FMD indicates insertion without treatment.

Rat Number	Right Side	Left Side
1	Sham FMD	Untreated
3	FMD 100 mW	Untreated
2	FMD 200 mW	Untreated
3	FMD 500 mW	Untreated
2	FMD 500 mW	Sham FMD
2	FMD 750 mW	Untreated
1	FMD 750 mW	Sham FMD
1	FMD-EBA 100 mW	FMD-EBA
1	FMD-EBA 200 mW	FMD-EBA

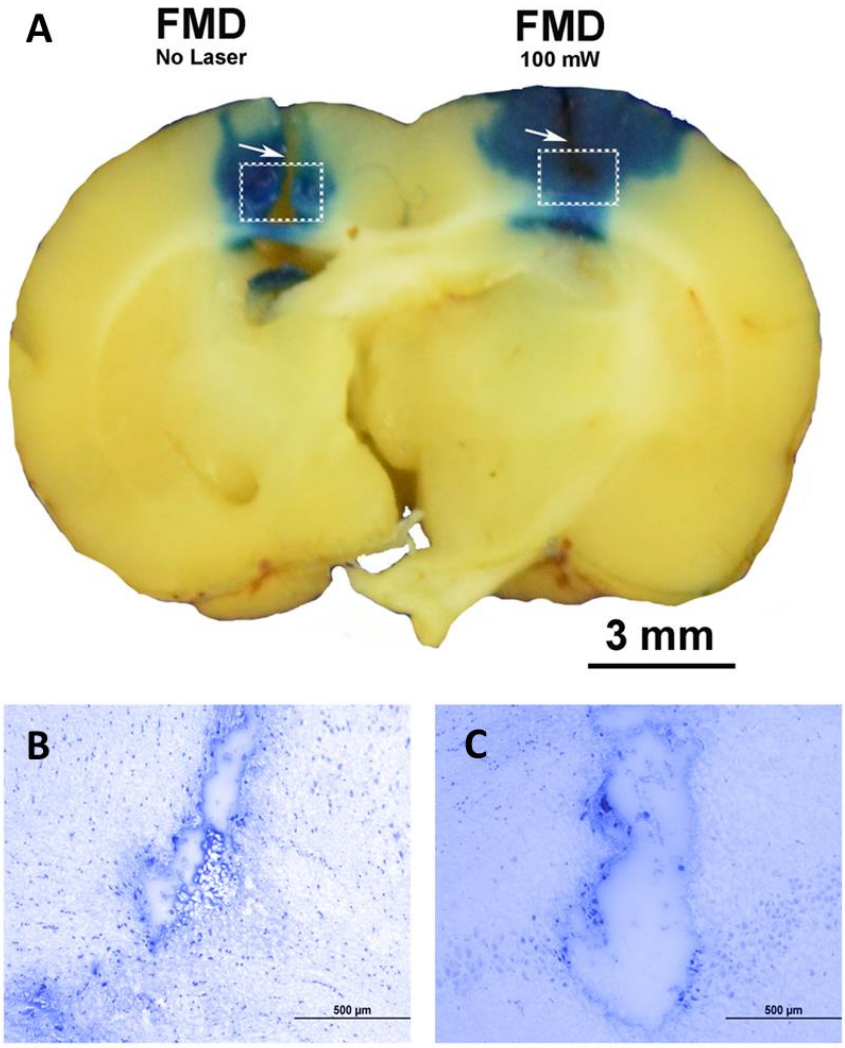

Figure 39: FMD-CED infusion of EBA into rat cerebrum. A- Gross brain slice preparation demonstrating larger distribution of EBA infusate in FDM 100 mW laser treated cortex compared to control. B and C- Brain tissue damage associated with FMD infusions is minimal and limited to the trajectory of the FMD needle insertions; hematoxylin counterstain.

5.4 Discussion

This study was conducted to determine laser power parameters with which to conduct simultaneous *in vivo* CED co-delivery of fluids and laser light without causing thermal damage.

Using fluoroptic temperature sensing and histopathological assessments, we identified that a laser power of 100 mW results in sub-lethal brain hyperthermia, and the optimum, sub-lethal target energy range is likely 100-200 mW. The preliminary FMD-CED experiments confirmed the feasibility of augmenting fluid dispersal using sub-lethal photothermal heat generation.

Analysis of the fluoroptic temperature measurements yielded values of 38.7±1.6 and 42.0±0.9 ºC for the 100 and 200 mW experimental groups, respectively. These are the averaged quantities measured immediately following laser deactivation at 10 minute intervals, yielding six measurements for each experiment and averaged between experiments. As the fluoroptic sensors were approximately 1 mm away from the FMD tip, temperatures measured may not have been the absolute maximum. Other events, such as local hemorrhage, were not consistent between experiments or timepoints and would also influence measurements. However, the repeatable exponential decay curve following deactivation and, more importantly, the histopathology, lent confidence to the measurements. These metrics also caused the rejection of the 500 and 750 mW data, as the decay curves were non-repeatable and frequently exhibited unrealistic values. This may have been an effect of the rapid temperature decay being more sudden than the probes could recover from the laser interference.

In addition to the fluoroptic sensors described, temperature measurement was attempted with several T-type thermocouples (Omega Engineering, Inc., Stamford, CT), which encountered interference from the brain's electrical activity. The original hypothesis of 500 mW being sub-lethal was obtained from preliminary experiments in *ex vivo* porcine cerebral tissue using the thermocouples and a literature derived target temperature of 42-43 ºC as a threshold for

increased heat shock protein expression and thermal damage [116-120]. This proved to be an overestimation for the *in vivo* case presented in the rodent model, as the thermal damage threshold was determined to be between 100-200 mW. The overestimation may have been instigated by the different optical and thermal properties of *ex vivo* tissues, in addition to the use of a sensor that was less sensitive and spatially exact than the fluoroptic probes. These issues aside, the data indicates a target laser power range of 100-200 mW to be utilized and optimized in subsequent studies.

The CED co-delivery pilot experiments indicate that increasing interstitial fluid dispersion in the brain using local hyperthermia is feasible with the described FMD platform. This effect could be attributable to a host of interconnected hyperthermia-related reasons. Diffusive and convective transport increase with temperature, while fluid viscosity decreases. The porosity of the surrounding extracellular matrix may increase with temperature. Salcman *et al.* described cerebral blood vessel dilation and leakage through the blood brain barrier associated with hyperthermic temperatures of 42-43 °C [121]. Determining the specific mechanisms of this effect was not an objective of this study, and while these results are preliminary, they support this application of FMD co-delivery technology and will be further tested in future experiments.

While photothermal means were employed for local hyperthermia in these experiments, one could argue that similar results could be obtained through heat generation with electrical resistance or radiofrequency excitation [122, 123]. Laser heat generation has the advantages of being non-ionizing, locally delivered, and volumetric, as 1064 nm laser energy high penetration depth of 1-5 mm in brain tissue [112]. Additionally, laser-induced hyperthermia as presented in

this chapter benefits from being MR compatible, compact in its interface with the patient, associated with diffuse heat generation millimeters from the probe's tip, and co-terminal in its delivery of laser energy and fluid agents, ensuring that the fluid and heat fields are spatially co-registered. Cerebral tissue is also highly scattering, causing directionality of the emitted laser energy to be quickly lost and generating an amorphous heating profile around the FMD tip [124]. FMD technology seeks to leverage these advantages of photothermal heating to increase the volume dispersal and uniformity of chemotherapies delivered through CED.

The authors envision the FMD being deployed to treat MG currently identified as candidates for CED. The small diameter of the FMD catheters (~360 μm) cause minimal tissue disruption, enabling several to be stereotactically placed to maximize chemotherapeutic saturation of the tumor and surrounding margins. While the photothermal heating may increase the fluid agent dispersal, additional advantages may be leveraged by this technique. Studies have shown that some chemotherapeutics are more effective when delivered adjunctively with slight hyperthermia, a mechanism attributed to heat-mediated increases in cellular porosity and metabolism [125-127]. Heat-mediated reduction in the blood-brain barrier's function could increase the efficacy of an adjunctively administered systemic chemotherapeutics that may not normally be able to cross the blood-brain-barrier Although the brain application envisioned does not involve thermal tissue damage, the FMD could also be used for LITT, as demonstrated by the ability of FMD to thermally ablate brain tissue at the 500 and 750 mW irradiations. We conclude that the FMD platform described here may have multiple indications for use in intracranial surgery.

Chapter VI: Enhanced Volumetric Dispersal of Intracranial Infusates through Photothermal Hyperthermia with the Fiberoptic Microneedle Device

6.0 Abstract

Background and Objectives: A fiberoptic microneedle device (FMD) was designed and fabricated for the purpose of enhancing the volumetric dispersal of macromolecules delivered to the brain through convection-enhanced delivery (CED) by concurrent delivery of sub-lethal photothermal hyperthermia. This study's objective was to demonstrate enhanced dispersal of fluid tracer molecules through co-delivery of 1064 nm laser energy in an *in vivo* rodent model.

Materials and Methods: FMDs capable of co-delivering fluids and laser energy through a single light-guiding capillary tube were fabricated. FMDs were stereotactically inserted symmetrically into both cerebral hemispheres of 16 anesthetized rats to a depth of 1.5 mm. 1064 nm laser irradiation at 0 (control), 100, and 200 mW was administered concurrently with CED infusions of liposomal rhodamine (LR) or gadolinium-Evans blue-serum albumin conjugated complex (Gd-EBA) at a flow rate of 0.1 µL/min for 1 hour. Line pressures were monitored during the infusions. Rodents were sacrificed immediately following infusion and their brains were harvested, frozen, and serially cryosectioned for histopathologic and volumetric analyses.

Results: Analysis by ANOVA methods demonstrated that co-delivery enhanced volumetric dispersal significantly, with measured volumes of 15.8±0.6 mm^3 for 100 mW compared to 10.0±0.4 mm^3 for its fluid only control and and 18.0±0.3 mm^3 for 200 mW compared to 10.3±0.7

mm^3 for its fluid only control. Brains treated with 200 mW co-delivery exhibited thermal lesions, while 100 mW co-deliveries were associated with preservation of brain cytoarchitecture.

Conclusion: Both lethal and sub-lethal photothermal hyperthermia substantially increase the rate of volumetric dispersal in a 1 hour CED infusion. This suggests that the FMD co-delivery method could reduce infusion times and the number of catheter insertions into the brain during CED procedures.

6.1 Background and Objectives

Systemic delivery of high molecular-weight therapeutic agents for lesions in the central nervous system is demonstrably regulated by the blood-brain barrier (BBB) [128-131]. One method developed for overcoming regulation imposed by the BBB is convection-enhanced delivery (CED), where the BBB is bypassed by transdural insertion of a slender cannula and active infusion directly within lesions [47, 110]. CED has been demonstrated to deliver high molecular weight macromolecules up to 2 cm into the brain parenchyma after a 2 hour infusion without causing cerebral edema [20]. CED's potential for regional distribution of large macromolecules has led to related studies for treating several cerebral disorders, such as Parkinson's, epilepsy, Alzheimer's, and intracranial malignancies [49-51].

To preclude detrimental increases in intracranial pressure, CED typically requires infusion flow rates to be 10 µL/min or less. This necessitates infusion timeframes of up to 3-4 days for treatment of large tissue volumes [110, 132]. CED requires highly accurate catheter placement, as fluid reflux and the differences in hydraulic resistance of gray and white matter can

significantly impact dispersal geometries [51, 115]. These limitations of CED were identified as heavily contributing to the results of the PRECISE trial, where CED was used to deliver IL13-PE38QQR (cintredekin besudotox) for treatment of malignant gliomas. In a retrospective evaluation, Sampson *et al.* indicated that the failure to meet clinical endpoints was not attributable to the therapeutic efficacy of the chosen infusate, but rather to the CED technique itself not providing sufficiently broad and uniform distribution of the immunotoxin [23]. As even the most selective and potent chemotherapeutic agents must reach their target to be effective, there is a need to improve CED through improved implementation and engineering solutions.

We have previously provided preliminary data that demonstrates the feasibility and potential of photothermal heating during infusion for improving volumetric dispersal during CED [105]. Thermochemotherapy is defined as the heating of chemotherapeutic agents to enhance tumor penetration; it is routinely utilized in the treatment of peritoneal tumors [59, 133]. On a macroscale level, this enhancement can be attributed to temperature-based increases in fluid diffusion and convection, as well as a reduction in fluid viscosity [134]. Local hyperthermia has been demonstrated to dilate cerebral arterioles [135]. Additionally, hyperthermia of up to 43 ºC has been shown to increase the potency of select chemotherapeutics *in vitro* [60-62]. This augmentation was attributed to temperature based increases in cellular membrane permeability and metabolism. The synergistic potential of facilitating CED by inclusion of sub-lethal hyperthermia may improve the efficacy of CED, making it a viable and effective treatment for cerebral disorders, such as malignant glioma.

To determine if CED could be augmented with aspects of thermochemotherapy, the fiberoptic microneedle device (FMD) technology developed by this group was adapted for intracranial use [105]. FMD technology is based on light-guiding, silica capillary tubing capable of simultaneously co-delivering laser energy and fluid agents. This capillary tubing can be angle-polished at the tip to create a sharp, beveled profile. Previous development and experimentation included various fabrication techniques, mechanical penetration experiments, and characterization of light and fluid delivery into tissue [76, 106, 107, 136]. In a previous study conducted by this group, the sub-lethal photothermal damage threshold in the brain for 1064 nm laser energy delivered through the FMD was determined to be between 100 and 200 mW [105]. For this study, the FMD was used to generate mild hyperthermia through photothermal heating with 1064 nm laser energy at the point of infusion. We hypothesized that concurrent generation of hyperthermia through FMD photothermal heating during CED would improve volumetric dispersal of infusates.

6.2 Materials and Methods

6.2.1 Fiberoptic Microneedle Device Fabrication

Previous publications have described the FMD's evolving state of development, which has progressed to the current prototype incorporating a light-guiding, silica capillary tube (LTSP150735, Polymicro Technologies, Phoenix, AZ) capable of delivering both fluids and light simultaneously [76, 106, 107]. This group has previously described the devices used for this study in detail [105]. Briefly, FMDs were fabricated through a patent-pending technique wherein a multimode fiberoptic (100/110 core/clad) was fusion spliced to a section of the light-guiding capillary's annular wall. The splice region was subsequently encased within a closed fluid system with a single inlet coupled to a Luer-Lock connector for fluid input. Thus, both fluid and

light could be coupled into a single capillary tube. The distal end of the capillary was polished to an approximately 45º angle for a sharp, beveled tip.

6.2.2 Animals and Craniectomy Procedure

All study procedures were conducted following Institutional Animal Care and Use Committee approval and performed in a GLP-compliant facility. Sixteen (16), male Fischer 344 rats weighing 220-250 g were pre-medicated with buprenorphine (0.02 mg/kg subcutaneously), and then anesthetized with inhaled isofluorane delivered via induction chamber. Anesthesia was maintained with inhaled isofluorane delivered via nosecone; provision of a surgical plane of anesthesia was assessed by loss of the tail or toe pinch reflex. The hair of the skull was clipped and aseptically prepared using povidone-iodine and alcohol solutions. Anesthetized rats were placed in a small animal stereotactic head frame (Model 1350M, David Kopf Instruments, Tungisten, CA, USA). A routine bilateral rostrotentorial surgical approach to the skull was made and mirror-image, 2 mm diameter parieto-occipital burr-hole craniectomy defects were created in the right and left aspects of the skull of each rat using a high-speed electric drill. These defects were created at the following stereotactic locations relative to the bregma: 5 mm posterior (caudal) and 3 mm lateral. The exposed dura was punctured with hypodermic needle, and the FMDs were then advanced to a depth of 1.5 mm beneath the surface of dura of each craniectomy defect using the manipulator arm of the stereotactic frame (Table 5).

6.2.3 Fiberotpic Microneedle Device-Convection Enhanced Delivery (FMD-CED) Procedure

A total of 30 cerebral hemispheres from 15 rats were treated, as the brain from each rat underwent bilateral CED infusion with a liposomal rhodamine (LR) solution (DOPC/CHOL/mPEG2000-DSPE liposomes labeled with rhodamine DHPE; FormuMax Scientific, Palo Alto, CA, USA), or a gadolinium-Evans blue-albumin complex solution (Gd-EBA) co-delivered with the FMD parameters described in Table 5. Laser power values for co-delivery were 100 or 200 mW emitted from a 1064 nm, continuous wave fiber laser (IPG Photonics, Oxford, MA). The average irradiance corresponding to the power values of 100 and 200 mW was 1.3 and 2.6 W/mm^2, respectively. Average irradiance was calculated by dividing power by the surface area of the capillary tube's annular beveled tip (45°). In individual rats, the infusate solution used during CED was kept consistent between both cerebral hemispheres, and every rat (except the control) had one hemisphere treated with laser and fluid co-delivery (FMD-CED+laser), and one hemisphere with fluid delivery alone (FMD-CED only).

A single rat served as an untreated control, which underwent sham FMD placement without infusion in the left cerebral hemisphere, and no insertion in the right cerebral hemisphere. The Gd-EBA solution was prepared by diluting a stock solution of 25 mg/ml Gd-albumin (Galbumin, BioPAL Inc., Worcester, MA, USA), containing 10-15 Gd-DTPA per albumin molecule and a molecular weight of 74 kDa, with deionized water to a concentration of 10 mg/ml. The Gd-albumin was then mixed with Evans blue (1 mg Evans blue [Sigma, St. Louis, MO, USA] per 2 ml Gd-albumin) to make the tagged Gd-EBA complex.

All CED infusates were delivered at a rate of 0.1 µl/min for a total of 60 minutes using a multichannel, microinfusion syringe pump (PhD Ultra, Harvard Apparatus, Holliston, MA, USA). The pump was started at least 1 hour prior to infusion and continued through withdrawal of the needle from the brain after the 1 hour experimental infusion to help prevent clogging and aid in identifying infusion issues using the infusion line pressure monitoring. CED infusion line pressure was monitored at a sample frequency of 2 Hz by wet/wet differential pressure sensors (PX26-005DV, Omega Engineering, Inc., Stamford, CT) connected to a data acquisition unit (OM-DAQ-USB-2401, Omega Engineering, Inc., Stamford, CT). The pressure sensors were attached to a 3-way T-valve connecting the syringe pump to the infusate line. Pressure monitoring was begun at least 5 minutes prior to initiating the infusion and continued until at least 10 minutes after infusion had ceased.

Table 5: FMD-CED treatment matrix

Treatment	No. Hemispheres Treated
Gd-EBA Only	8
Gd-EBA + 100 mW	6
Gd-EBA + 200 mW	2
LR Only	7
LR + 100 mW	4
LR + 200 mW	3
Total N-number	**30**

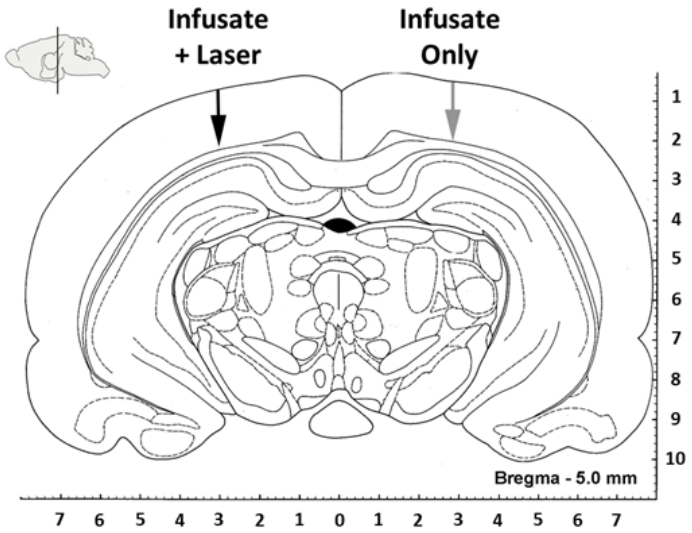

Table 1- Legend
GD-EBA= Gadolinium-Evans blue- albumin complex solution
LR= Liposomal rhodamine
Arrows indicate the insertions of the FMD in each hemisphere

Following completion of the infusions, the FMDs were withdrawn from the brain, and the rats euthanatized by intraperitoneal injection of 1 mL of phenytoin-pentobarbital solution (Beuthanasia-D, Abbott Laboratories, Abbott Park, IL) followed by rapid cervical dislocation. The brains were harvested, examined for evidence of external reflux of infusate or superficial damage to the cerebral cortex, and processed as described below.

6.2.4 Post-Infusion Magnetic Resonance Imaging (MRI)

Two rats infused with Gd-EBA and treated with 100 mW FMD-CED underwent *in situ* MRI examination of the brain immediately following euthanasia using a 1.5 Tesla superconducting magnet (Philips Integra, Philips Healthcare, Andover, MA) with an 8-channel volume head coil. T1-weighted images were obtained in 3 planes using a spin echo sequence (Echo time [TE]=15 ms, Repetition time [TR] = 410 ms, 2 mm slice thickness with 0.5 mm spacing, 224 x 224 mm field of view (FOV), and 256 x 256 mm matrix), and a high-resolution multiplanar three-dimensional gradient echo sequence (TE= 4.4 ms, TR= 25 ms, 1.5 mm slice thickness with no gap, 128 x 128 mm FOV, and 256 x 256 mm matrix).

6.2.5 FMD-CED Volume of Distribution Quantification and Brain Pathology

A transverse brain segment extending from the bregma to the rostral cerebellum containing both treated cerebral hemispheres was harvested, embedded in a cryomold containing cryomedia (OCT; Ted Pella, Redding, CA, USA), flash frozen in liquid nitrogen and stored at -80 °C until analysis. Tissue was serially sectioned in the transverse plane at 10 μm thickness and 200 μm intervals. The positions of the transverse sections at which the Gd-EBA or LR were first and last

visible (the anterior/rostral and posterior/caudal limits of the z-plane of the CED infusion) were recorded. Digital photomicrographs (Nikon Eclipse Ni-E, Nikon, Japan) of the fluorescent volume from rhodamine-containing liposomes or Evans blue were obtained from all intervening transverse sections using a charged-coupled device camera with a fixed aperture (Nikon DS-Fi1c, Nikon, Japan) and an ultraviolet light source. The volume of fluorescent infusate distribution (V_d) resulting from the transverse image stack from each rat was calculated using the volumetric algorithm on a commercial image analysis system (Stereo Investigator; MBF Bioscience, Williston, VT, USA).

Sections of 5 μm thickness were also trimmed from each transverse brain interval, stained with hematoxylin and eosin and examined by light microscopy for morphologic evidence of thermal or mechanical damage to the brain resulting from the FMD co-delivery treatments.

6.2.6 Statistical Analysis

A mixed model ANOVA procedure was used to evaluate the effects of laser co-delivery (laser on or laser off [treated control]), laser power (100 mW vs. 200 mW), and infusion agent (LR and Gd-EBA) on the V_d of infusates. Statistical analyses were performed using commercial software (SAS, version 9.0, Cary, NC, USA) and $\alpha = 0.05$.

6.3 Results

6.3.1 FMD-CED Procedure

Data from 22 cerebral hemispheres were included in statistical analyses of V_d. The intended targeted regions of both cerebral hemispheres were successfully infused in 10/15 of rats. In 3/15 rats (one each for Gd-EBA + 200 mW, LR + 100 mW, and LR + 200 mW) the data from both hemispheres was excluded due to significant leakage of infusate outside of the targeted region of brain parenchyma into the ventricular system or subarachnoid space. In one rat, one hemisphere (Gd-EBA only) was excluded due to mechanical damage to the FMD prior to insertion into the brain that precluded delivery of infusate. In an additional rat, one hemisphere (LR = 200 mW) was excluded due to reflux of the majority of the delivered infusate volume up the FMD insertion track to the surface of the brain.

6.3.2 Qualitative and Quantitative Analyses of FMD-CED

Brain regions infused with LR and Gd-EBA through the FMD were clearly and sharply demarcated from untreated regions on MR imaging and pathological analyses (Figures 40-42). Qualitatively, the V_d of LR and Gd-EBA appeared larger in cerebral hemispheres treated with co-delivery based on pathological (Figures 40A, 42A-3C) and MRI (Figure 41) examinations. Quantitatively, co-delivery was associated with significantly increased V_d compared to controls (Figure 40B), with measured volumes of dispersal of 15.8±0.6 mm^3 and 10.01±0.4 mm^3 for 100 mW co-delivery and its symmetric hemisphere fluid only controls, respectively. The V_d for 200 mW co-delivery and its symmetric hemisphere fluid only controls were measured at 18.0±0.3 mm^3 and 10.3±0.7 mm^3, respectively (Figure 40B). Higher laser power (200 mW) was

associated with a significant and positive effect on infusate V_d (Figure 40B). There were no significant differences in V_d between infusions performed with Gd-EBA or LR (p=0.7912).

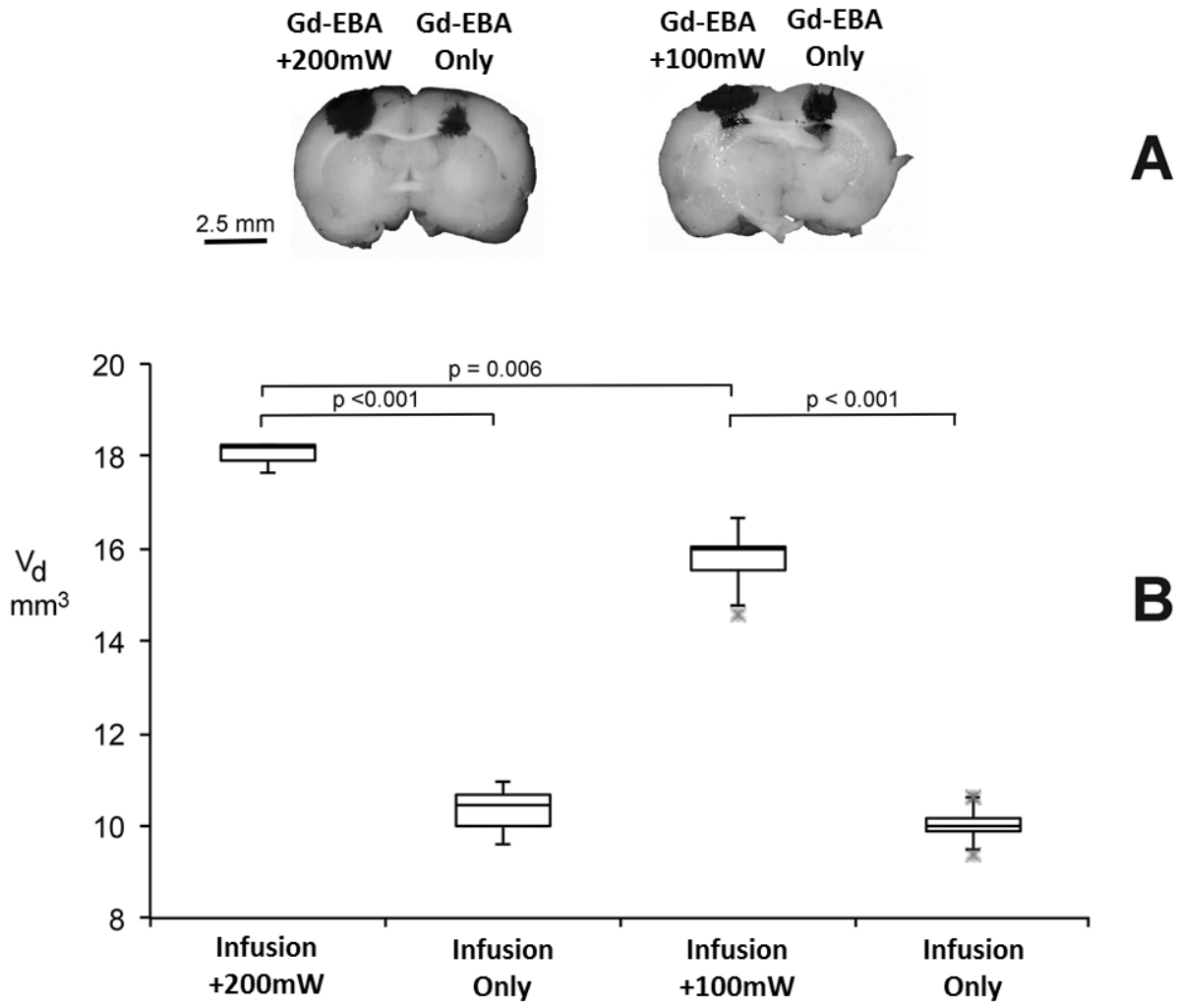

Figure 40: The effects of FMD-CED laser co-delivery on infusate Vd demonstrated with gross brain specimens (A) and quantitative analyses (B). Cerebral hemispheres receiving co-delivery have significantly larger Vd compared to controls, and increasing laser co-delivery power was associated with a significant increase in the Vd.

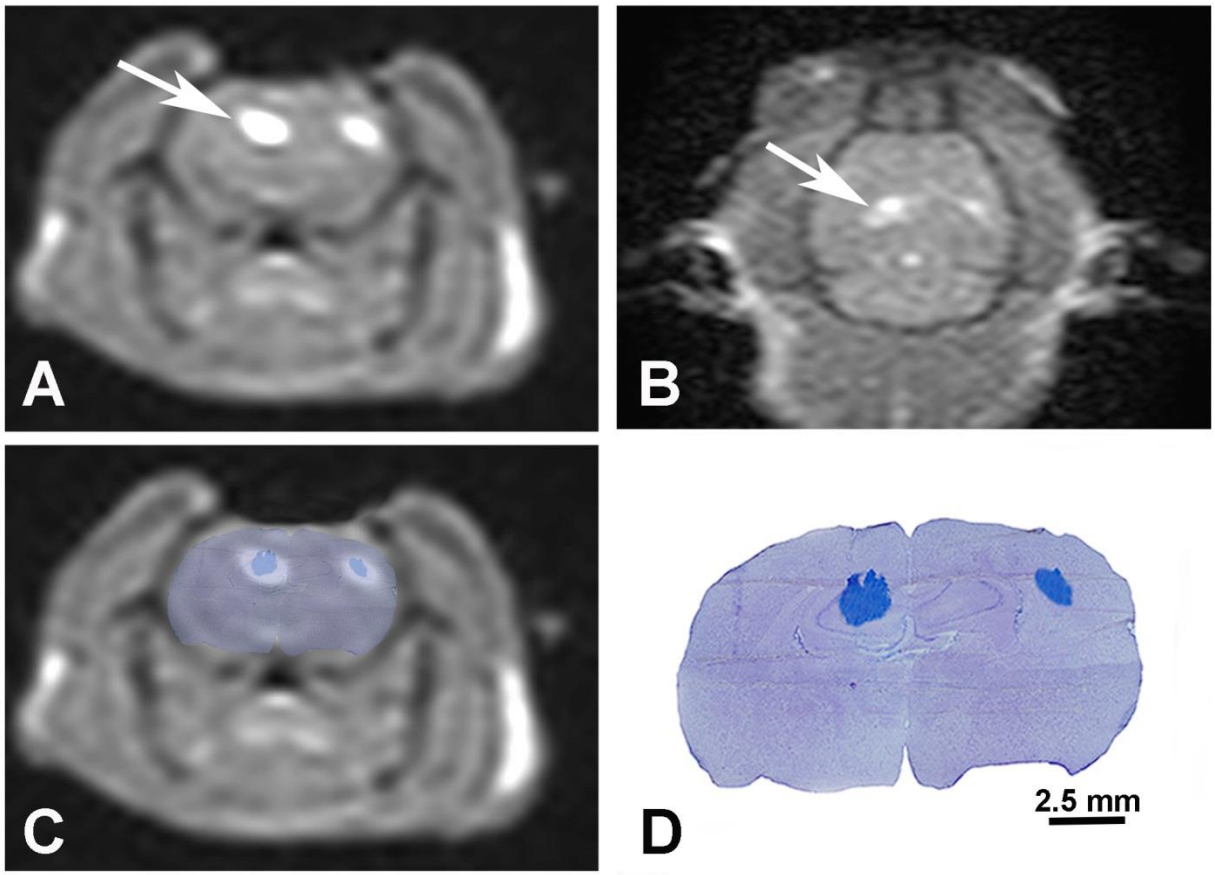

Figure 41: Immediate post-mortem transverse (A, C), and dorsal planar (B) T1-weighted MRI images and corresponding pathological brain slice preparation (C, D) of rat brain infused with Gd-EBA by FMD-CED illustrating greater infusate distribution associated with co-delivery of 100 mW laser energy (arrows) compared to infusion-only control (contralateral hemisphere). The fusion panel (C) demonstrates correlation of infusate distributions between MRI and pathological images.

6.3.3 Brain Pathology

No significant changes were seen in the untreated cerebral hemisphere (Figure 42A). The sham FMD treatment resulted in physical displacement of neuropil along the trajectory of needle insertion, which was also associated with minimal hemorrhage (Figure 42D). Minimal histopathologic changes (described below) were present in control hemispheres and those

subjected to 100 mW FMD co-delivery. Small foci of malacia, measuring up to 500 x 500 μm, were present in regions of the brain located at the tips of the FMD, and microvascular hemorrhage was noted along the insertion trajectories of some FMD devices (Figure 42D and 42E). Control and 100 mW FMD treatments were associated with neuronal pyknosis and vacuolization of the brain tissue immediately adjacent to needle insertion tracks, with morphologically normal brain tissue being present within 250 μm of FMD insertions (Figure 42D and 42E). The laminar cytoarchitecture of the cerebral cortex and hippocampus was preserved in the sham (Figure 42D, 42G, and 42J), FMD only, and 100 mW co-delivery treated cerebral hemispheres (Figure 42E, 42H, and 42K). Cerebral cortices treated with 200 mW co-delivery displayed evidence of thermal-induced brain injury (protein coagulation, hyperchromasia, and fragmentation) which resulted in significant disruption of the brain's morphology, including more extensive malacia at the needle tips (Figure 42F), as well as microcavitation and necrosis (Figure 42F, 42I, and 42L) of the brain tissue in infused regions.

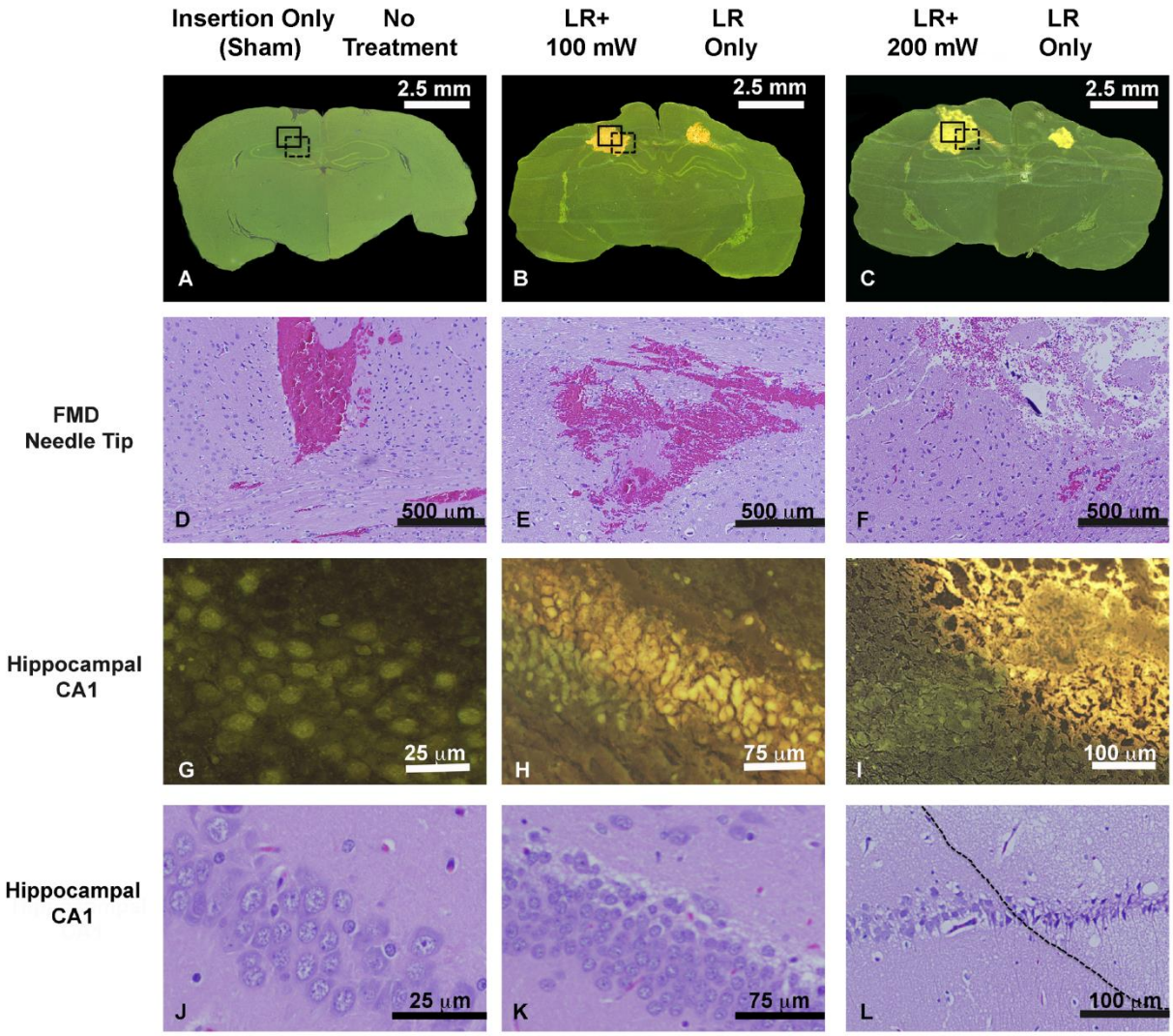

Figure 42: Pathology of rat brains infused with LR. Subgross fluorescent brain slice preparations (A-C) demonstrating larger LR distributions (yellow-gold regions) associated with laser co-delivery (B and C) compared to infusion only and an untreated control (A). Morphologic changes in the brain at the level of the FMD needle tips in sham (D; solid inset A), 100 mW co-delivery (E; solid inset B) and 200 mW co-delivery (F; solid inset C) treated cerebral hemispheres. Compared to the sham and 100 mW co-delivery regions, there is prominent malacia induced by the 200 mW treatment. Fluorescent (G-I) and corresponding brightfield (J-L, H&E stain) microscopic morphology of hippocampal CA1 regions at the periphery of infusions in untreated control (G and

J; dashed inset A), 100 mW co-delivery (H and K; dashed inset B), and 200 mW co-delivery infused brains (I and L; dashed inset C). In the 100 mW co-delivery treated brain, LR is visible in the interstitial and intracellular compartments (H) and is not associated with significant changes in cytoarchitecture (K). In the 200 mW co-delivery treatment (I and L), hippocampal damage is most prominent in the infused region (L, right of dashed line) and consists of polymicrocavitation and hippocampal neuronal pyknosis.

6.3.4 Line Pressure Monitoring

The pressure behavior in the infusions used in the statistical analyses exhibited an approximately linear increase throughout the procedure, indicating steady-state pressure was not reached during the one hour infusion timeframe at a flow rate of 0.1 μL/min. The rate of pressure increase varied greatly between infusions. A representative pressure graph during infusion is shown in Figure 43.

6.4 Discussion

This study was conducted to determine if laser co-delivery during infusion would significantly increase the V_d of an infusate over a one-hour infusion timeframe. Quantitative analysis of co-delivery versus fluid infusion alone was conducted through post-infusion MR and histopathological analysis of infused *in vivo* rodent cerebral tissue. Through these means, co-delivery was demonstrated to significantly increase V_d, with greater enhancement associated with 200 mW co-delivery over 100 mW. However, the 200 mW laser power was also associated with thermal damage to the brain tissue. As negligible tissue damage occurred with the 100 mW co-delivery, enhanced V_d was shown to be an effect decoupled from thermal damage, suggesting

that a sub-lethal, temperature-based phenomenon can be attributed for the observed increase in V_d.

The thermal damage associated with the 200 mW co-delivery was minimal and entirely localized to the region of highest energy density at the FMD tip. Previous groups have demonstrated that sustained temperatures of 45 °C will cause coagulative necrosis in normal brain tissue, while most agree that the threshold for irreversible damage over long exposure is between 42 and 43 °C [121, 137-139] The minimal thermal damage at the higher irradiance (2.6 W/mm^2) used in this study is to be expected from similar experiments in the literature and previous work by this group [140]. Schatz *et al.* conducted a similar study on thermal lesion size in normal rabbit brains, with irradiances ranging from 4.0-23.8 W/mm^2. The group utilized a bare fiber with a 400 µm core inserted transdurally to a depth of 8 mm within the cerebrum and created thermal lesions 2-10 mm in diameter. In a recent paper, our group demonstrated that irradiances of 2.6 W/mm^2 (without fluid delivery) was associated with a small volume (<1 mm) of thermal damage surrounding the FMD tip. It remains an important observation that the thermal damage response in this rat model remained independent of whether room temperature fluid was being co-delivered, although the experiment should be repeated at higher flow rates in larger animal models to ensure the finding is consistent at CED relevant treatment parameters.

Volumetric dispersal was shown to increase with laser co-delivery during infusion independent of which of the two infusates was employed. The authors can only speculate on contributing mechanisms involved in causing the increased V_d. Fluid and mass transport in biological tissues occur by multiple simultaneous pathways, and each are known to have temperature dependence.

Such pathways include both passive and active transport across cells membranes, interstitial flow between cells, and blood perfusion [135, 141-143]. Increasing temperature also reduces fluid viscosity, enhancing extracellular dispersal [134]. Ogura *et al.* demonstrated that local hyperthermia has been shown to exhibit a biphasic response from intracerebral arterioles, as hyperthermia causes vasoconstriction within the first 3 minutes, but subsequently the vessels dilate to a state of greater than initial diameter by 15 minutes [135]. This behavior would cause increased interstitial thermal and fluid transport after the initial response. In thermochemotherapy, heating fluid-based chemotherapeutics has been shown to increase penetration depth into target tissues and tumor masses [144]. Bischoff *et al.* demonstrated that hyperthermic temperatures above 40 ºC have been shown to enhance cell membrane permeability *in vitro* [145]. As the brain is highly cellular, it is possible that sub-lethal thermal permeabilization of cell membranes allows molecular transport intra- and inter-cellularly, which would act as an increase in net tissue porosity. Contributing factors of multifarious influence are almost certainly influencing the hyperthermic effect of laser co-delivery.

Volumetric dispersal was also shown to increase with increasing laser power, as the 200 mW co-delivery had a greater effect on $V_{d.}$ This may provide an indication on the mechanisms contributing to the hyperthermic effect, but can also be for more obvious reasons. One explanation for the greater enhancement would be the larger tissue volume brought into a state of sub-lethal hyperthermia by the higher irradiance. A previous paper by this group described laser powers greater than 200 mW causing thermal coagulation of increasingly larger tissue volumes, indicating increased thermal elevation volume despite mitigating factors such as the heat sink behavior of the local vasculature [105]. In light of the thermal damage observed, any

hyperthermic effect may have increased in the tissue proximal to the FMD tip, allowing greater transport rates. Overall, these experiments have demonstrated that sub-lethal photothermal heating during infusion can shorten infusion timeframes for dispersing fluid throughout a given volume.

In the uncompromised CED infusions performed, line pressure steadily increased throughout the duration of the infusion. It should be noted that, possibly due to factors including low flow rate, compliance in the fluid lines, and relatively short infusion period, steady-state pressure was not achieved. Pressure monitoring also allowed for real-time identification of adverse events associated with CED. For example, in three infusions, correlation between breakthrough of the infusate into a nearby ventricle and a large pressure drop followed by a plateau lasting the remainder of the infusion. A similarly detectable event was clogging of the FMDs. Monitoring the line pressure of a CED infusion may allow detection of these clogs and may enable feedback during attempts to ameliorate the problem by modulating needle depth or pump flow rate. Both ventricular leakage and clogging have been identified as complications of CED in the brain [47]. These results corroborate findings made by other groups, suggesting that utilization of real-time monitoring through line pressure measurement or MRI-tracking can provide superior feedback and control of CED infusions and may allow the avoidance of adverse events entirely through enabling clinicians to anticipate and counteract potential obstacles [47, 146, 147].

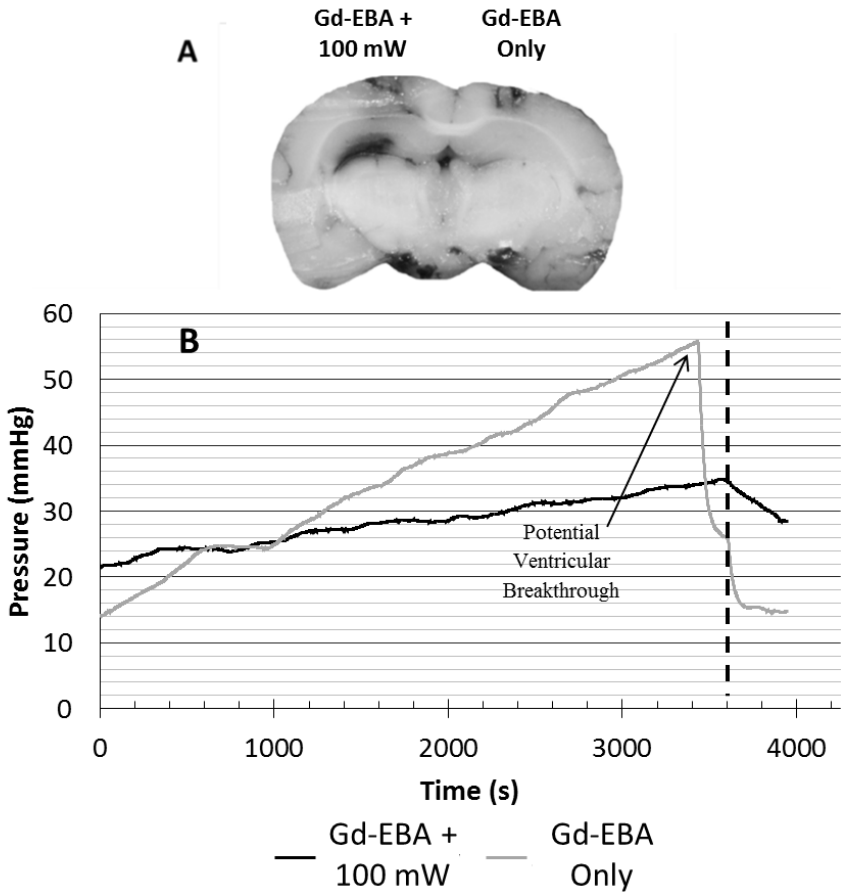

Figure 43: A) Gross section exhibiting a ventricular breakthrough. B) Pressure vs. time plot for infusion into gross section showing a waveform suggestive of ventricular leakage for the fluid only curve. The dotted line denotes FMD withdraw from the brain. Leakage of infusate into the ventricles on the Gd-EBA only hemisphere resulted in a lack of infusate in the brain parenchyma compared to the Gd-EBA+100 mW hemisphere. Note that the pump continued after FMD withdraw.

This study was the first to demonstrate how laser co-delivery can be used to increase V_d in a normal brain rodent model. However, the rat brain model used in this study has several limitations. The first is the difference in relative geometry between larger mammals. The FMDs employed are very similar to what the authors envision using in large animal models and

humans, but the relative amount of brain volume disturbed by the microneedle involved would be greatly diminished. Additionally, the relative distance between different structures may make some problems encountered, such as ventricular leakage, less likely in a larger model. One of the few concessions made to the model's brain size was the flow rate, which was set 1-2 orders of magnitude below the infusion rates normally used for CED in humans [110]. Chen *et al.* stated that the flow rate of 0.1 µL/min is associated with substantially less reflux than more clinically relevant flow rates of 1-5 µL/min [115]. High amounts of fluid reflux might carry heat away from the target region, lessening the thermal effect laser co-delivery provides at these power values. Another factor to consider in this study was that infusion was conducted in healthy animals. CED has been investigated for treating malignant gliomas, which have been shown to have a profound and largely unpredictable effect on macromolecule transport. Solid tumors tend to be associated with high local fluid pressure, necrotic tissue, and leaky vasculature, which could all have significant impact on the effects of laser co-delivery [148]. Future experiments conducted with larger models afflicted with different disease states would enable greater insight into the utility of sub-lethal hyperthermia demonstrated in this study.

6.5 Conclusion

This study investigated whether concurrent delivery of photothermal heating during infusion would significantly enhance fluid dispersal in brain tissue. FMDs were inserted symmetrically into either hemisphere of healthy rodents, one device co-delivered fluids and laser energy while the other infused fluid only. Analyses of serial sections and post-infusion MRIs demonstrated that dispersal volume increased with increasing laser power, with measured volumes of 15.8±0.6 mm^3 for 100 mW compared to 10.0±0.4 mm^3 for its fluid only control and and 18.0±0.3 mm^3 for

200 mW compared to 10.3±0.7 mm^3 for its fluid only control. This finding indicated that laser co-delivery during CED procedures significantly increases volumetric dispersal rate and could shorten infusion timeframes. Future work evaluating photothermal augmentation of fluid dispersal in brain tumor models is ongoing.

Chapter 7: Conclusions and Future Work

This dissertation provides the most complete review of the FMD technology's development to date. After briefly reviewing early studies focused on optimizing multimode fiberoptic-based FMD designs for skin penetration and control of light delivery profiles, the bulk of the manuscript provides a thorough description of work developing FMDs based on silica capillary tubes. Learning from early experiments with the unpredictable resistances provided by melt-drawn tips, later designs incorporated an angle-polished, sharp, bevel tip, whose hydraulic resistance closely resembles that of a flat-cleaved tube. The ease and mechanical reliability of the beveled tip design led to its deployment in initial experiments seeking to modify the FMD for treating bladder and brain cancers.

To begin working towards the therapeutic strategy of shaping a photothermal insult through infusing exogenous chromophores, a set of experiments characterizing SWNH solution dispersal and photothermal response to irradiation with a 1064 nm laser were conducted. The nanohorns were demonstrated to quickly spread through a clinically relevant footprint analogous to that of an invasive urothelial cell carcinoma. Exterior irradiation with a 1064 nm laser quickly heated SWNH perfused tissue to a quasi-steady state temperature approximately an order of magnitude higher than identical non-SWNH perfused tissue. Further experiments exhibited the first successful simultaneous co-delivery through a single, light-guiding capillary tube. These results demonstrated the FMD's potential as a new tool to combat urothelial cell carcinomas.

Convection-enhanced delivery (CED) was the next target application for the FMD. Initial experiments sought to demonstrate an increase in volumetric dispersal rate mediated by low-

level amounts of local hyperthermia. As the co-delivery couple allowing simultaneous co-delivery through a single capillary tube had not reached a sufficiently robust stage, the experiments were conducted with a multimode fiberoptic adhered to a standard capillary. The Agarose offered unforeseen complications through reflux and clogging, which were sufficiently circumvented through a rapid manual translation method that offered reduced lateral motion during insertion. Dual delivery of laser energy during infusion was demonstrated to increase volumetric dispersal. To enhance mechanistic understanding of this effect, a secondary set of experiments were conducted with a set of infusions into isothermal volumes of Agarose at different temperatures. A poroelastic model developed by Chen *et al.* through similar experiments in Agarose was applied to our data. Through use of Chen *et al.*'s empirically-derived constants and our experimental volume dispersal data, values for the dilatation coefficient, a product of the Darcy permeability and the sum of the compressibility and rigidity moduli, were found. As disambiguating the temperature dependence of the different factors contributing to dilatation coefficient was impossible, the lumped dilatation coefficient itself was plotted as a function of temperature and an empirical equation describing the relationship was determined. Further tests are needed to determine if this equation will describe temperatures outside the experimental range or for the *in vivo* case, but the general procedure and mathematical process should be conserved. This data demonstrated proof of the photothermal augmentation hypothesis, which motivated a follow-up study with an *in vivo* model.

Two sequential experiments were conducted to first determine the correct laser and fluid parameters for the FMD treatment approach and then fully test the hypothesis of sub-lethal photothermal heating. Preliminary experiments with *ex vivo* brain tissue were finished to select

an initial range of laser powers. Irradiation through an interstitially positioned FMD at a range of powers determined the threshold for photothermal damage after 1 hour of irradiation was between 100 and 200 mW. The subsequent study used these limits to both verify the previous experiment and show both a lethal and sub-lethal photothermal response. Volumetric dispersal was shown to markedly increase with increasing wattage, but the 200 mW irradiance again demonstrated slight photothermal damage in histopathological analysis. However, the 100 mW irradiance was correlated with a substantial increase in volumetric dispersal over the fluid only control, validating the hypothesis of photothermal augmentation improving interstitial dispersal rate for CED.

Future steps for the FMD technology platform include testing the different applications of light and fluid delivery on vaccines, cosmetic procedures, and optogenetics. Within the applications described in this manuscript, treatments of live canine veterinary patients with naturally occurring forms of the described brain and bladder cancers will be the next steps. Slight alterations to the described procedures such as delivering a photochemical agent for photodynamic therapy could also be tested. Design improvements to minimize traditional infusion problems such as reflux and tissue clogging could be implemented, such as the step-down catheters developed by Krauze *et al.* The FMD platform has possibilities to improve or modify any treatment or diagnostic procedure in medical science that uses a high aspect ratio needle or catheter, so there is great potential for the co-delivery aspect to fundamentally improve one or more such application.

References Cited

1. **Kaushik, S., et al., *Lack of pain associated with microfabricated microneedles.* Anesth Analg, 2001. 92(2): p. 502-4.**
2. **Gill, H.S., et al., *Effect of microneedle design on pain in human volunteers.* Clin J Pain, 2008. 24(7): p. 585-94.**
3. **Gill, H.S. and M.R. Prausnitz, *Does needle size matter?* J Diabetes Sci Technol, 2007. 1(5): p. 725-9.**
4. **Cormier, M., et al., *Transdermal delivery of desmopressin using a coated microneedle array patch system.* J Control Release, 2004. 97(3): p. 503-11.**
5. **Liu, R., X. Wang, and Z. Zhou, *[Application of MEMS microneedles array in biomedicine].* Journal of Biomedical Engineering, 2004. 21(3): p. 482-5.**
6. **Mukerjee, E.V., et al., *Microneedle array for measuring wound generated electric fields.* Conf Proc IEEE Eng Med Biol Soc, 2006. 1: p. 4326-8.**
7. **Yan, K., H. Todo, and K. Sugibayashi, *Transdermal drug delivery by in-skin electroporation using a microneedle array.* Int J Pharm, 2010.**
8. **Jiang, J., et al., *Intrascleral drug delivery to the eye using hollow microneedles.* Pharmaceutical Research, 2009. 26(2): p. 395-403.**
9. **Prausnitz, M.R., et al., *Microneedle-based vaccines.* Curr Top Microbiol Immunol, 2009. 333: p. 369-93.**
10. **Park, J.H., M.G. Allen, and M.R. Prausnitz, *Polymer microneedles for controlled-release drug delivery.* Pharmaceutical Research, 2006. 23(5): p. 1008-19.**
11. **Park, J.H., M.G. Allen, and M.R. Prausnitz, *Biodegradable polymer microneedles: fabrication, mechanics and transdermal drug delivery.* J Control Release, 2005. 104(1): p. 51-66.**
12. **Lee, J.W., J.H. Park, and M.R. Prausnitz, *Dissolving microneedles for transdermal drug delivery.* Biomaterials, 2008. 29(13): p. 2113-24.**
13. **Davis, S.P., et al., *Hollow metal microneedles for insulin delivery to diabetic rats.* IEEE Trans Biomed Eng, 2005. 52(5): p. 909-15.**
14. **Martanto, W., et al., *Transdermal delivery of insulin using microneedles in vivo.* Pharmaceutical Research, 2004. 21(6): p. 947-52.**
15. **Roxhed, N., et al., *Painless drug delivery through microneedle-based transdermal patches featuring active infusion.* IEEE Trans Biomed Eng, 2008. 55(3): p. 1063-71.**
16. **Kosoglu, M.A., et al., *Fiber Optic Microneedles for Transdermal Light Delivery: Ex Vivo Porcine Skin Penetration Experiments.* Journal of Biomechanical Engineering-Transactions of the Asme, 2010. 132(9).**
17. **Chen, W.-F. and E.M. Lui, *Structural stability : theory and implementation*. 1987, New York: Elsevier. xvii, 490 p.**
18. **Kosoglu, M.A., et al., *Fiberoptic microneedles: novel optical diffusers for interstitial delivery of therapeutic light.* Lasers Surg Med, 2011. 43(9): p. 914-20.**
19. **Kosoglu, M.A., R.L. Hood, and C.G. Rylander, *Mechanical strengthening of fiberoptic microneedles using an elastomeric support.* Lasers in Surgery and Medicine, 2012. 44(5): p. 421-428.**

20. **Vandergrift, W.A., et al., *Convection-enhanced delivery of immunotoxins and radioisotopes for treatment of malignant gliomas.* Neurosurg Focus, 2006. 20(4): p. E13.**
21. **Quek, M.L., et al., *Prognostic significance of lymphovascular invasion of bladder cancer treated with radical cystectomy.* J Urol, 2005. 174(1): p. 103-6.**
22. **Wong-You-Cheong, J.J., et al., *From the archives of the AFIP - Neoplasms of the urinary bladder: Radiologic-pathologic correlation.* Radiographics, 2006. 26(2): p. 553-U17.**
23. **Sampson, J.H., et al., *Poor drug distribution as a possible explanation for the results of the PRECISE trial.* Journal of Neurosurgery, 2010. 113(2): p. 301-9.**
24. **Rodel, C., et al., *Combined-modality treatment and selective organ preservation in invasive bladder cancer: Long-term results.* Journal of Clinical Oncology, 2002. 20(14): p. 3061-3071.**
25. ***Bladder Cancer Treatment*. 2009 8/21/2009 [cited 2010; Available from: http://www.cancer.gov/cancertopics/pdq/treatment/bladder/Patient/page4.**
26. **Thrasher, J.B. and E.D. Crawford, *Current management of invasive and metastatic transitional cell carcinoma of the bladder.* J Urol, 1993. 149(5): p. 957-72.**
27. **Hart, S., et al., *Quality of life after radical cystectomy for bladder cancer in patients with an ileal conduit, cutaneous or urethral kock pouch.* The Journal of urology, 1999. 162(1): p. 77-81.**
28. **Stein, J.P., et al., *Radical cystectomy in the treatment of invasive bladder cancer: long-term results in 1,054 patients.* Journal of clinical oncology : official journal of the American Society of Clinical Oncology, 2001. 19(3): p. 666-75.**
29. **Syed, H.A., et al., *Holmium : YAG laser treatment of recurrent superficial bladder carcinoma: Initial clinical experience.* Journal of Endourology, 2001. 15(6): p. 625-627.**
30. **Larizgoitia, I. and J.M.V. Pons, *A systematic review of the clinical efficacy and effectiveness of the holmium : YAG laser in urology.* Bju International, 1999. 84(1): p. 1-9.**
31. **Soler-Martinez, J., et al., *Holmium laser treatment for low grade, low stage, Noninvasive bladder cancer with local anesthesia and early instillation of mitomycin C.* Journal of Urology, 2007. 178(6): p. 2337-2339.**
32. **Pietrow, P.K. and J.A. Smith, Jr., *Laser treatment for invasive and noninvasive carcinoma of the bladder.* Journal of endourology / Endourological Society, 2001. 15(4): p. 415-8; discussion 425-6.**
33. **Hruby, G.W., et al., *Transurethral bladder cryoablation in the porcine model.* Journal of Urology, 2008. 179(4): p. 365-365.**
34. **Sternberg, C.N., et al., *Chemotherapy for bladder cancer: treatment guidelines for neoadjuvant chemotherapy, bladder preservation, adjuvant chemotherapy, and metastatic cancer.* Urology, 2007. 69(1 Suppl): p. 62-79.**
35. **Malkowicz, S.B., et al., *Muscle-invasive urothelial carcinoma of the bladder.* Urology, 2007. 69(1 Suppl): p. 3-16.**
36. **Fedeli, U., S.A. Fedewa, and E.M. Ward, *Treatment of muscle invasive bladder cancer: evidence from the National Cancer Database, 2003 to 2007.* The Journal of urology, 2011. 185(1): p. 72-8.**

37. Kramer, M.W., et al., *Current evidence for transurethral laser therapy of non-muscle invasive bladder cancer.* World J Urol, 2011.
38. Johnson, D.E., *Use of the Holmium-Yag (Ho Yag) Laser for Treatment of Superficial Bladder-Carcinoma.* Lasers in Surgery and Medicine, 1994. 14(3): p. 213-218.
39. Kramer, M.W., et al., *Current evidence for transurethral laser therapy of non-muscle invasive bladder cancer.* World journal of urology, 2011.
40. Das, A., P. Gilling, and M. Fraundorfer, *Holmium laser resection of bladder tumors (HoLRBT).* Techniques in urology, 1998. 4(1): p. 12-4.
41. Ghoneim, M.A., et al., *Radical cystectomy for carcinoma of the bladder: critical evaluation of the results in 1,026 cases.* The Journal of urology, 1997. 158(2): p. 393-9.
42. Nishikawa, R., *Standard Therapy for Glioblastoma-A Review of Where We Are.* Neurologia Medico-Chirurgica, 2010. 50(9): p. 713-719.
43. Stupp, R., et al., *Effects of radiotherapy with concomitant and adjuvant temozolomide versus radiotherapy alone on survival in glioblastoma in a randomised phase III study: 5-year analysis of the EORTC-NCIC trial.* Lancet Oncol, 2009. 10(5): p. 459-66.
44. Walker, M.D., et al., *Randomized comparisons of radiotherapy and nitrosoureas for the treatment of malignant glioma after surgery.* N Engl J Med, 1980. 303(23): p. 1323-9.
45. Nishikawa, R., *Standard therapy for glioblastoma--a review of where we are.* Neurol Med Chir (Tokyo), 2010. 50(9): p. 713-9.
46. Laske, D.W., R.J. Youle, and E.H. Oldfield, *Tumor regression with regional distribution of the targeted toxin TF-CRM107 in patients with malignant brain tumors.* Nat Med, 1997. 3(12): p. 1362-8.
47. Bobo, R.H., et al., *Convection-enhanced delivery of macromolecules in the brain.* Proc Natl Acad Sci U S A, 1994. 91(6): p. 2076-80.
48. Vazquez, L.C., et al., *Polymer-coated cannulas for the reduction of backflow during intraparenchymal infusions.* J Mater Sci Mater Med, 2012. 23(8): p. 2037-46.
49. Gill, S.S., et al., *Direct brain infusion of glial cell line-derived neurotrophic factor in Parkinson disease.* Nat Med, 2003. 9(5): p. 589-95.
50. Rogawski, M.A., *Convection-enhanced delivery in the treatment of epilepsy.* Neurotherapeutics, 2009. 6(2): p. 344-51.
51. Sampson, J.H., et al., *Intracerebral infusate distribution by convection-enhanced delivery in humans with malignant gliomas: descriptive effects of target anatomy and catheter positioning.* Neurosurgery, 2007. 60(2 Suppl 1): p. ONS89-98; discussion ONS98-9.
52. Kanner, A.A., *Convection-Enhanced Delivery High-Grade Gliomas*, G.H. Barnett, Editor. 2007, Humana Press. p. 303-314.
53. Degen, J.W., et al., *Safety and efficacy of convection-enhanced delivery of gemcitabine or carboplatin in a malignant glioma model in rats.* Journal of Neurosurgery, 2003. 99(5): p. 893-898.
54. Mardor, Y., et al., *Convection-Enhanced Drug Delivery of Interleukin-4 Pseudomonas Exotoxin (PRX321): Increased Distribution and Magnetic Resonance Monitoring.* Journal of Pharmacology and Experimental Therapeutics, 2009. 330(2): p. 520-525.

55. Ivanchenko, O. and V. Ivanchenko, *Designing and Testing of Backflow-Free Catheters.* Journal of Biomechanical Engineering-Transactions of the Asme, 2011. 133(6).
56. Saito, R., et al., *Distribution of liposomes into brain and rat brain tumor models by convection-enhanced delivery monitored with magnetic resonance imaging.* Cancer Research, 2004. 64(7): p. 2572-2579.
57. Krauze, M.T., et al., *Reflux-free cannula for convection-enhanced high-speed delivery of therapeutic agents - Technical note.* Journal of Neurosurgery, 2005. 103(5): p. 923-929.
58. Martanto, W., et al., *Mechanism of fluid infusion during microneedle insertion and retraction.* J Control Release, 2006. 112(3): p. 357-61.
59. Hamazoe, R., M. Maeta, and N. Kaibara, *Intraperitoneal thermochemotherapy for prevention of peritoneal recurrence of gastric cancer. Final results of a randomized controlled study.* Cancer, 1994. 73(8): p. 2048-52.
60. Liu, Y., et al., *Ultrasound-Induced hyperthermia increases cellular uptake and cytotoxicity of P-glycoprotein substrates in multi-drug resistant cells.* Pharm Res, 2001. 18(9): p. 1255-61.
61. Saad, A.H. and G.M. Hahn, *Ultrasound-Enhanced Effects of Adriamycin against Murine Tumors.* Ultrasound in Medicine and Biology, 1992. 18(8): p. 715-723.
62. Block, J.B., P.A. Harris, and A. Peale, *Preliminary Observations on Temperature-Enhanced Drug Uptake by Leukemic Leukocytes Invitro.* Cancer Chemotherapy Reports Part 1, 1975. 59(5): p. 985-988.
63. Nicholson, C., *Diffusion and related transport mechanisms in brain tissue.* Reports on Progress in Physics, 2001. 64(7): p. 815-884.
64. Linninger, A.A., et al., *Computational methods for predicting drug transport in anisotropic and heterogeneous brain tissue.* Journal of Biomechanics, 2008. 41(10): p. 2176-2187.
65. Chen, Z.J., et al., *A realistic brain tissue phantom for intraparenchymal infusion studies.* Journal of Neurosurgery, 2004. 101(2): p. 314-322.
66. Foley, C.P., et al., *Flexible microfluidic devices supported by biodegradable insertion scaffolds for convection-enhanced neural drug delivery.* Biomedical Microdevices, 2009. 11(4): p. 915-924.
67. Bettag, M., et al., *Stereotactic laser therapy in cerebral gliomas.* Acta Neurochir Suppl (Wien), 1991. 52: p. 81-3.
68. Carpentier, A., et al., *MR-guided laser-induced thermal therapy (LITT) for recurrent glioblastomas.* Lasers Surg Med, 2012. 44(5): p. 361-8.
69. Carpentier, A., et al., *Real-time magnetic resonance-guided laser thermal therapy for focal metastatic brain tumors.* Neurosurgery, 2008. 63(1 Suppl 1): p. ONS21-8; discussion ONS28-9.
70. Schwarzmaier, H.J., et al., *Treatment planning for MRI-guided laser-induced interstitial thermotherapy of brain tumors--the role of blood perfusion.* J Magn Reson Imaging, 1998. 8(1): p. 121-7.
71. Stafford, R.J., et al., *Laser-induced thermal therapy for tumor ablation.* Crit Rev Biomed Eng, 2010. 38(1): p. 79-100.

72. McDannold, N.J., et al., *Usefulness of MR imaging-derived thermometry and dosimetry in determining the threshold for tissue damage induced by thermal surgery in rabbits.* Radiology, 2000. 216(2): p. 517-23.
73. Jethwa, P.R., et al., *Treatment of a supratentorial primitive neuroectodermal tumor using magnetic resonance-guided laser-induced thermal therapy.* J Neurosurg Pediatr, 2011. 8(5): p. 468-75.
74. Jethwa, P.R., et al., *Magnetic resonance thermometry-guided laser-induced thermal therapy for intracranial neoplasms: initial experience.* Neurosurgery, 2012. 71(1 Suppl Operative): p. ons133-45.
75. Schwabe, B., et al., *Laser-induced thermal lesions in the human brain: short- and long-term appearance on MRI.* J Comput Assist Tomogr, 1997. 21(5): p. 818-25.
76. Kosoglu, M., et al., *Fiberoptic Microneedles for Transdermal Light Delivery: Ex Vivo Porcine Skin Penetration Experiments.* Journal of Biomechanical Engineering, 2010. 132(9): p. 091014.
77. Ramasubramanian, M.K., O.M. Barham, and V. Swaminathan, *Mechanics of a mosquito bite with applications to microneedle design.* Bioinspir Biomim, 2008. 3(4): p. 046001.
78. Kirby, B., *Micro- and nanoscale fluid mechanics : transport in microfluidic devices*. 2010, New York: Cambridge University Press. xxiii, 512 p.
79. Munson, B.R. and T.H. Okiishi, *Fundamentals of fluid mechanics*. 6th ed. 2009, Hoboken, NJ: J. Wiley & Sons. 1 v. (various pagings).
80. Incropera, F.P., *Fundamentals of heat and mass transfer*. 6th ed. 2007, Hoboken, NJ: John Wiley. xxv, 997 p.
81. Zahn, J.D., et al., Biomedical Microdevices, 2000. 2(4): p. 295-303.
82. Sutterby, J., *Laminar Newtonian and Non-Newtonian Converging Flow in Conical Sections*, in *PhD Dissertation*1964, University of Wisconsin: Madison, WI.
83. Jarzebski, A.B. and W.L. Wilkinson, *Non-Isothermal Developing Flow of a Generalized Power-Law Fluid in a Tapered Tube.* Journal of Non-Newtonian Fluid Mechanics, 1981. 8(3-4): p. 239-248.
84. Phull, J.S., *Modern transurethral resection in the management of superficial bladder tumors.* British journal of medical & surgical urology, 2011. 4(3): p. 91.
85. Zhang, M., et al., *Fabrication of ZnPc/protein nanohorns for double photodynamic and hyperthermic cancer phototherapy.* Proc Natl Acad Sci U S A, 2008. 105(39): p. 14773-8.
86. Iijima, S., et al., *Nano-aggregates of single-walled graphitic carbon nano-horns.* Chemical Physics Letters, 1999. 309(3-4): p. 165-170.
87. Miyawaki, J., et al., *Toxicity of single-walled carbon nanohorns.* ACS nano, 2008. 2(2): p. 213-26.
88. Whitney, J.R., et al., *Single Walled Carbon Nanohorns as Photothermal Cancer Agents.* Lasers in Surgery and Medicine, 2011. 43(1): p. 43-51.
89. Murata, K., et al., *Molecular potential structures of heat-treated single-wall carbon nanohorn assemblies.* Journal of Physical Chemistry B, 2001. 105(42): p. 10210-10216.
90. Whitney, J., et al., *Carbon Nanohorns as Photothermal and Photochemical Laser Cancer Therapeutic Agents.* Lasers in Surgery and Medicine, 2009: p. 3-3.

91. Miyako, E., et al., *Near-infrared laser-triggered carbon nanohorns for selective elimination of microbes.* Nanotechnology, 2007. 18(47).
92. Cheng, M.D., et al., *Formation studies and controlled production of carbon nanohorns using continuous in situ characterization techniques.* Nanotechnology, 2007. 18(18).
93. Sarkar, S., et al., *Optical properties of breast tumor phantoms containing carbon nanotubes and nanohorns.* Journal of biomedical optics, 2011. 16(5): p. 051304.
94. Sarkar, S., et al., *Optical properties of breast tumor phantoms containing carbon nanotubes and nanohorns.* Journal of Biomedical Optics, 2011. 16(5).
95. Fisher, J.W., et al., *Photothermal response of human and murine cancer cells to multiwalled carbon nanotubes after laser irradiation.* Cancer Research, 2010. 70(23): p. 9855-64.
96. Burke, A., et al., *Long-term survival following a single treatment of kidney tumors with multiwalled carbon nanotubes and near-infrared radiation.* Proc Natl Acad Sci U S A, 2009. 106(31): p. 12897-902.
97. Whitney, J.R., et al., *Spatial and temporal measurements of temperature and cell viability in response to nanoparticle-mediated photothermal therapy.* Nanomedicine (Lond), 2012.
98. Morrison, P.F., et al., *Focal delivery during direct infusion to brain: role of flow rate, catheter diameter, and tissue mechanics.* The American journal of physiology, 1999. 277(4 Pt 2): p. R1218-29.
99. Dowlatshahi, K., et al., *Stereotactically guided laser therapy of occult breast tumors: work-in-progress report.* Archives of surgery, 2000. 135(11): p. 1345-52.
100. Hood, R.L., Kosoglu, M.A., Parker, M., Rylander, C.G., *Effects of Microneedle Design Parameters on Hydraulic Resistance.* ASME Journal of Medical Devices: p. In Revision.
101. Kosoglu, M.A., Hood, R.L., Rossmeisl, J.H., Grant, D.C., Robertson, J.L., Rylander, M.N., Rylander, C.G., *Fiberoptic Microneedles: Novel Optical Diffusers for Interstitial Delivery of Therapeutic Light.* Lasers in surgery and medicine: p. In Revision.
102. Kosoglu, M.A., et al., *Fiber Optic Microneedles for Transdermal Light Delivery: Ex Vivo Porcine Skin Penetration Experiments.* Journal of Biomechanical Engineering-Transactions of the Asme, 2010. 132(9): p. -.
103. DeGrandpre, M.D., et al., *Characterization of long pathlength capillary waveguides for evanescent fluorescence sensing applications.* Sensors and Actuators B-Chemical, 2008. 135(1): p. 145-151.
104. Kanner, A.A., *Convection-Enhanced Delivery: High-Grade Gliomas*, G.H. Barnett, Editor. 2007, Humana Press. p. 303-314.
105. Hood, R.L., et al., *Intracranial hyperthermia through local photothermal heating with a fiberoptic microneedle device.* Lasers Surg Med, 2013.
106. Kosoglu, M., R. Hood, and C. Rylander, *Fiberoptic Microneedles for Microscale Interstitial Delivery of Therapeutic Light.* Lasers in surgery and medicine, 2011. 43: p. 920-920.
107. Hood, R.L., et al., *Effects of Microneedle Design Parameters on Hydraulic Resistance.* Journal of Medical Devices-Transactions of the Asme, 2011. 5(3): p. 31012-31016.
108. Casanova, F., P.R. Carney, and M. Sarntinoranont, *Influence of needle insertion speed on backflow for convection-enhanced delivery.* J Biomech Eng, 2012. 134(4): p. 041006.

109. **Morrison, P.F., et al., *Focal delivery during direct infusion to brain: role of flow rate, catheter diameter, and tissue mechanics.* Am J Physiol, 1999. 277(4 Pt 2): p. R1218-29.**
110. **Kanner, A.A., *Convection-Enhanced Delivery High-Grade Gliomas*, G.H. Barnett, Editor. 2007, Humana Press. p. 303-314.**
111. **Hood, R.L., et al., *Effects of Microneedle Design Parameters on Hydraulic Resistance.* Journal of Medical Devices-Transactions of the Asme, 2011. 5(3).**
112. **Yaroslavsky, A.N., et al., *Optical properties of selected native and coagulated human brain tissues in vitro in the visible and near infrared spectral range.* Phys Med Biol, 2002. 47(12): p. 2059-73.**
113. **Keller, B.K., *Characterization of long pathlength capillary waveguides for evanescent chemical sensing applications.* 2004. 5585: p. 143-151.**
114. **Patterson, C.E., R.A. Rhoades, and J.G. Garcia, *Evans blue dye as a marker of albumin clearance in cultured endothelial monolayer and isolated lung.* J Appl Physiol, 1992. 72(3): p. 865-73.**
115. **Chen, M.Y., et al., *Variables affecting convection-enhanced delivery to the striatum: a systematic examination of rate of infusion, cannula size, infusate concentration, and tissue-cannula sealing time.* J Neurosurg, 1999. 90(2): p. 315-20.**
116. **Garcia, P.A., et al., *Intracranial nonthermal irreversible electroporation: in vivo analysis.* J Membr Biol, 2010. 236(1): p. 127-36.**
117. **Sapareto, S.A. and W.C. Dewey, *Thermal dose determination in cancer therapy.* Int J Radiat Oncol Biol Phys, 1984. 10(6): p. 787-800.**
118. **Roti Roti, J.L., *Cellular responses to hyperthermia (40-46 degrees C): cell killing and molecular events.* Int J Hyperthermia, 2008. 24(1): p. 3-15.**
119. **Wilmink, G. and J. Grundt, *Invited Review Article: Current State of Research on Biological Effects of Terahertz Radiation.* Journal of Infrared, Millimeter, and Terahertz Waves, 2011. 32(10): p. 1074-1122.**
120. **O'Connell-Rodwell, C.E., et al., *In vivo analysis of heat-shock-protein-70 induction following pulsed laser irradiation in a transgenic reporter mouse.* J Biomed Opt, 2008. 13(3): p. 030501.**
121. **Salcman, M. and G.M. Samaras, *Hyperthermia for Brain-Tumors - Biophysical Rationale.* Neurosurgery, 1981. 9(3): p. 327-335.**
122. **Tanaka, R., et al., *Radiofrequency hyperthermia for malignant brain tumors: preliminary results of clinical trials.* Neurosurgery, 1987. 21(4): p. 478-83.**
123. **Guthkelch, A.N., et al., *Treatment of malignant brain tumors with focused ultrasound hyperthermia and radiation: results of a phase I trial.* J Neurooncol, 1991. 10(3): p. 271-84.**
124. **Welch, A.J. and M.J.C.v. Gemert, *Optical-thermal response of laser-irradiated tissue*. Lasers, photonics, and electro-optics. 1995, New York: Plenum Press. xxvi, 925 p.**
125. **Cohen, J.D., H.I. Robins, and M.J. Javid, *Sensitization of C6 Glioma to Carboplatin Cytotoxicity by Hyperthermia and Thymidine.* Journal of Neuro-Oncology, 1990. 9(1): p. 1-8.**
126. **Raaphorst, G.P., et al., *A comparison of hyperthermia cisplatin sensitization in human ovarian carcinoma and glioma cell lines sensitive and resistant to cisplatin treatment.* Cancer Chemotherapy and Pharmacology, 1996. 37(6): p. 574-580.**

127. Ko, S.H., et al., *Optimizing a novel regional chemotherapeutic agent against melanoma: Hyperthermia-induced enhancement of temozolomide cytotoxicity.* Clinical Cancer Research, 2006. 12(1): p. 289-297.
128. Begley, D.J., M.W.B. Bradbury, and J. Kreuter, *The blood-brain barrier and drug delivery to the CNS*. 2000, New York: Dekker. 248-249.
129. Chien, Y.W. and S.F. Chang, *Intranasal drug delivery for systemic medications.* Crit Rev Ther Drug Carrier Syst, 1987. 4(2): p. 67-194.
130. Greig, N.H., *Optimizing drug delivery to brain tumors.* Cancer Treat Rev, 1987. 14(1): p. 1-28.
131. Zlokovic, B.V., *The blood-brain barrier in health and chronic neurodegenerative disorders.* Neuron, 2008. 57(2): p. 178-201.
132. Laske, D.W., et al., *Chronic interstitial infusion of protein to primate brain: determination of drug distribution and clearance with single-photon emission computerized tomography imaging.* J Neurosurg, 1997. 87(4): p. 586-94.
133. Fu, Q.G., et al., *Efficacy of intraperitoneal thermochemotherapy and immunotherapy in intraperitoneal recurrence after gastrointestinal cancer resection.* World J Gastroenterol, 2002. 8(6): p. 1019-22.
134. Munson, B.R., D.F. Young, and T.H. Okiishi, *Fundamentals of fluid mechanics*. 5th ed. 2006, Hoboken, NJ: J. Wiley & Sons.
135. Ogura, K., M. Takayasu, and R.G. Dacey, Jr., *Effects of hypothermia and hyperthermia on the reactivity of rat intracerebral arterioles in vitro.* J Neurosurg, 1991. 75(3): p. 433-9.
136. Hood, R.L., et al., *Spatially controlled photothermal heating of bladder tissue through single-walled carbon nanohorns delivered with a fiberoptic microneedle device.* Lasers Med Sci, 2012 Epub ahead of Print.
137. Schatz, S.W., et al., *Low-Power Interstitial Nd-Yag Laser Photocoagulation in Normal Rabbit Brain.* Lasers Med Sci, 1992. 7(4): p. 433-439.
138. Burgery, F.J. and F.A. Fuhrman, *Evidence of Injury to Tissues after Hyperthermia.* Am J Physiol, 1964. 206: p. 1062-4.
139. Frankel, H.M. and S.M. Cain, *Arterial and cerebral venous blood substrate concentrations during hyperthermia.* Am J Physiol, 1966. 210(6): p. 1265-8.
140. Hood, R.L., et al., *Intracranial hyperthermia through local photothermal heating with a fiberoptic microneedle device.* Lasers Surg Med, 2013. 45(3): p. 167-74.
141. Zhang, X.Y., et al., *Interstitial hydraulic conductivity in a fibrosarcoma.* Am J Physiol Heart Circ Physiol, 2000. 279(6): p. H2726-34.
142. Ponce, A.M., et al., *Hyperthermia mediated liposomal drug delivery.* Int J Hyperthermia, 2006. 22(3): p. 205-13.
143. Kong, G., R.D. Braun, and M.W. Dewhirst, *Hyperthermia enables tumor-specific nanoparticle delivery: effect of particle size.* Cancer Res, 2000. 60(16): p. 4440-5.
144. Los, G., M.J. van Vugt, and H.M. Pinedo, *Response of peritoneal solid tumours after intraperitoneal chemohyperthermia treatment with cisplatin or carboplatin.* Br J Cancer, 1994. 69(2): p. 235-41.
145. Bischof, J.C., et al., *Dynamics of cell membrane permeability changes at supraphysiological temperatures.* Biophys J, 1995. 68(6): p. 2608-14.

146. **Perlstein, B., et al.,** ***Convection-enhanced delivery of maghemite nanoparticles: Increased efficacy and MRI monitoring.*** **Neuro Oncol, 2008. 10(2): p. 153-61.**
147. **Voges, J., et al.,** ***Imaging-guided convection-enhanced delivery and gene therapy of glioblastoma.*** **Ann Neurol, 2003. 54(4): p. 479-87.**
148. **Raghavan, R., et al.,** ***Convection-enhanced delivery of therapeutics for brain disease, and its optimization.*** **Neurosurg Focus, 2006. 20(4): p. E12.**